DISTRIBUTED AMPLIFIER CIRCUIT DESIGN

USING

A COMMERCIAL CMOS PROCESS TECHNOLOGY

by

Kyle Gene Ross

A thesis submitted in partial fulfillment
of the requirements of the degree

of

Master in Science

in

Electrical Engineering

MONTANA STATE UNIVERSITY
Bozeman, Montana

July 2006

© COPYRIGHT

by

Kyle Gene Ross

2006

All Rights Reserved

APPROVAL

of a thesis submitted by

Kyle Gene Ross

This thesis has been read by each member of the thesis committee and has been found to be satisfactory regarding content, English usage, format, citations, bibliographic style, and consistency, and is ready for submission to the Division of Graduate Education.

James P. Becker

Approved for the Department of Electrical and Computer Engineering

James N. Peterson

Approved for the Division of Graduate Education

Joseph J. Fedock

STATEMENT OF PERMISSION OF USE

In presenting this thesis in partial fulfillment of the requirements for a master's degree at Montana State University, I agree that the Library shall make it available to borrowers under rules of the Library.

If I have indicated my intention to copyright this thesis by including a copyright notice page, copying is allowable in so far as the copyright license grants without express permission from the copyright holder. Any of these conditions may be waived with permission from the copyright holder.

Kyle Gene Ross

July 2006

ACKNOWLEDGEMENTS

I would like to express my gratitude to those who without their help and encouragement this project would not have been a success. First, I would like to thank my advisor Dr. James Becker for his support and guidance throughout my undergraduate and graduate career. His enthusiasm for research and teaching has inspired me to strive for the same. Secondly, I would like to thank committee members Dr. Donald Thelen and Andy Olson for their indispensable advice and patience. Also, this work would not have been nearly as great without the relief provided by fellow lab-mates Edward Dickman and Kyle Lyson. Lastly, I would like to acknowledge the support provided for this work by both the National Science Foundation (NSF) under grant #347469 and the MOSIS Service through the MOSIS Educational Program (MEP).

TABLE OF CONTENTS

1. INTRODUCTION 1
Introduction 1
Thesis Overview..2

2. DISTRIBUTED AMPLIFIERS..4
Background 4
Theory of Operation 5
MOSFET Realization of the DA 8
Design Procedures..18
CMOS Figures of Merit..18
Device Sizing Procedures 20

3. CMOS TRANSMISSION LINE REALIZATION..29
Transmission Line Parameters 29
Coplanar Strip-line (CPS) Selection and Design 30
Optimal Device Quantity Deduction..41

4. BIASING AND PLANAR INDUCTOR DESIGN 42
Distributed Amplifier Biasing..42
Planar Spiral Inductor Design 45
Inductor Figures of Merit..47
Planar Spiral Inductor Implementation..51

5. CALIBRATION AND CHARACTERIZATION 53
Introduction 53
Calibration..54
Short-Open-Load-Thru (SOLT)..56
Thru-Reflect-Line (TRL) 58
Measurements..63
Delay Line Validation..63
Square Planar Spiral Inductors..66
Isolated Transistors 69
Distributed Amplifier..76

6. CONCLUSIONS AND RECOMMENDATIONS FOR FURTHER WORK...............81
Summary 81
Recommendations for Further Research 82
Planar Spiral Inductors..82
Planar Microwave Circuit Design Course 83

REFERENCES CITED..84

TABLE OF CONTENTS - CONTINUED

APPENDICES 88

APPENDIX A: Non-Quasistatic Effects 89
APPENDIX B: AMIS C5 BSIM3v3 SPICE Model Parameters 92
APPENDIX C: MOSIS T5AR Run Wafer Electrical Test Data and SPICE
Model Parameters 93
APPENDIX D: IE3D Extracted RLGC Parameters for 500mm, 50Ω CPS 98
APPENDIX E: Analytical Planar Spiral Inductor Design...................................100

LIST OF TABLES

Table Page

3.1 DC parasitic parameter values of a 200μm x 0.6μm (WxL) NMOS transistor....30

3.2 AMIS C5 process specifications for metal layer 3 35

3.3 IE3D extracted RLGC parameters for a 500μm, 50Ω CPS 36

3.4 Parasitic parameter values of a 200μm x 0.6μm (WxL) NMOS transistor at 1GHz 37

3.5 IE3D extracted RLGC parameters for 500μm gate and drain CPS 38

4.1 Coefficients for modified Wheeler expression 49

4.2 Coefficients for current sheet expression....49

LIST OF FIGURES

Figure Page

2.1 TWA illustration of the DA 6

2.2 Schematic representation of a N-stage MOSFET TWA....8

2.3 Lumped-element equivalent circuit for an incremental length of transmission line 10

2.4 Small-signal model of the MOSFET when the source is connected to the substrate (body)....10

2.5 Small-signal model of the MOSFET after applying Miller's Theorem 11

2.6 Distributed amplifier transmission line circuits for the (a) gate line and (b) the drain line....11

2.7 Equivalent circuit for single unit cell of (a) gate and (b) drain line circuits....12

2.8 ADS simulation schematic used in determining maximum unit cell electrical lengths 13

2.9 CMOS performance envelope as a function of transistor speeds 21

2.10 Plot illustrating the relationship between a normal, or Gaussian, process distribution and the standard deviation (sigma) limits....22

2.11 Unity-gain frequency of 200x0.6 µm (WxL) NMOS transistor (I_D = 31.1mA) 23

2.12 ADS simulation setup used to determine unity-gain frequency of NMOS....24

2.13 Source and load stability contours of a single 200µm by 0.6µm (WxL) MOSFET....27

2.14 Source and load stability contours of a single 200µm by 0.6µm (WxL) MOSFET loaded at the gate with a series resistance of 1Ω....27

3.1 Microstrip transmission line realized in CMOS substrate using the highest (yellow) and lowest (red) metal interconnect layers 31

LIST OF FIGURES – CONTINUED

Figure Page

3.2 AMIS C5 process family substrate diagram 32

3.3 Coplanar waveguide cross-sectional illustration 33

3.4 Coplanar stripline cross-sectional illustration....................................34

3.5 Micrograph of the fabricated gate and drain CPS....................................40

4.1 DA circuit with DC bias network realized with square-spiral inductors...43

4.2 ADS schematic of DA circuit with an optimal DC bias network realized with ideal RF-chokes....................................44

4.3 Planar spiral inductor geometries for (a) square, (b) hexagonal, (c) octagonal, and (d) circular realizations....................................47

5.1 GGB model 40A CPS RF probe tip diagram....................................54

5.2 Measured 2-port S-parameters of a CS-8 thru line after SOLT calibration 57

5.3 Measured reflection from a CS-8 short circuit after SOLT calibration.....58

5.4 Micrograph of the fabricated CPS TRL calibration standards; TOP-open reflects, MIDDLE-short reflects, BOTTOM-thru line.............60

5.5 Two-port S-parameters of an on-chip thru line after TRL calibration.......62

5.6 Input impedances of on-chip short and open reflects after TRL calibration 63

5.7 Micrograph of an isolated drain delay line being probed after SOLT calibration 64

5.8 ADS delay line phase difference simulation schematic....................................64

5.9 Delay line phase difference, ADS simulation (Si_3N_4 passivation layer.....65

LIST OF FIGURES – CONTINUED

Figure Page

5.10 Delay line phase difference, measured data, SOLT calibration 04.21.2006 66

5.11 Micrograph of a 4.25 turn spiral inductor undergoing a DC connectivity test 67

5.12 Comparing the simulated S-parameters of the 4.25 turn spiral inductor to those of the measured on-chip inductor 67

5.13 Comparing effects of including Si_3N_4 passivation layer on the simulated S-parameters of the 4.25 turn spiral inductor using Momentum 68

5.14 Micrograph of a 200μm by 0.6μm (WxL) transistor within a 500μm CPS structure 69

5.15 Measured and simulated I_D versus V_{DS} curves for a single 200μm by 0.6μm (WxL) transistor 70

5.16 Simulated I_D versus V_{DS} curves for a single 200μm by 0.6μm (WxL) transistor using BSIM3v3 model parameters provided by AMIS and MOSIS 71

5.17 Measured and simulated gain and input matching of a 200μm by 0.6μm (WxL) transistor 72

5.18 Measured and simulated reverse isolation and output matching of a 200μm by 0.6μm (WxL) transistor 72

5.19 Layout representation of multi-fingered transistor of size 200/0.6μm (W/L) 74

5.20 Measured and simulated gain and input matching of a 200μm by 0.6μm (WxL) transistor including an effective gate resistance in simulation 75

5.21 Measured and simulated reverse isolation and output matching of a 200μm by 0.6μm (WxL) transistor including an effective gate resistance in simulation 76

LIST OF FIGURES – CONTINUED

Figure Page

5.22 Micrograph of the fabricated distributed amplifier....................................77

5.23 Measured 2-port S-parameters of the distributed amplifier after SOLT calibration 78

5.24 Measured gain (S_{21}) of DA with bias levels V_{DS} = 3.5V and V_{GS} = 1.9V 78

5.25 Simulated gain (S_{21}) of DA with bias levels V_{DS} = 3.5V and V_{GS} = 1.9V 79

5.26 Measured and simulated gain (S_{21}) and input matching (S_{11}) of the DA...80

ABSTRACT

The demand for ever increasing amounts and rates of data transmission is one of the most significant driving forces in the design of modern telecommunications systems. In response, integrated circuit (IC) designers are forced to achieve higher and higher bit rates. Increased bit rates in turn impel the IC communication systems to achieve ever larger bandwidths while maintaining stringent requirements on other design specifications such as cost, die-size and power consumption. One alternative approach to high-bandwidth design showing promise is the design of distributed integrated circuits. Distributed integrated circuit creation applies design methods that have been investigated for nearly seventy years to the rapidly evolving semiconductor process technologies of the modern IC landscape. Simply stated, it is an approach whereby the combination of multiple parallel signals results in increased bandwidths, enhanced power combining faculties, and often novel design capabilities for a given IC process. Consequently, the focus of this thesis is upon the application of distributed integrated circuit methodologies towards the realization of a distributed broadband amplifier in a commercial CMOS process technology. On-chip spiral inductors were utilized in on-chip bias circuitry. The measured performance of the DA was found to be significantly degraded from that of initial simulation by the poor performance of the fabricated inductors. In addition to serving as a portion of the author's thesis requirements, the fabricated chips are to be incorporated into a university laboratory session in subsequent semesters.

CHAPTER ONE
INTRODUCTION

Motivation

The demand for ever increasing amounts and rates of data transmission is one of the most significant driving forces in the design of modern telecommunications systems. In response, integrated circuit (IC) designers are forced to achieve higher and higher bit rates. Increased bit rates in turn impel the IC communication systems to achieve ever larger bandwidths while maintaining stringent requirements on other design specifications such as cost, die-size and power consumption. Increasing the frequency of operation of these ICs into microwave and millimeter-wave frequencies is an obvious means of achieving larger bandwidth.

In order to discuss the requirements for such a transition there are several IC design characteristics that need to be discussed. First, the frequency at which the transistors in a given IC semiconductor technology exhibit unity short-circuit current gain is an important quantifier and is denoted by f_T. Unity-gain frequencies in mainstream technologies regularly approach 50 GHz [1] and have even been reported at a maximum of 604 GHz for exotic technologies [2]. However, even while the individual transistors in a given process may have a sufficiently high cutoff frequency, the circuits employing the particular process will undoubtedly be restricted to operating at frequencies much below f_T. This unavoidable condition arises from two primary wherefores. The first is due to the importance of employing degenerative, or negative, feedback in many analog circuit designs. Negative feedback provides design benefits such as reduced distortion, increased bandwidth, and system stability at the cost of a reduction in the gain of the

system. Subsequently, in order to achieve the desired gains, systems must be designed with open-loop gains considerably larger than requisite in closed loop. This is to say that the systems are forced to operate at frequencies for which the active devices are able to provide gain much above unity and thus must operate well below f_T. Secondly, the passive devices within the circuit have their own associated resonant frequencies that are ofttimes much below that of the active devices. Thus, simply increasing the frequency of operation is often an impractical or simply unattainable solution to the problem of increasing bandwidth. This realization leads to the conclusion that alternative design methodologies are required for the construction of future high-speed communication systems.

One alternative approach to high-frequency design showing promise is the design of distributed integrated circuits. Distributed integrated circuit creation employs design methods that have been investigated for nearly seventy years to the rapidly evolving semiconductor process technologies of the modern IC landscape. Simply stated, it is an approach whereby the combination of multiple parallel signals results in increased bandwidths, enhanced power combining faculties, and often novel design capabilities for a given IC process. Consequently, the focus of this thesis will be the application of distributed integrated circuit methodologies towards the realization of a distributed broadband amplifier in a commercial IC technology.

Thesis Overview

This thesis is comprised of six main sections and is organized in the following manner. Chapter 2 introduces the operational principles of distributed amplifiers and

examines the implementation of such a device in commercial complementary metal-oxide semiconductor (CMOS) fabrication processes. Chapter 3 discusses the realization of suitable transmission line structures via the photolithographic fabrication methods present in the selected IC process. The design procedures and theoretical underpinnings of planar spiral inductors for use within a DC biasing scheme are then visited in Chapter 4. Measurement techniques, including the necessary calibration approaches, suitable for microwave and mm-wave device characterization are reviewed in Chapter 5. Chapter 6 completes the thesis with an examination of the measured results for the fabricated distributed amplifier and concludes with recommendations for further work.

CHAPTER TWO
DISTRIBUTED AMPLIFIERS

Background

Certainly one of the most resourceful examples of distributed circuit design conceived is the distributed amplifier (DA) formulated by William S. Percival in 1936 [3]. In that year Percival proposed a design by which the transconductances of individual vacuum tubes could be added linearly, thus arriving at a circuit that achieved a gain-bandwidth product greater than that of an individual tube. Percival's design did not gain widespread awareness however, until a publication on the subject was authored by Ginzton, Hewlett, Jasberg, and Noe in 1948 [4]. It is to this later paper that the term *distributed amplifier* can actually be traced.

Traditionally, DA design architectures have been realized using III-V semiconductor technologies, such as GaAs [5]-[7] and InP [8],[9], due the superior performance of these technologies resulting from these technologies' higher bandgaps (higher electron mobility), higher saturated electron velocity, higher breakdown voltages and higher-resistivity substrates. The latter contributes much to the availability of higher quality-factor (*Q*-factor or simply *Q*) integrated passive devices in the III-V semiconductor technologies. Even so, in order to meet the marketplace demands on cost, size, and power consumption of monolithic microwave integrated circuits (MMICs), on-going research continues in the development of mainstream digital bulk-CMOS processes for such purposes. The continuous scaling of feature sizes in current IC technologies has enabled microwave and mm-wave CMOS circuits to directly benefit from the resulting increased unity-gain frequencies of the scaled technology. This device scaling, along

with the advanced process control available in today's technologies, has recently made it possible to reach an f_T of 170 GHz and a maximum oscillation frequency (f_{max}) of 240 GHz in a 90nm CMOS process [10].

Theory of Operation

The operation of the DA can perhaps be most easily understood when explained in terms of the *traveling wave amplifier* (TWA) illustrated in Figure 2.1. As seen in the figure, the DA consists of a pair of transmission lines with characteristic impedances of Z_0 independently connecting the inputs and outputs of several active devices. An RF signal is thus supplied to the section of transmission line connected to the input of the first device. As the input signal propagates down the input line, the individual devices respond to the forward traveling input step by inducing an amplified complementary forward traveling wave on the output line. This assumes the delays of the input and output lines are made equal through intelligent selection of propagation constants and lengths of the two lines and as such the output signals from each individual device sum in phase. Terminating resistors Z_g and Z_d are placed to minimize destructive reflections.

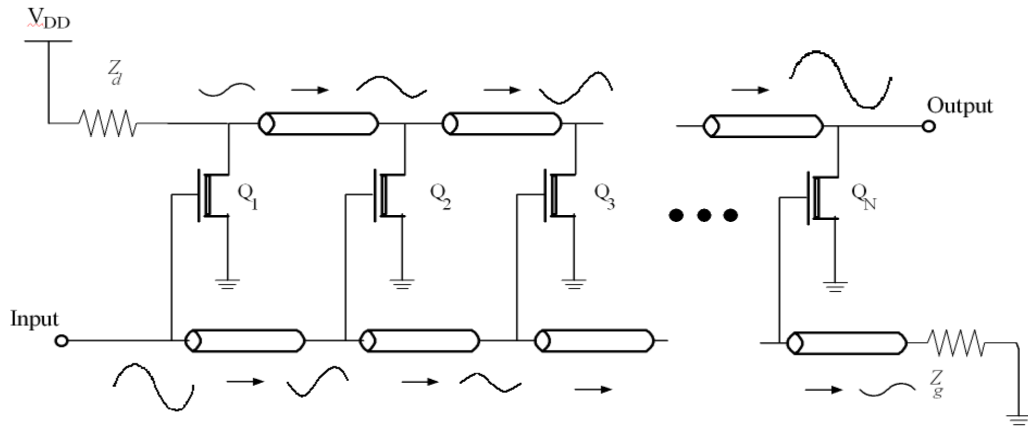

Figure 2.1 TWA illustration of the DA.

Denoting the transconductive gain of each device as g_m and recognizing that the output impedance seen by each transistor is half the characteristic impedance of the transmission line one arrives at the overall voltage gain of the DA being [11]

$$A_V = n g_m \frac{Z_o}{2}. \tag{2.1}$$

Neglecting losses the gain demonstrates a linear dependence on the number of devices (stages). Unlike the multiplicative nature of a cascade of conventional amplifiers, the DA demonstrates an additive quality. It is this synergistic property of the DA architecture that makes it possible for it to provide gain at frequencies beyond that of the unity-gain frequency of the individual stages in a matched system. In practice the number of stages is limited by the diminishing input signal resulting from attenuation on the input line. Means of determining the optimal number of stages are discussed in the subsequent section. Bandwidth is typically limited by impedance mismatches brought

about by frequency dependent device parasitics.

Another way of understanding the advantages of the DA topology is recognize that the architecture realizes a distributed broadband matching network through absorption of the device parasitics into the matching network itself. In order to achieve greater gain from a conventional single device amplifier one would simply increase the size (width) of the device as desired. However in order to provide adequate matching the matching networks (input and output transmission lines) must then be implemented with progressively higher characteristic impedances in order to compensate for the larger input and output parasitic device capacitances. Subsequently, the design of the input and output matching networks becomes increasingly difficult as design tolerances makes the physical realization of these high impedance values impractical. In an IC implementation of the DA the tolerances of high characteristic impedance distributed matching networks are made difficult to maintain through virtue of the unavoidable process variations present within any given fabrication technology. The impact of these variations is further explored in the section titled “Device Sizing Procedures”. Another limiting feature of large-sized devices within the context of the distributed amplification is revealed when considering the Bragg cutoff frequency of the parasitically loaded transmission lines. The Bragg cutoff frequency of the transmission lines within a distributed matching network can be roughly computed by

$$\omega_c \approx \frac{2}{\sqrt{L_{TL}(C_{TL} + C_{device})}},$$

where L is the total inductance of the line segment and C is the sum of the line segment capacitance and the parasitic loading capacitance upon the line segment [11]. Hence, it can be readily seen that increasing the device size in order to realize larger gains simultaneously lowers the cutoff frequency of the distributed matching network. Thus, by providing a means of achieving increased gain without substantially increasing device size the DA achieves a physically realizable broadband amplifier with performance greater than that possible through traditional amplifier designs.

Lastly, its important to note that the DA architecture incurs delay in order to achieve its broadband gain characteristics. With a bit of insight, one realizes that this delay can actually be a desired feature in the design of another distributive system, the distributed oscillator. As is detailed later in this thesis, the simplicity of the above discussion belies the rather intricate design process of a distributed amplifier.

MOSFET Realization of the DA

As previously discussed, the goal of DA design is to couple two transmission lines by the transconductances of active devices. Detailed analysis of the operation of the DA is presented in [12] and [13] in terms of the loaded gate and drains transmission lines and will be used to derive the gain equations for a CMOS DA. Figure 2.2 shows the basic schematic representation of a N-stage MOSFET traveling wave amplifier. The input transmission line having a characteristic impedance of Z_g connects the gates of the devices with a spacing of ℓ_g. Similarly the drains are connected via a transmission line with a characteristic impedance of Z_d and a spacing of ℓ_d.

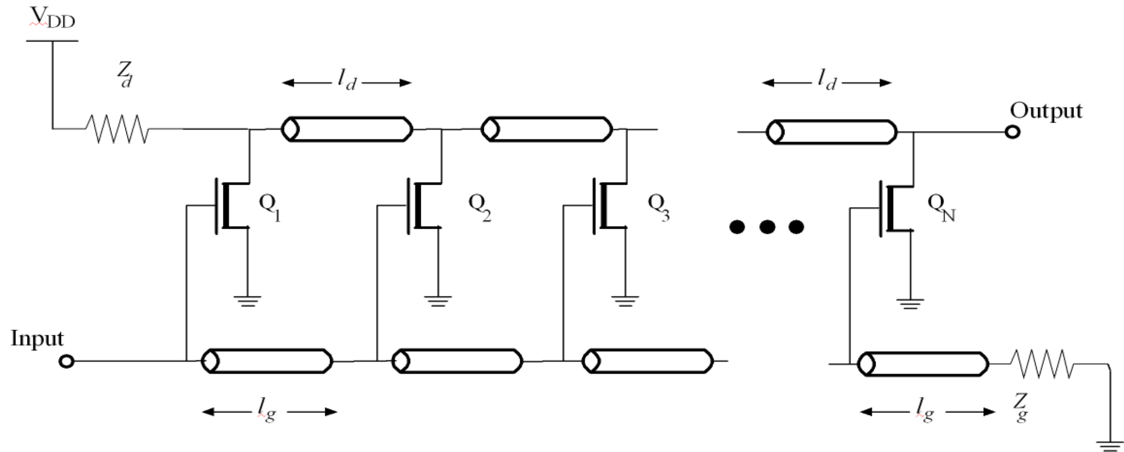

Figure 2.2 Schematic representation of a N-stage MOSFET TWA.

Implementing the DA architecture in CMOS dictates the active devices are MOSFETS. Also, the choice of transmission line structure is governed by the requirement that the line be realizable by photolithographic processes thereby limiting one to two-conductor choices such as microstrip and coplanar waveguide (CPW) geometries. Recognizing that the lumped-element equivalent of a short piece of line of length Δz can be modeled as a lumped-element circuit as shown in Figure 2.3, the employment of the small-signal model of the MOSFET shown in Figure 2.4 can subsequently be used to decompose the circuit of Figure 2.2 into the separate loaded transmission lines for the gate and drain terminals shown in Figure 2.6. Note that in this decomposition the bridging gate to drain capacitance of the MOSFET's small signal model was replaced with a shunt capacitor using Miller's theorem [14],

$$C_M = C_{gd} \cdot \left[1 + g_m \left(r_o // \frac{Z_d}{2} \right) \right] \tag{2.2}$$

and

$$C_M' = C_{gd} \cdot \left[1 + \frac{1}{g_m \left(r_o // \frac{Z_d}{2} \right)} \right]. \tag{2.3}$$

This Miller replacement is shown in Figure 2.5.

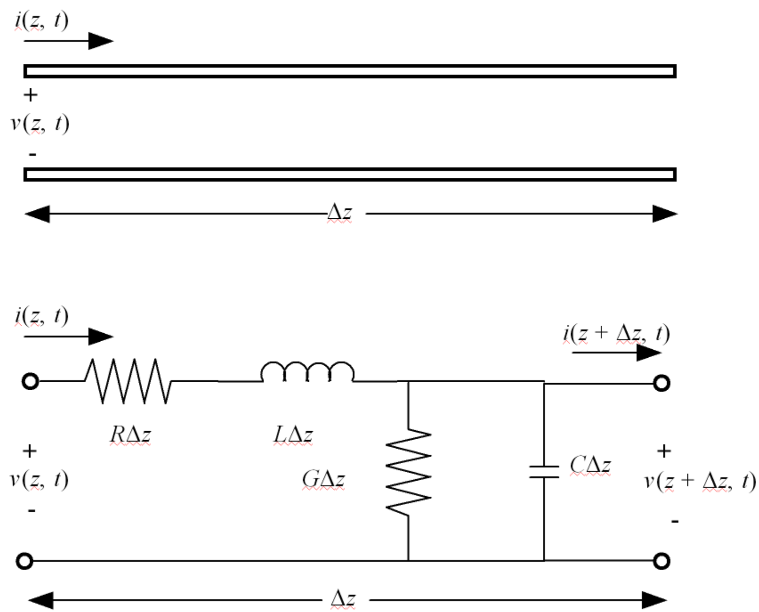

Figure 2.3 Lumped-element equivalent circuit for an incremental length of transmission line.

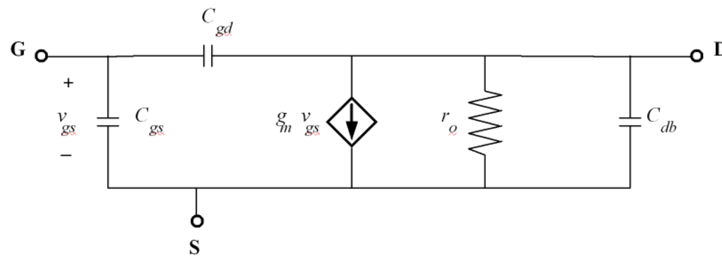

Figure 2.4 Small-signal model of the MOSFET when the source is connected to the substrate (body).

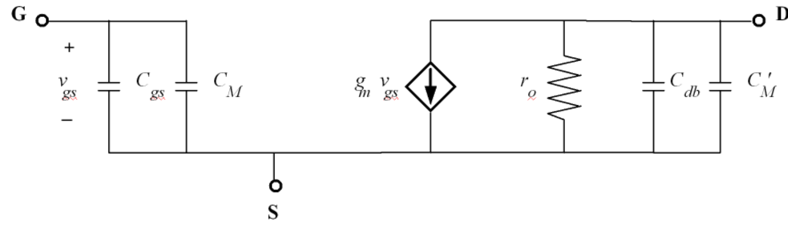

Figure 2.5 Small-signal model of the MOSFET after applying Miller's Theorem.

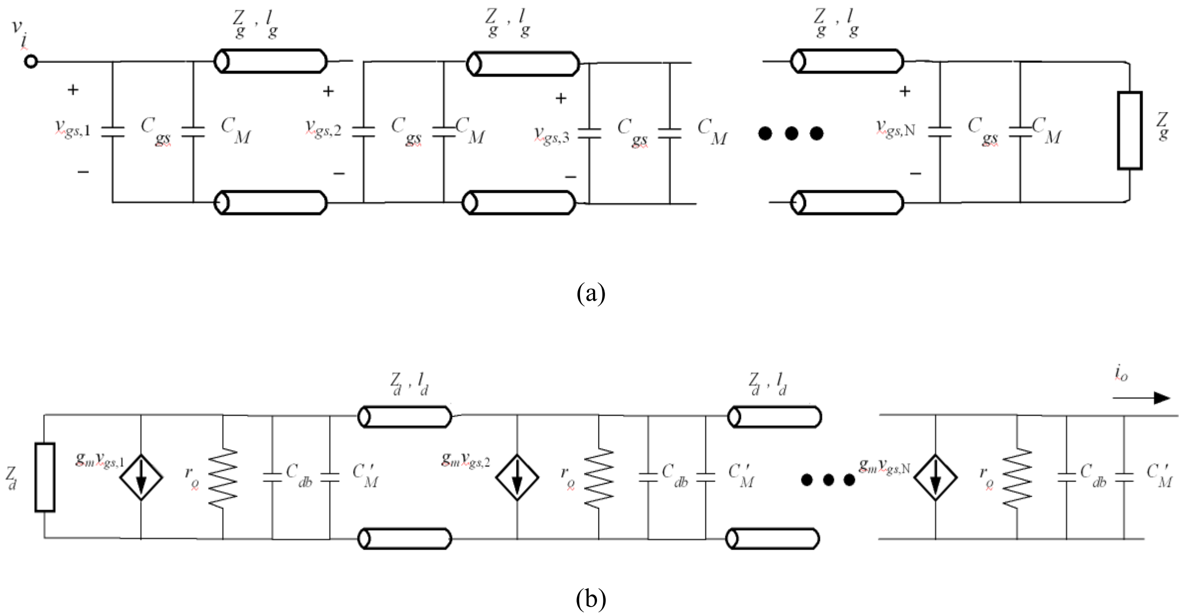

Figure 2.6 Distributed amplifier transmission line circuits for the (a) gate line and (b) the drain line.

Notice that while ground conductors are not shown in Figure 2.2, they are in Figure 2.6. This is due to the aforementioned restriction to process realizable two-conductor transmission lines. Matching impedances terminate each transmission line circuit and the dependent current sources provide coupling between the two circuits in the form $i_d = g_m v_{gs}$. Figures 2.7a and 2.7b thus show the equivalent circuits for a single unit cell for the gate and drain line circuits, respectively.

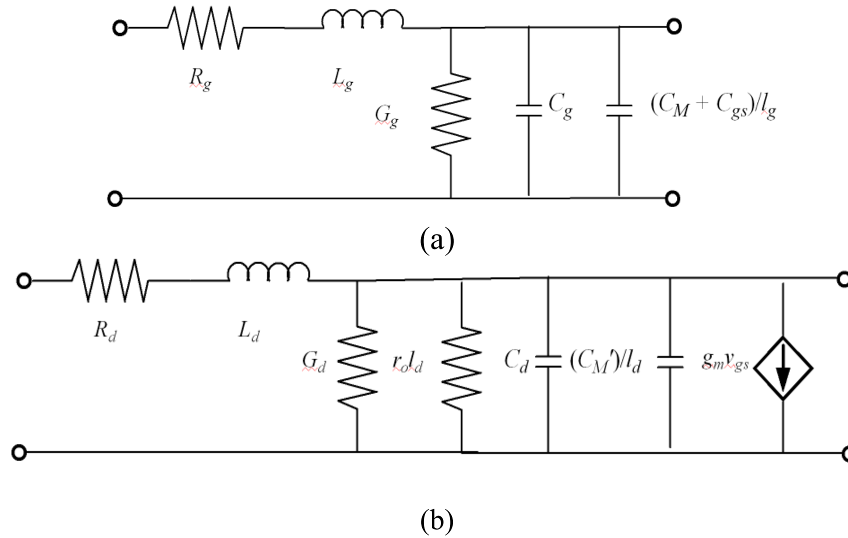

Figure 2.7 Equivalent circuit for single unit cell of (a) gate and (b) drain line circuits.

Recall from the lumped-element equivalent model of Figure 2.3 that the R_x, L_x, G_x, and C_x terms denote the series resistance per unit length for both conductors, series inductance per unit length for both conductors, shunt conductance per unit length, and the shunt capacitance per unit length, respectively, for each transmission line. $(C_M + C_{gs})/l_g$ represents the equivalent per unit length loading due to the input capacitance of the MOSFET, while $(C_M')/l_d$ and $r_o l_d$ represent the equivalent per unit length loading due to the output capacitance and resistance, respectively. These loading effects can be approximated as such provided the electrical lengths of the unit cells are kept small (<5º). The preceding restriction on the electrical length was determined via a straightforward simulation using Agilent Technologies's electronic design automation software system, Agilent Advanced Design System (ADS) [15]. This simulation, the schematic of which is given in Figure 2.8, involved the examination of the effects of varying the electrical length of a section of transmission line with a characteristic impedance of an unloaded

gate TL (the determination of this value is explained in Chapter 3) in-line with 50Ω sections.

The gate TL was chosen because, as is shown in Chapter 3, its characteristic impedance is necessarily designed to be greater than that of the drain TL. Thus, the simulation modeled the effects of varying the connecting lengths of TL between the loading active devices. Through this simulation it was found that beyond an electrical length of 5° significant reflections resulted from the resulting impedance mismatches.

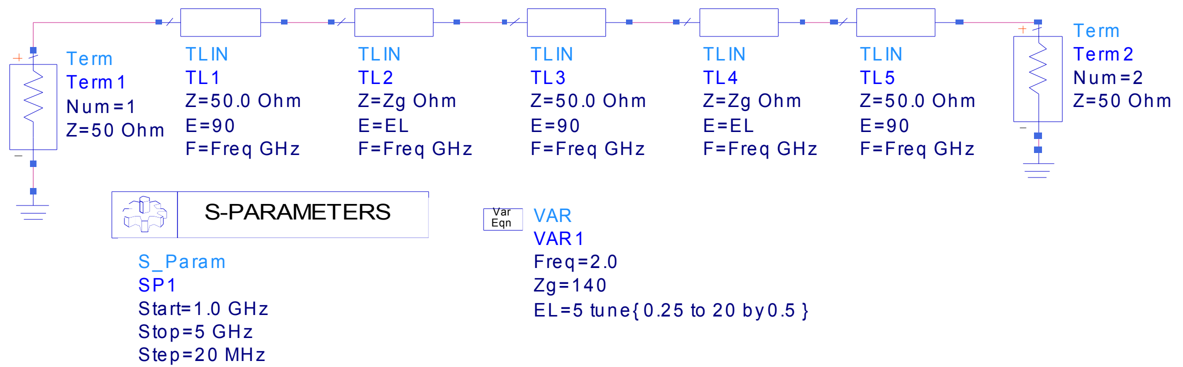

Figure 2.8 ADS simulation schematic used in determining maximum unit cell electrical lengths.

Basic transmission line theory can now be utilized to determine the effective transmission parameters, characteristic impedance and propagation constant, of each line. Hence, the series impedance and shunt admittance per unit length, including losses, of the equivalent gate line are written

$$Z = R_g + j\omega L_g, \tag{2.4}$$

$$Y = G_g + j\omega (C_g + C_{gs}'/l_g), \tag{2.5}$$

where $C_{gs}{}' = C_{gs} + C_M$. The complex characteristic impedance of the gate line is thus given as

$$Z_g = \sqrt{\frac{Z}{Y}} = \sqrt{\frac{R_g + j\omega L_g}{G_g + j\omega (C_g + C_{gs}{}'/l_g)}}. \tag{2.6}$$

The expression for the propagation constant of the gate line is as follows,

$$\gamma_g = \alpha_g + j\beta_g = \sqrt{ZY} = \sqrt{G_g R_g + j\omega (C_g + \frac{C_{gs}{}'}{l_g})R_g + j\omega G_g L_g - \omega^2 L_g \left(C_g + \frac{C_{gs}{}'}{l_g} \right)}. \tag{2.7}$$

Similarly, the series impedance and shunt admittance per unit length of the equivalent drain line are

$$Z = R_d + j\omega L_d, \tag{2.8}$$

$$Y = G_d + \frac{1}{r_o l_d} + j\omega (C_d + C_M{}'/l_d), \tag{2.9}$$

and the characteristic impedance of the drain line is written as

$$Z_d = \sqrt{\frac{Z}{Y}} = \sqrt{\frac{R_d + j\omega L_d}{G_d + \frac{1}{r_o l_d} + j\omega (C_d + C_M{}'/l_d)}}. \tag{2.10}$$

For the drain line the propagation constant is given to be

$$\gamma_d = \alpha_d + j\beta_d = \sqrt{ZY} = \sqrt{G_d R_d + \frac{R_d}{r_o l_d} + j\omega (C_d + \frac{C_M{}'}{l_d})R_d + j\omega G_d L_d + j\omega \frac{L_d}{r_o l_d} - L_d \omega^2 (C_d + \frac{C_M{}'}{l_d})}. \tag{2.11}$$

Using the input to the first MOSFET as the reference point for all subsequent phase denotations, the gate-to-source voltage of the *n*th device resulting from an initial input voltage applied to the first device can be denoted as

$$v_{gs}^{\ n} = v_i e^{-(n-1)\gamma_g l_g} \tag{2.12}$$

Notice that this voltage is the product of the incident input voltage and an exponential damping factor dependent upon the length and propagation constant of the loaded gate line. Each device thus excites the drain line in a way that produces waves in both directions of the form

$$-\frac{1}{2} I_d^{\ n} e^{\pm \gamma_d z}. \tag{2.13}$$

Recalling that the coupling relationship between the gate and drain line can be expressed as $I_d^n = g_m v_{gs}^{\ n}$, the total output current at the drain of the *M*th device is given to be

$$I_o = -\frac{1}{2}\sum_{n=1}^{M} I_d^{\ n} e^{-(M-n)\gamma_d l_d} = -\frac{g_m v_i}{2} e^{-(M\gamma_d l_d - \gamma_g l_g)} \sum_{n=1}^{M} e^{-n(\gamma_g l_g - \gamma_d l_d)}. \tag{2.14}$$

When the phase velocities of the forward traveling waves present on gate and drain lines are equal the terms in the summation will add in phase. By inspection, this will only occur when $\beta_g l_g = \beta_d l_d$. The backwards traveling waves indicated by (2.13) subsequently

will not be be in phase and optimally will be wholly terminated in the drain line matching resistor. Using the following summation formula for a geometric series

$$\sum_{k=m}^{n} ar^{k} = \frac{a(r^{m} - r^{n+1})}{1 - r}, \tag{2.15}$$

the expression derived above for the output current can be simplified to

$$I_o = -\frac{g_m v_i}{2} \frac{e^{\gamma_d l_d}\left[e^{-M\gamma_g l_g} - e^{-M\gamma_d l_d}\right]}{e^{-(\gamma_g l_g - \gamma_d l_d)} - 1} = -\frac{g_m v_i}{2} \frac{e^{-M\gamma_g l_g} - e^{-M\gamma_d l_d}}{e^{-\gamma_g l_g} - e^{-\gamma_d l_d}}. \tag{2.16}$$

Assuming matched input and output ports, the amplifier power gain can thus be obtained by relating the incident input voltage to the total output current as follows

$$G = \frac{P_{out}}{P_{in}} = \frac{\frac{1}{2}\left|I_o\right|^2 Z_d}{\frac{1}{2}\left|v_i\right|^2 / Z_g} = \frac{g_m{}^2 Z_g Z_d}{4}\left|\frac{e^{-M\gamma_g l_g} - e^{-M\gamma_d l_d}}{e^{-\gamma_g l_g} - e^{-\gamma_d l_d}}\right|^2. \tag{2.17}$$

This expression can be further reduced when the phase velocity equalization ($\beta_g l_g = \beta_d l_d$) requirement is applied to the expression

$$G = \frac{g_m{}^2 Z_g Z_d}{4}\left|\frac{e^{-M\alpha_g l_g} - e^{-M\alpha_d l_d}}{e^{-\alpha_g l_g} - e^{-\alpha_d l_d}}\right|^2. \tag{2.18}$$

Neglecting losses, this expression reduces to

$$G = \frac{g_m{}^2 Z_g Z_d M^2}{4}, \tag{2.19}$$

indicating the linear dependence of the voltage gain upon the number of stages previously claimed to have been possessed by the distributed amplifier.

Another important property to be observed in the gain expression of (2.18) is the exponential decay of the gain as the number of stages goes to infinity. As previously hinted at, this practical limitation is directly proportional to the attenuation of the transmission lines. For lossy transmission lines the incident input wave will eventually degrade to a point that subsequent devices will observe virtually no input signal, therefore contributing nothing to the traveling wave upon the drain line. Similarly, the initial amplified signals will incur degradation upon the drain line though typically to a lesser extent as will be explained when the actual design of the transmission lines is investigated. Knowing this, the next logical step is to determine the optimal number of stages for which the gain of the distributed amplifier is maximized. By differentiating (2.18) with respect to M and setting the result to zero allows one to the following expression for the optimal number of stages

$$M(G_{MAX}) = \frac{\ln(\alpha_g l_g / \alpha_d l_d)}{\alpha_g l_g - \alpha_d l_d}. \tag{2.20}$$

Design Procedures

Expression (2.18) indicates that the gain of the distributed amplifier is dependent upon the frequency of operation, the active device parameters, and the transmission line circuit characteristics. Thus, the first decision to be made by the designer is the selection of the process technology in which the design is to be realized. AMI Semiconductor's (AMIS) C5 process family was chosen for this project due to a combination of the experience garnered by the author's use of this process in the analog IC courses offered at the university (EE414 and EE415) and its availability through the MOSIS Educational Program (MEP)[1]. The C5 process technology used is one optimized for 5V mixed-signal applications and has a minimum feature size of 0.6µm, thereby providing a fundamental limit on the performance of any fabricated transistors. In order to realize the limitations imposed by a particular process technology following is a discussion of the relationships between relevant figures of merit (FOM) and physical device characteristics as pertaining to CMOS technologies.

CMOS Figures of Merit

Expressions for first-order approximations of the unity-gain frequency f_t, the maximum frequency of oscillation f_{max}, the minimum noise figure, and the third harmonic intercept voltage V_{IP3} for a CMOS process technology are given below [16]

1 "MOSIS is an integrated circuit fabrication service where one can purchase prototype and small-volume production quantities of integrated circuits and related products. MOSIS lowers the cost of fabrication by combining designs from many customers onto multi-project wafers, thereby significantly decreasing the cost of each design." Since 1986 The MOSIS Service has provided support for "unfunded research conducted by graduate students and faculty who needed to develop critical mass in their areas of research in order to attract funding for future research." (http://mosis.org)

$$f_t = \frac{1}{2\pi} \cdot \frac{g_m}{C_g + C_{gb} + C_{gso} + C_{gdo}}, \tag{2.21}$$

$$f_{\max} = \frac{f_t}{2\sqrt{(R_g + R_i)(g_{ds} + 2\pi f_t C_{gdo})}}, \tag{2.22}$$

$$NF_{\min} = 1 + K \cdot \frac{f}{f_t}\sqrt{g_m(R_g + R_i + R_s)}, \tag{2.23}$$

$$V_{IP3} = \sqrt{\frac{24 \cdot g_m}{g_{m3}}}, \tag{2.24}$$

where g_m and g_{m3} are the fundamental and third-order device transconductances; C_g, C_{gb}, C_{gso}, and C_{gdo} are the intrinsic input capacitance, the gate-to-bulk capacitance, the gate-to-source overlap capacitance, and the gate-to-drain overlap capacitances, respectively; R_g, R_i, and R_s, are the gate resistance, real part of the input impedance due to non-quasistatic effects (see Appendix A), and source series resistances, respectively; and g_{ds} is the output conductance.

Examining the preceding FOM expressions allows one to recognize the effects physical device characteristics and subsequently the process technology limitations have on the performance of analog ICs. Recall that the expression for the transconductance of a saturated MOSFET in strong inversion can be given as

$$g_m = \sqrt{2\mu_0 C_{ox} \frac{W}{L} I_D} = \mu_0 C_{ox} \frac{W}{L}(V_{GS} - V_t), \tag{2.25}$$

where μ_0, C_{ox}, W, L, I_D, V_{GS}, and V_t are the electron mobility of the channel, the capacitance per unit area of the parallel-plate capacitor formed between the gate and the channel, the width and length, the DC bias current of the transistor, the gate-to-source

bias voltage, and the threshold voltage of the transistor, respectively.

Combining 2.25 with 2.21 allows one to recognize that device performance is decidedly dependent on device size, in terms of both the channel size and the associated capacitances, and upon the bias conditions. Mark that the MOSFET transconductance is square-root dependent upon the large-signal, or DC, drain current while linearly dependent upon both the gate-to-source and threshold voltages. One may also recognize that process scaling results in both an increased unity-gain frequency and an increased maximum frequency of oscillation through decreased channel lengths and reduced parasitic capacitances. This is an important point to remember when the future applicability of commercial CMOS IC technologies for microwave and mm-wave applications is considered.

Device Sizing Procedures

Appendix B gives the BSIM3v3[2] model for the "typical" process corner as provided by AMIS. *Process corners* represent an important tool for IC designers in the creation of devices that routinely operate within the specifications claimed and are thus explained.

CMOS processes typically suffer from a substantial parameter variability from run to run and even from wafer to wafer. Thus, in order to provide IC designers with a measure of reliability in the design process, process engineers provide a performance envelope for each device. This performance envelope is a compromise between parameter variation and process yield, as those wafers tested outside the envelope are

2 Berkeley Short Channel IGFET SPICE model version 3.3. Note: MOSIS BSIM3 SPICE parameters are not verified for circuit behavior above 500MHz (http://www.mosis.org/support/faqs/faq_spice.html#11.0).

typically discarded. As the chief design focus in CMOS technologies has historically been in the digital domain, this performance envelope is generally described as a function of NMOS and PMOS speeds, as shown in Figure 2.9, bounded by the worst-case acceptable process conditions. These worst-case boundaries are referred to as the "process corners". The most commonly employed process corners thus are obtained through a restriction of the device speed envelope to the following five envelope locations: typical (TYP) PMOS and NMOS speeds and supply voltage; worst-case power (WCP), fast PMOS and NMOS; worst-case speed (WCS), slow PMOS and NMOS ; worst-case one (WC1), slow PMOS and fast NMOS; worst-case zero (WC0), fast PMOS and slow NMOS [17]. Temperature and power supply voltages represent additional degrees of variability to an IC designer, with a typical value of 27ºC representing the nominal operating temperature.

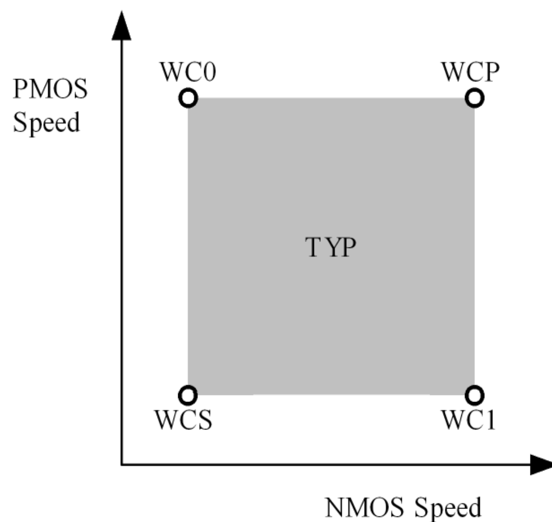

Figure 2.9 CMOS performance envelope as a function of transistor speeds.

It is important to note that these process corners are purely statistical in their definition. A foundry will typically define their process corners to be those process parameters that occur within three to four standard deviations from the process mean (typical) [17]. Looking a Figure 2.10 it becomes clear that a three sigma process corner definition implies that the designer can count on circuit performance within the specified performance envelope approximately 99.73% of the time. Consequently, there always exists a probability that a fabrication will fall outside of this tolerance at some time. It the goal of the process engineers to ensure that this chance is minimized, thus maximizing die yield and subsequently foundry profitability.

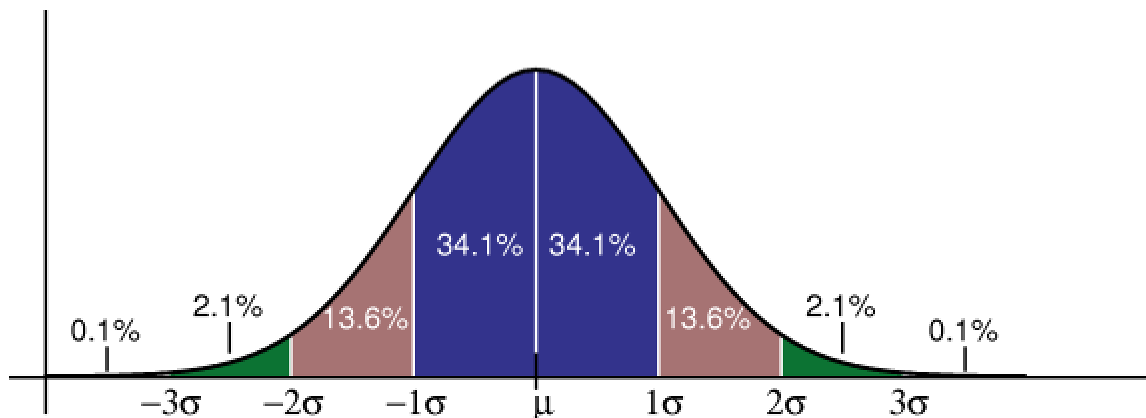

Figure 2.10 Plot illustrating the relationship between a normal, or Gaussian, process distribution and the standard deviation (sigma) limits. (http://en.wikipedia.org/wiki/Image:Standard_deviation_diagram.png)

A standard system impedance of 50Ω was assumed for the design. Therefore the transistors were designed for "optimum performance" with 50Ω loading upon both the input (gate) and output (drain) terminals. As a chief goal of the DA design was broadband performance, an optimally performing transistor was defined to be one with the highest cutoff frequency with 50Ω loading. Thus, using the BSIM3v3 device models

provided by AMIS in conjunction with the *Nominal Optimization* feature present in ADS an "optimally" sized transistor was deduced using the design criteria that the transistor gain be maximized over a frequency range of 0-30GHz. The operating point of this device was selected to be 2.5V for both V_{GS} and V_{DS}, saturated with a significant overdrive voltage in order to minimize the non-quasistatic effects explained in Appendix A. This operating point was selected to allow for sizable signal signal without clipping effects. It should be noted that the DC operating point has a direct effect upon a transistor's cutoff frequency. A larger DC drain current will directly increase the device transconductance, thereby directly increasing the cutoff frequency as defined by (2.21).

Through this simulation procedure it was determined that a size of 200µm by 0.6µm (WxL) provided a device with the highest cutoff frequency in a 50Ω system. This cutoff frequency was found to be equal to ~13GHz, as shown Figure 2.11. The experimental setup used to determine this frequency is given in Figure 2.12.

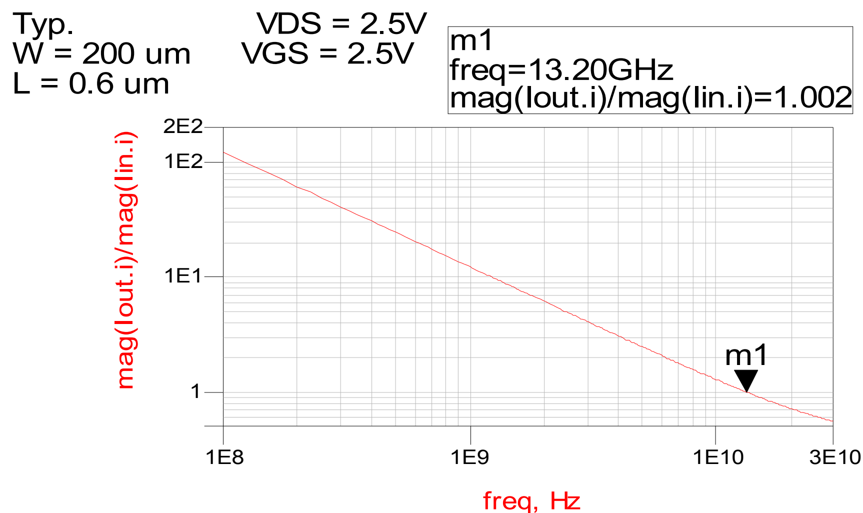

Figure 2.11 Unity-gain frequency of 200x0.6 µm (WxL) NMOS transistor (I_D = 31.1mA).

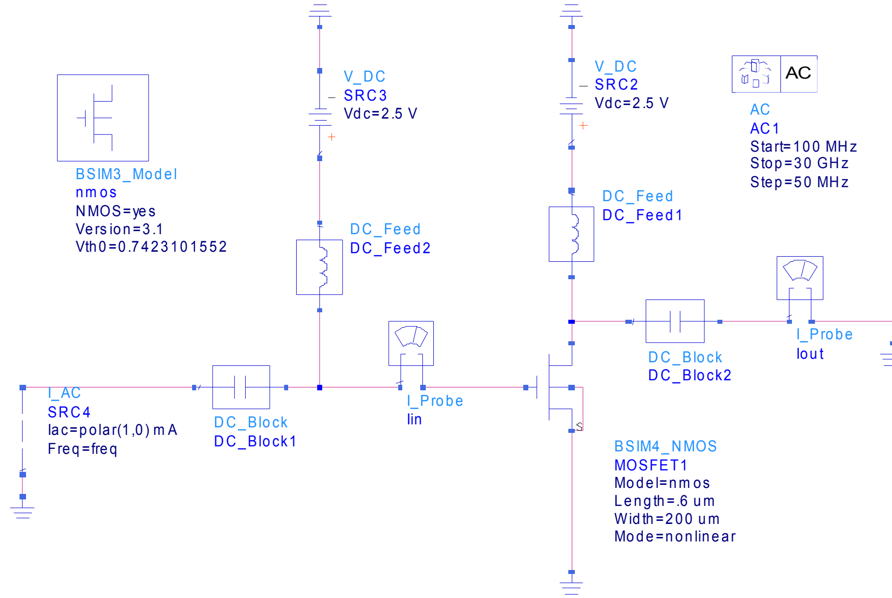

Figure 2.12 ADS simulation setup used to determine unity-gain frequency of NMOS.

The next step was to ensure that this particular transistor is stable throughout a reasonable frequency range. In terms of high-frequency amplifier design, stability demands that the input Γ_{IN} and output reflection Γ_{OUT} coefficients be less than unity, as expressed by the following relationships [18]

$$\Gamma_{IN} = \frac{Z_{IN} - Z_0}{Z_{IN} + Z_0} = S_{11} + \frac{S_{12}S_{21}\Gamma_L}{1 - S_{22}\Gamma_L} < 1 \qquad (2.26)$$

$$\Gamma_{OUT} = \frac{Z_{OUT} - Z_0}{Z_{OUT} + Z_0} = S_{22} + \frac{S_{12}S_{21}\Gamma_S}{1 - S_{11}\Gamma_S} < 1, \qquad (2.27)$$

where Z_{IN} and Z_{OUT} represent the input and output impedance of the transistor, S_{XX} denote the respective scattering parameters (S-parameters) of the device, and Γ_S and Γ_L represent

the reflection coefficients of the device source and load networks, respectively. It should be noted that the scattering parameters of each device will also exhibit Gaussian distributions due to effects of the process variations discussed above.

Stability assessment is readily accomplished using the Smith chart and visual cues known as stability contours. These contours, also referred to as stability circles, are arrived at by calculating those points that comprise the border between instability and stability as defined by (2.26) and (2.27). Consequently, this visualization results in two stability circles, one for the input and one for the output. These circles are characterized by their origin and radius as follows

$$C_L = \frac{\left(S_{22} - \Delta S_{11}^*\right)^*}{|S_{22}|^2 - |\Delta|^2} \tag{2.28}$$

$$r_L = \left|\frac{S_{12}S_{21}}{|S_{22}|^2 - |\Delta|^2}\right| \tag{2.29}$$

$$C_S = \frac{\left(S_{11} - \Delta S_{22}^*\right)^*}{|S_{11}|^2 - |\Delta|^2} \tag{2.30}$$

$$r_S = \left|\frac{S_{12}S_{21}}{|S_{11}|^2 - |\Delta|^2}\right| \tag{2.31}$$

where C_L, r_L, C_S, and r_S denote the center and radius of the load and center stability circles, respectively [18]. The Δ term in the above expressions is defined to be

$$\Delta = S_{11}S_{22} - S_{12}S_{21}. \tag{2.32}$$

In order to use stability circles to assess stability one must calculate the center of the circles (magnitude and phase) using (2.28) and (2.30), calculate the radius of the circles (magnitude) using (2.29) and (2.31), draw the contours upon the Smith chart, and assess whether the inside or the outside of the Smith chart is stable for each contour[18]. The last is accomplished for the load stability contour by setting $\Gamma_L = 0$, resulting in $\Gamma_{IN} = S_{11}$. If $S_{11} < 1$, then the center of the Smith chart is stable, otherwise the center of the Smith chart is unstable. For the source stability contour, set $\Gamma_L = 0$ to make $\Gamma_{OUT} = S_{22}$. Similarly, if $S_{22} < 1$, then the center of the Smith chart is stable, otherwise the center of the Smith chart is unstable.

The capability to quickly create stability contours and plot them on a Smith chart is built into the ADS suite. One can quickly plot a range of stability circles from the S-parameters of a simulated two port network using this feature. Using this feature the plot shown in Figure 2.13 was obtained by simulating the S-parameters of a single 200μm by 0.6μm (WxL) device in a 50Ω system from 0.5-5GHz in 0.5GHz steps. Both S_{11} and S_{22} were found to be less than one throughout this frequency range. Note that while the center of the Smith chart is a region of stability, above 50Ω there exists real impedances for which the system may exhibit instability. In order to judge the potentiality for an unstable system the gate of the transistor was loaded with a marginal series resistance (1Ω). The result of this simulation can be seen in Figure 2.14. Loading the gate of this transistor with a series resistance of ~1Ω or greater would thus ensure that the device is stable for all real impedances. As will be seen in the following chapter this criteria is met through the loading presented by the realized transmission lines.

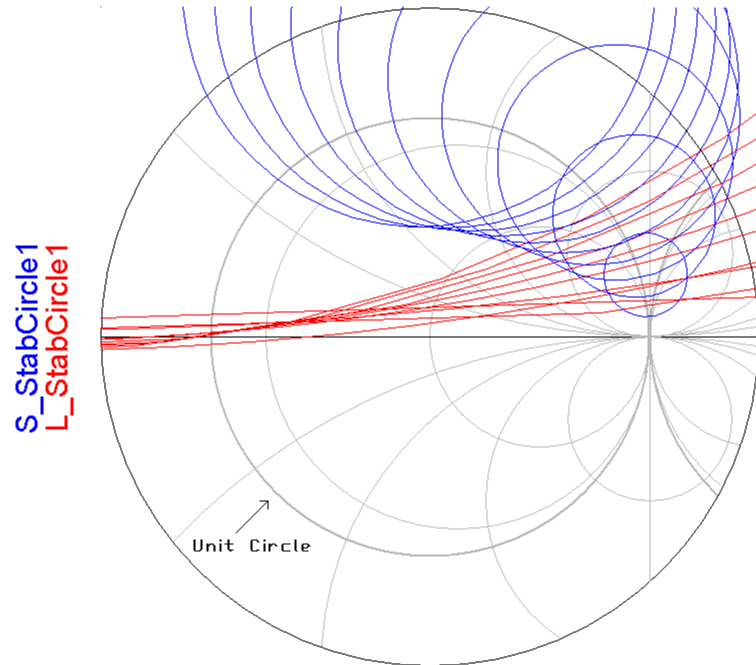

Figure 2.13 Source (blue) and load (red) stability contours of a single 200μm by 0.6μm (WxL) MOSFET.

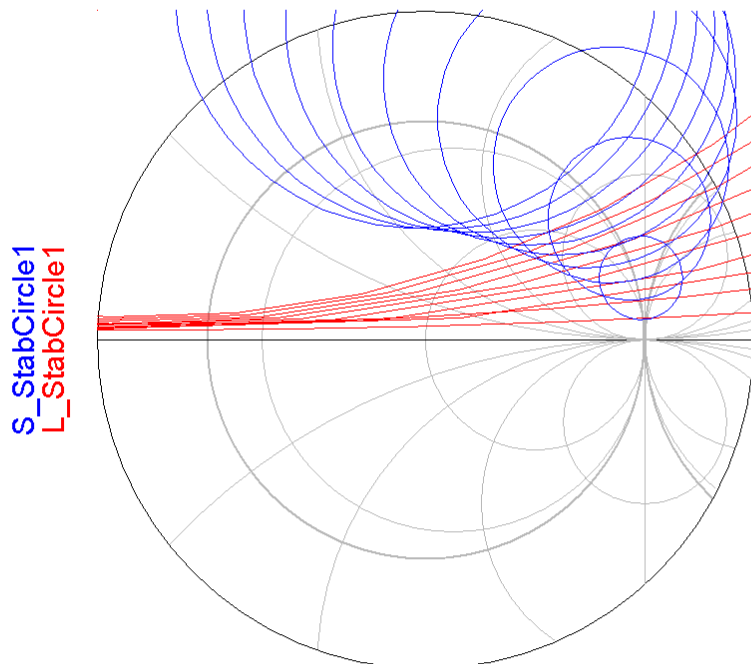

Figure 2.14 Source (blue) and load (red) stability contours of a single 200μm by 0.6μm (WxL) MOSFET loaded at the gate with a series resistance of 1Ω.

Once a transistor size and bias operating point is decided upon the design of the transmission lines can be undertaken using expressions 2.6 and 2.10 and the phase velocity equalization requirement addressed in expression 2.14. The focus of the subsequent chapter will be upon this design process.

CHAPTER 3
CMOS TRANSMISSION LINE REALIZATION

Transmission Line Parameters

Recall that the lumped-element equivalent circuit of a section of loaded transmission line is comprised of four primary parameters (the series resistance R_{EQ}, the series inductance L_{EQ}, the shunt conductance G_{EQ}, and the shunt capacitance C_{EQ},) encompassing the per unit length parameters of the TL itself and the "absorbed" parasitics of the loading transistors (Figure 2.7). Using this equivalent circuit the expressions for the characteristic impedances of the gate and drain lines were shown in the previous chapter to be

$$Z_g = \sqrt{\frac{Z}{Y}} = \sqrt{\frac{R_g + j\omega L_g}{G_g + j\omega (C_g + C_{gs}' / l_g)}}, \tag{3.1}$$

and

$$Z_d = \sqrt{\frac{Z}{Y}} = \sqrt{\frac{R_d + j\omega L_d}{G_d + \dfrac{1}{r_o l_d} + j\omega (C_d + C_M' / l_d)}}, \tag{3.2}$$

respectively. Knowing the transistor parasitic values and defining a design criteria for the system impedance allows one to realize the required unloaded TL parameters. The DC parasitic capacitances of the 200µm x 0.6µm (WxL) NMOS transistor obtained through SPICE simulation (and the subsequent calculation values of the Miller capacitance) are tabulated in Table 3.1.

Parameter	***Value***	***Unit***
Gate/Drain overlap capacitance, C_{gdo}	$6.0\text{x}10^{-14}$	F
Gate/Source overlap capacitance, C_{gso}	$6.0\text{x}10^{-14}$	F
Gate/Bulk capacitance, C_{gb}	$1.185\text{x}10^{-14}$	F
Gate/Drain capacitance, C_{gd}	$1.03\text{x}10^{-14}$	F
Gate/Source capacitance, C_{gs}	$2.683\text{x}10^{-13}$	F
Drain current, I_D	66	mA
Transconductance, g_m	75	mS
Miller capacitance (Gate), C_M	$1.698\text{x}10^{-13}$	F
Miller capacitance (drain), C_M'	$9.278\text{x}10^{-14}$	F

Table 3.1 DC parasitic parameter values of a 200µm x 0.6µm (WxL) NMOS transistor.

Coplanar Strip-line (CPS) Selection and Design

The choice of transmission line realization in CMOS technologies requires that the TL be able to be fabricated using the available photolithographic processes. This limitation typically restricts one's choice to those realizable via planar two-conductor geometries. Microstrip and coplanar waveguide (CPW) are two such geometries. The choice between these two geometries rests in the application desired. Microstrip lines demonstrate an advantage over CPW lines in that the ground plane provides intrinsic shielding from the lossy substrate (see Figure 3.1), lessening line losses due to capacitive substrate coupling.

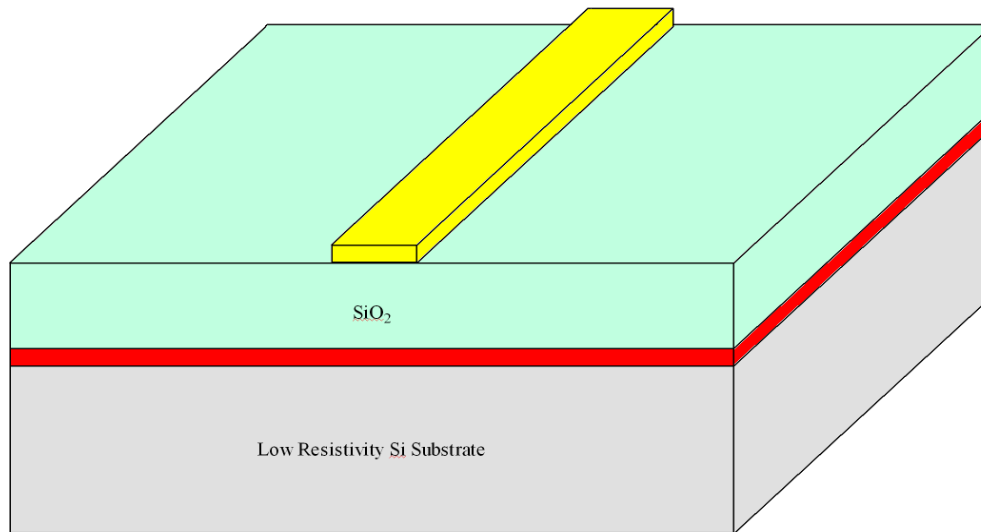

Figure 3.1 Microstrip transmission line realized in CMOS substrate using the highest (yellow) and lowest (red) metal interconnect layers.

In the same manner, the ground plane also provides the microstrip line designer with a measure of insensitivity to the processing done previous to the ground plane creation. These advantages aside however, microstrip is most often not the most suitable choice of transmission line structure in distributed CMOS designs. In the 3-metal CMOS process used in the DA design of this project the separation between the lowest metal layer (Metal 1) and the highest metal layer (Metal 3) is approximately 1.56μm (see substrate diagram in Figure 3.2).

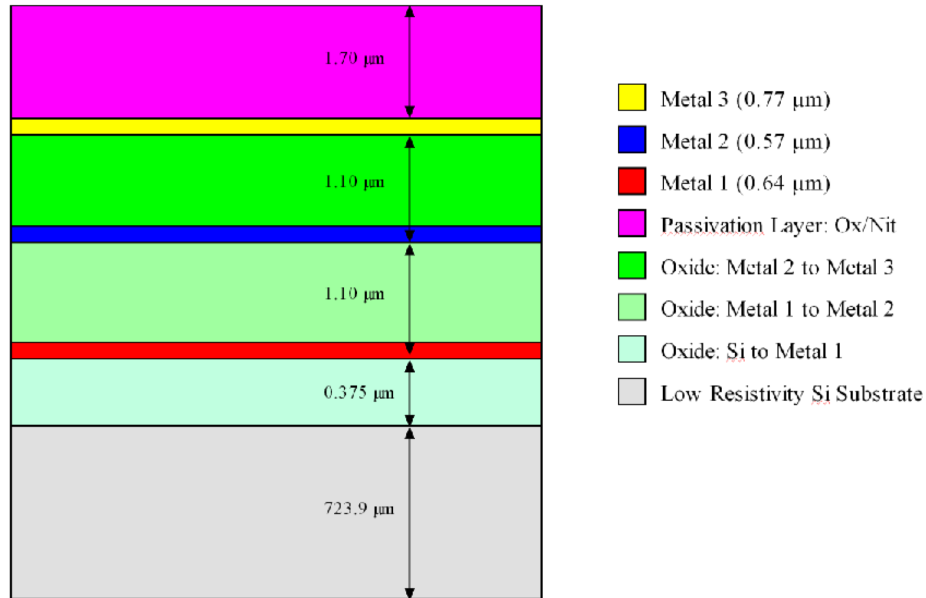

Figure 3.2 AMIS C5 process family substrate diagram.

This very modest separation distance between signal line and ground plane results in integrated microstrip lines having very small inductance per unit length parameters [19]. As such, microstrip lines fabricated in a typical CMOS technology will have very low inductive quality factors, resulting in increased line loss; the series and shunt quality factors of the microstrip can be extracted from the equivalent lumped-element model and defined as [19]

$$Q_L = \frac{\omega L}{R} \text{ and } Q_C = \frac{\omega C}{G}.$$

Consequently, CPW lines enjoy an advantage in that the geometry allows for an increased per unit length inductance. The higher L value is important in both allowing for the creation of a potentially lower loss line and in the context of the DA design, allows one to more readily satisfy the TL design requirements determined in Section 3.1.

One disadvantage to CPW lines is that the geometry requires two adjacent ground lines, see Figure 3.3, and thus can consume substantial amounts of die real estate. To avoid this costly consumption of die area the single adjacent ground line equivalent, coplanar stripline (CPS), can be chosen. CPS also enjoys the benefit of being able to attain higher characteristic impedances than that of CPW with equal resistive losses (e.g. using larger line widths) [20]. As mentioned in Chapter 2, the realization of high characteristic impedance TLs with tight tolerances can be difficult to realize in a commercial IC process technology due to fabrication process variation and intrinsic substrate variables such substrate resistance.

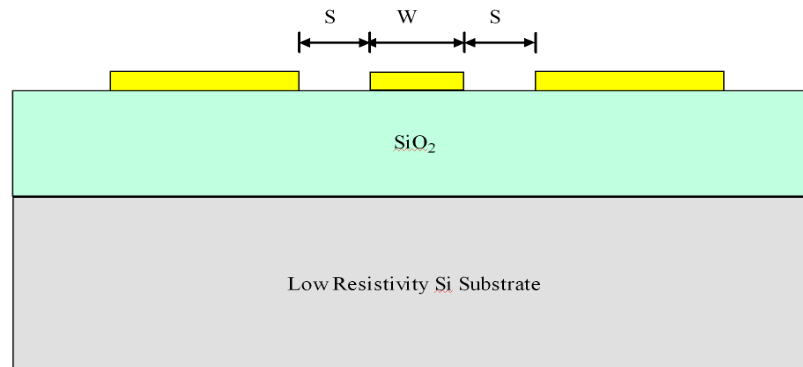

Figure 3.3 Coplanar waveguide cross-sectional illustration.

The design of the CPSs includes the selection of the line widths and spacing given the process parameters for the metal trace used and the resulting substrate; see Figure 3.4. This can be accomplished through the various analytical formulas developed for the analysis of coupled microstrip lines [21-23] and those specifically developed for the analysis of CPS [24-25]. The LineCalc program contained within the ADS suite uses those formulas developed by [22] and [23] to allow the user to quickly obtain electrical

and physical parameters of the coupled transmission lines of CPS geometries at specific frequencies of interest. The user supplies the program with the necessary substrate (effective dielectric constant **Er**, permeability **Mur**, and thickness **H**) and conductor (thickness **T** and conductivity **Cond**) parameters and selects a desired characteristic impedance for a selected design frequency and is returned the appropriate line widths and spacing.

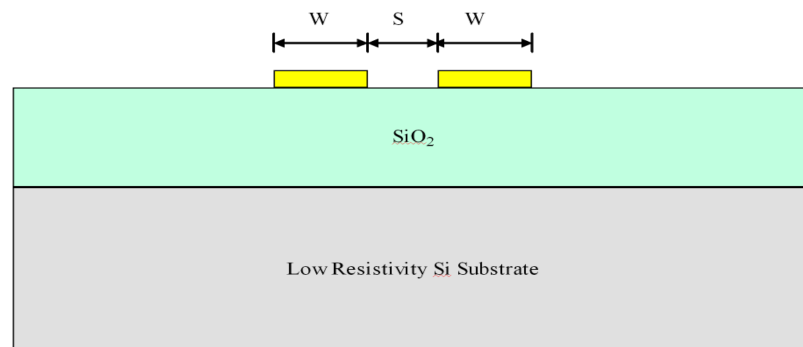

Figure 3.4 Coplanar stripline cross-sectional illustration.

The structural parameters used were obtained from the C5 process technology design rules and are shown graphically in Figure 3.2. In order to minimize the coupling effects between the CPS and the low-resistivity silicon substrate the top metal layer (Metal 3) was chosen for the implementation of the transmission lines. The process specifications as obtained from the design rules for this metal layer are given in Table 3.2. Note that the metal conductivity is found by simply dividing the sheet resistance R_S by the metal thickness t.

Parameter	***Min***	***Typ***	***Max***	***Unit***
Thickness, *t*	7000	7700	8400	Å
Sheet Resistance, R_S	33	40	47	m-ohms/sq
Electromigration (10yr life expectancy)	**85 ˚C**	**125 ˚C**		
Allowed current density per width	2.2 mA/µm	0.85 mA/µm		

Table 3.2 AMIS C5 process specifications for metal layer 3.

In order to determine the effective dielectric constant of the silicon substrate, silicon dioxide combination the method-of-moments (MoM) based electromagnetic (EM) simulator IE3D [26] was utilized in modeling the substrate shown in Figure 3.2 (minus the passivation layer). A simulation of an arbitrary uniform 2-port transmission line structure upon this substrate allowed the complex effective dielectric constant to be extracted versus frequency for use within LineCalc. An exact solution (W=48µm, S=4µm) for a 50Ω CPS implemented in the C5 process at a frequency of 1GHz was then deduced using the LineCalc program and constructed in IE3D for EM simulation. This frequency was chosen so as to minimize the error induced in the IE3D extraction of the RLGC parameters while still being high enough to maintain a reasonable idea of the high-frequency characteristics of the TL[3]. As such, using the RLGC extraction tool within IE3D, the lumped-element equivalent parameters were extracted for the CPS at 1GHz and can be seen in Table 3.3; see Appendix D for a complete extraction to 15 GHz.

3 IE3D uses an "Error Factor" term to give the user an indication of the relative error of an RLGC equivalent approximation for a segment of transmission line. This error factor (E) is defined to be equal to the square-root of the absolute value of the input impedance of the lumped-element circuit when the output is shorted over the input impedance with an open output. The relative error in an extraction can then be computed by the expression: $1 – sqrt(1 – E^2)*100\%$.

Parameter	***Value***	***Unit***
Frequency	1.000	GHz
Series R	0.99382	Ohms
Series L	0.27849	nH
Shunt R	6371.6	Ohms
Shunt C	0.11788	pF

Table 3.3 IE3D extracted RLGC parameters for a 500μm, 50Ω CPS.

The calculation of the characteristic impedance of this TL at 1GHz is thus given,

$$Z_0 = \sqrt{\frac{0.99382 + j2\pi(1e9)(2.7849e-10)}{\frac{1}{6371.6} + j2\pi(1e9)(1.1788e-13)}} = (50.946 - j7.901)\Omega ,$$

where

$$|Z_0| = 51.555\Omega .$$

Upon obtaining the RLGC values for the 50Ω CPS, the device parasitics were obtained through simulation at a frequency of 1GHz (Table 3.4) and applied to equations 3.1 and 3.2 in order to observe the loading effects upon the TL characteristic impedances. By inspection, one can see that the net effect of the device loading is to significantly lower the characteristic impedances of the gate and drain lines. Hence, the subsequent step is to increase the unloaded CPS characteristic impedances to the point at which the loaded lines would have a characteristic impedance of 50Ω. Observe from the data in Table 3.4 that the gate line must be designed to account for a larger loading capacitance than the drain line. This requires that the series resistance and/or series inductance of the

gate line be greater, leading to a potential disparity in both attenuation and phase velocity between the two lines.

Parameter	***Value***	***Unit***
Gate Capacitance	3.39×10^{-13}	F
Drain Capacitance	3.22×10^{-13}	F
Drain current, I_D	66	mA
Transconductance, g_m	75	mS

Table 3.4 Parasitic parameter values of a 200μm x 0.6μm (WxL) NMOS transistor at 1GHz.

Through an iterative process of selecting new width and spacing values for increasing values of characteristic impedances using LineCalc, extracting the RLGC parameters via full-wave EM simulation in IE3D, and applying equations (3.1) and (3.2), device loaded 50Ω CPS were created for both the gate and drain lines. The width, spacing, and unloaded characteristic impedance of the gate and drain lines are given in Table 3.5 along with the extracted RLGC parameters for the two lines. Note that while (3.1) and (3.2) would seem to simply imply that increasing the series inductance is sufficient to equalize the impedances of the gate and drain TLs at 50Ω, it was discovered that increasing the spacing alone did not sufficiently increase the impedance of the respective lines and thus the widths of the TLs were also decreased. This departure from the predicted is attributed to substrate dependence not accounted for in (3.1) and (3.2).

Parameter	***Value***		***Unit***
-	Gate	Drain	-
Width	7.0	10.0	µm
Spacing	12.0	10.0	µm
Z_O	140.823	116.171	Ω
Frequency	1.000	1.000	GHz
Series R	5.7324	4.0289	Ω
Series L	0.50907	0.44292	nH
Shunt R	1.1102e5	71303	Ω
Shunt C	0.026784	0.03431	pF

Table 3.5 IE3D extracted RLGC parameters for 500µm gate and drain CPS.

Including the parasitic capacitances from Table 3.4 into the RLGC extracted parameters in Table 3.5 yields a calculated complex gate line impedance of

$$Z_g = \sqrt{\frac{5.7324 + j2\pi(1e9)(5.0907e-10)}{\frac{1}{1.1102e5} + j2\pi(1e9)\left(\left(2.6784e-14\right) + \left(3.40e-13\right)\right)}} = (46.076 - j26.933)\Omega\ ,$$

where

$$\left|Z_g\right| = 53.37\Omega\ ,$$

and a complex drain line impedance of

$$Z_d = \sqrt{\frac{4.0289 + j2\pi(1e9)(4.4292e-10)}{\frac{1}{71303} + j2\pi(1e9)\left(\left(3.431e-14\right) + \left(3.22e-13\right)\right)}} = (41.482 - j21.597)\Omega\ ,$$

where

$$|Z_d| = 46.77\Omega\,.$$

After determining the appropriate geometries for the respective lines, the disparity in phase velocities between the two was then addressed. The phase velocity of a signal traveling upon a TL can be expressed as [13]

$$v_p = \frac{1}{\sqrt{L \cdot C}}. \tag{3.3}$$

Combining (3.3) with the expression for the characteristic impedance of a lossless TL,

$$Z_0 = \sqrt{\frac{L}{C}}, \tag{3.4}$$

allows ones to obtain expressions for the phase velocities upon both the gate,

$$v_{p_{GATE}} = \frac{Z_0}{L_G}, \tag{3.5}$$

and drain lines,

$$v_{p_{DRAIN}} = \frac{Z_0}{L_D}. \tag{3.6}$$

Observing (3.5) and (3.6) allows to to note that the larger series inductance of the gate line L_g introduces additional phase delay, thus making it necessary to increase the

delay incurred in the drain line by an equal amount. This can be easily accomplish by increasing the length l_d of the drain line sufficiently to satisfy the relationship

$$\frac{L_g}{L_d} = \frac{l_d}{l_g}. \tag{3.7}$$

Satisfying this relationship results in a drain line length of 575µm. In order to facilitate layout the drain line was designed to occupy the same horizontal distance (500µm) as the gate line by including two jogged sections in the drain line. A micrograph of the gate and drain lines can be seen in Figure 3.5.

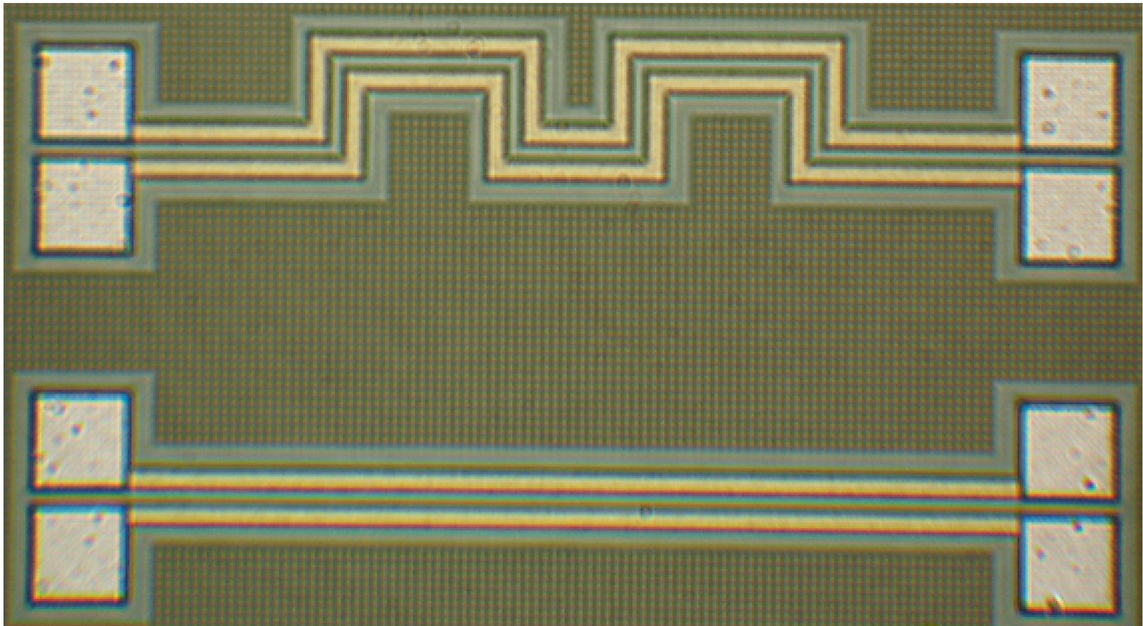

Figure 3.5 Micrograph of the fabricated gate and drain CPS.

Optimal Device Quantity Deduction

Once the characteristics of the gate and drain TLs are known, it is then possible to derive the optimal number of stages the DA should be designed for using (2.20). The electromagnetic simulator IE3D was used to extract the attenuation factors of each line. Knowing these, along with the intermediary lengths, allowed (2.20) to be used to find the optimal number of stages as follows:

$$M(G_{MAX}) = \frac{\ln(\alpha_g l_g / \alpha_d l_d)}{\alpha_g l_g - \alpha_d l_d} = \frac{\ln\left[\dfrac{\left(0.9161\dfrac{1}{\text{mm}}\right)(500\,\mu\text{m})}{\left(0.92262\dfrac{1}{\text{mm}}\right)(575\mu\text{m})}\right]}{\left(0.9161\dfrac{1}{\text{mm}}\right)(500\,\mu\text{m}) - \left(0.92262\dfrac{1}{\text{mm}}\right)(575\mu\text{m})} = 2.03.$$

An optimal stage number of two is thus arrived at for a starting design point. Following this determination the DA design was simulated in ADS using the appropriate models. The transistors were modeled using the provided BSIM3v3 models, while the transmission line structures were modeled using the method-of-moments based electromagnetic simulator present within ADS entitled Momentum. It was discovered during these simulations that in fact six stages could be implemented before the attenuation in the TLs overcame the gain improvements resulting from the addition of active devices. A 50Ω system consisting of six CPS delay line connected 200µm by 0.6µm (WxL) multi-fingered MOSFET transistors was thus decided upon as the final DA design configuration. At this point in the design each device was optimally biased by individual RF-choked voltages sources. The subsequent chapter will address feasible means of biasing these devices on-chip via an external voltage source.

CHAPTER 4
BIASING AND PLANAR INDUCTOR DESIGN

Distributed Amplifier Biasing

In order to realize a fully integrated distributed amplifier the bias network must necessarily be realized on chip as well. Previous implementations of distributed amplifiers in conventional CMOS technologies have relied upon bias-T [27-28] and package parasitics [29] to implement the requisite RF blocking mechanisms within the DA design. A primary focus of the DA design of this thesis was the implementation of a monolithic DA circuit topology. In addition, this work was carried out with the goal of realizing a DA sub-circuit that could be readily utilized within a larger 50Ω RF system design. Consequently, a biasing scheme for the six transistors comprising the amplifiers within the design was created to allow for simple system integration with minimal complexity power supply requirements.

The biasing method decided upon utilizes four square-spiral inductors (the selection and design of which is discussed in the subsequent section) acting as RF-chokes in the configuration shown in Figure 4.1. This configuration was chosen through a trial-and-error process starting from an optimal configuration in which RF-chokes were placed so that each device was provided immediate bias connections to the positive and negative power supply voltages as shown in Figure 4.2.

This implementation of the bias network was chosen over an implementation of the widely used analog building block, the current mirror, in order to achieve a bias network with the broadest frequency response in terms of device loading and

performance. The characteristics of various current mirror topologies has been shown have distinct frequency dependencies in [30]. The researchers in this publication demonstrated current mirror bandwidths not exceeding 2GHz through SPICE model simulations of a 0.8μm process. Simulation of smaller feature size (0.6μm and 0.35μm) processes are reported to attain slightly superior performance, though exact data is not given. The planar spiral inductor bias network achieves significantly larger performance bandwidths in simulation while presenting minimal complicating loading effects to the design of the input and output TLs.

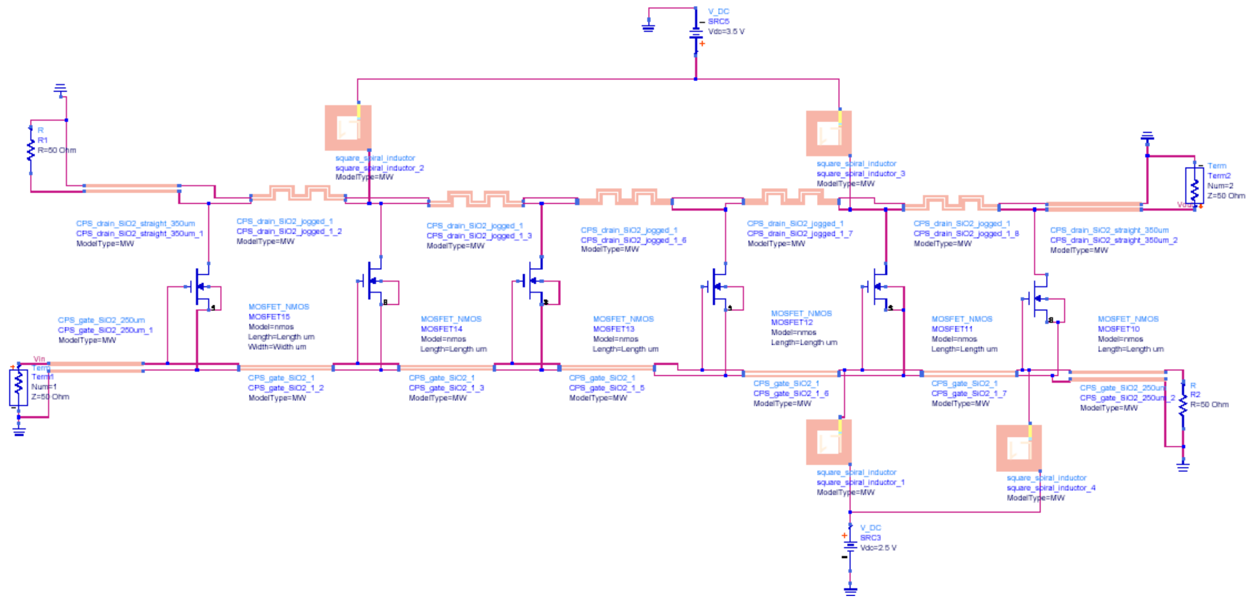

Figure 4.1 DA circuit with DC bias network realized with square-spiral inductors.

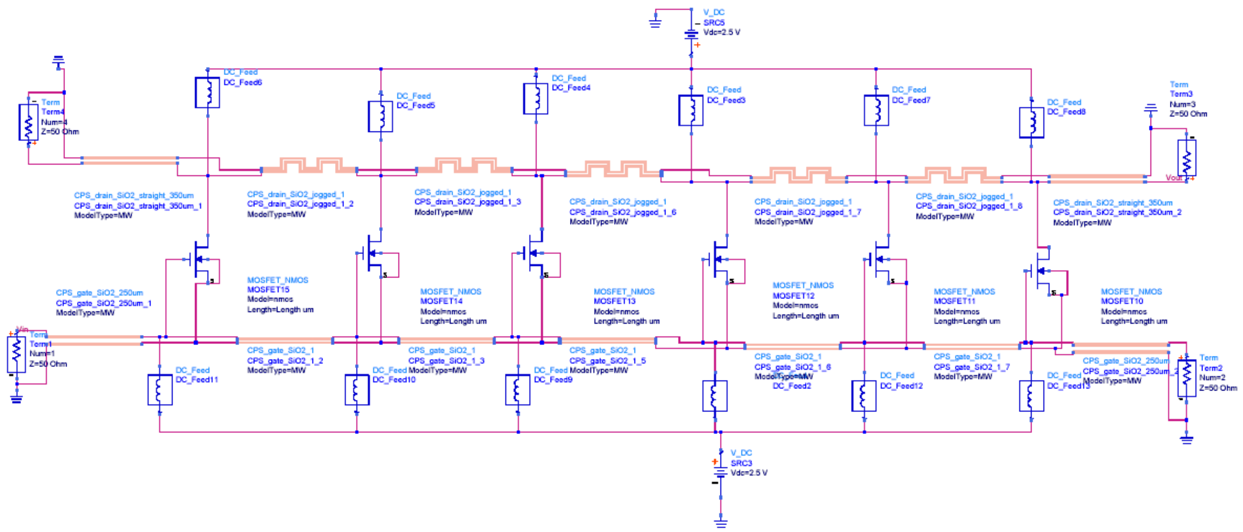

Figure 4.2 ADS schematic of DA circuit with an optimal DC bias network realized with ideal RF-chokes.

From this initial configuration, the loading effects of the square-spiral inductors were examined in order to determine the effects upon circuit performance. Initially it was believed that the bias inductors could easily be incorporated into the transmission line design, however, through simulation it was found that the imperfect RF-choke nature proved a greater detriment to the performance of the DA than the added inductive loading effects. The initial bias network provided an alternate route for the RF-signal resulting in considerable signal attenuation upon both the gate and drain lines. However, limiting the bias connections to single locations upon the respective transmission lines proved inadequate in terms of device biasing. Therefore it was determined through simulation that a pair of the designed square-spiral inductors provided a suitable balance between signal degradation and bias voltage levels experienced by each device. The attenuation experienced upon the lines also severely affected the supplied DC voltage level. From RF-input to the gate of the sixth transistor a 0.63V drop in DC potential was predicted

upon the gate line through ADS simulation when using a bias-T setup and 2.5V power supply voltages. Similarly, a 1.21V drop in voltage level on the drain line was simulated. Thus, the topology shown in Figure 4.1 was chosen as a comprise between the signal attenuation experienced and the DC voltage level supplied to each device. The actual design of the spiral inductors and simulated characteristics are discussed in the subsequent section.

Planar Spiral Inductor Design

Inductor implementations in commercial integrated circuit technologies are practically limited to either bond wires or planar spiral geometries. Bond wires typically provide higher Q values, typically an order of magnitude, and less resistive loss than planar spiral inductors but are typically limited in their inductance values by the bonding process and tend to not lend themselves to a well controlled inductance value [31]. Consequently, planar spiral inductors are customarily chosen for their well-defined inductance properties at the sacrifice of a limited Q-factor. For the reasons discussed in Section 4.1 the self-evident choice of inductor implementation was that of the planar spiral geometry type. The exact choice of polygonal layout is up to the designer and can range from the most simple square spiral, Figure 4.3a, to the wholly circular spiral, Figure 4.3d. Increasing the number of polygonal sides typically results in a higher Q inductor at the cost of a slightly decreased inductance value for the same design dimensions.

The planar inductors discussed forthwith are implemented using solely the top metal layer (M3). The reasons for this choice include a desire to minimize the coupling

effects between the inductor and the lossy silicon substrate and additionally, to minimize the power lost within trace. The latter reflects the process decision to relegate the top metal layer for such purposes as power routing and passive element realization. While multilayer realizations of planar spiral inductors demonstrating reduced areas for comparable inductance values can be found in literature [32-33], these designs typically employ more advanced processes which enjoy the advantage realized through the reverse thickness scaling of the CMOS interconnect stack (increased separation distance between interconnect layers and the silicon substrate resulting in reduced capacitive coupling effects). In addition, the conductivity of the initial and secondary metal interconnect layers within the AMIS C5 process are approximately half that of the third layer. This additional loss, in conjunction with the small interconnect stack distances, makes the creation of a high *Q*-factor multilayer inductor in the AMIS C5 a problem beyond the scope of this project.

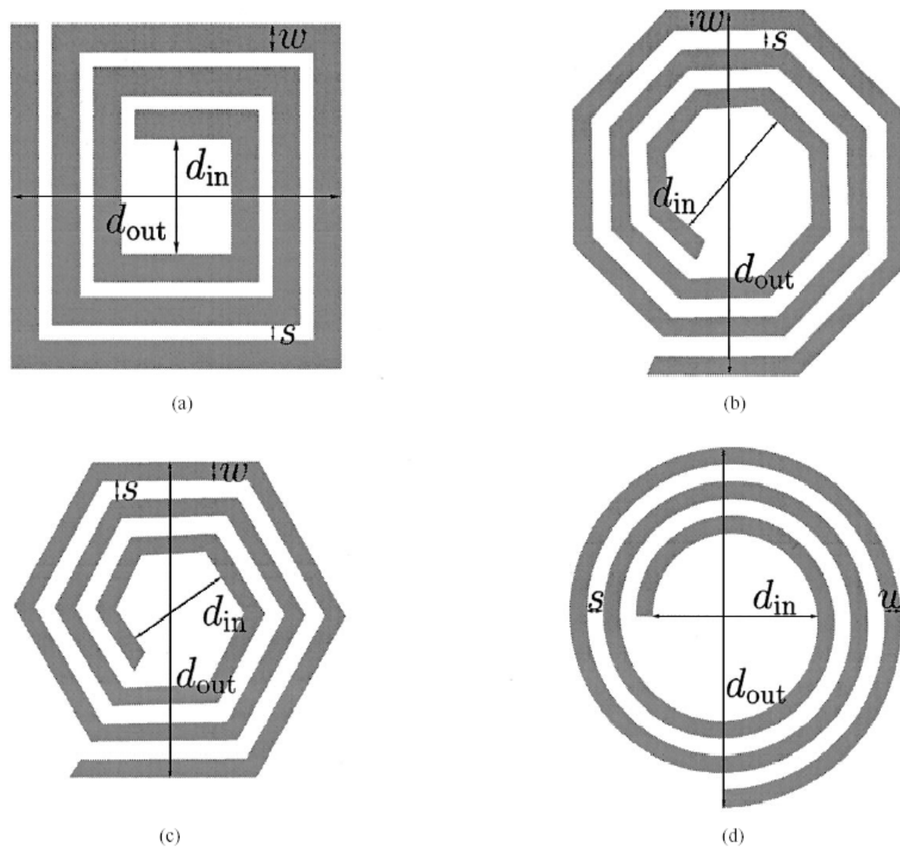

Figure 4.3 Planar spiral inductor geometries for (a) square, (b) hexagonal, (c) octagonal, and (d) circular realizations [31].

Inductor Figures of Merit

Passive inductor design includes several important FOM in realizing the inductor with the required properties. Foremost among these is of course the inductance itself. The most accurate method of obtaining the inductance is through the use of a three-dimensional (3-D) EM simulator such as [34]. Due to the significant computational run time required for such a simulation however, this approach is more useful as a characteristic validation step than as an initial design step. The use of approximate analytical expressions is thus the most desirable method for determining the geometry necessary to realize the required inductance value. Presented in [31] are three simple,

approximate expressions of planar spiral inductors of square, hexagonal, octagonal, and circular geometries. These expressions fully characterize the inductance of these geometries given the number of turns n, the line width w, the line spacing s, the average diameter d_{avg} ($0.5\cdot(d_{out} + d_{in})$) and the *fill ratio* ρ ($(d_{out} - d_{in})/(d_{out} + d_{in})$). The fill ratio is an indicator of how hollow the center of the spiral is. This is important in that an inductor with a fuller center will have a smaller inductance than one with a larger center spacing even while the two have the same average diameter due to the increased negative mutual inductance of the tighter inner turns of the first. One should also note that while these inner turns contribute less inductance they contribute no less series resistance, making it doubly important that a sufficiently large fill factor is maintained. A rule of thumb for a desirable fill factor value is approximately 0.5 [35]. Two of the expressions from [31] were selected for utilization in the analytical design of the required planar spiral inductors and will be discussed here.

The first, referred to as the modified Wheeler expression, takes the form

$$L_{mw} = K_1 \mu_0 \frac{n^2 d_{avg}}{1 + K_2 \rho}, \tag{4.1}$$

where K_1 and K_2 are the polygon dependent coefficients given in Table 4.1 and μ_0 is the permeability constant ($4\pi \times 10^{-7}$ [H/m]) [31].

Polygon	K_1	K_2
Square	2.34	2.75
Hexagonal	2.33	3.82
Octagonal	2.25	3.55

Table 4.1 Coefficients for modified Wheeler expression [31].

The second expression given by [31] is based on an approximation of the spirals as symmetrical current sheets of equivalent current densities and is shown to be given by

$$L_{gmd} = \frac{\mu_0 n^2 d_{avg} c_1}{2}\left(\ln(c_2/\rho) + c_3\rho + c_4\rho^2\right), \tag{4.2}$$

where the coefficients c_i are again polygon dependent; see Table 4.2.

Polygon	c_1	c_2	c_3	c_4
Square	1.27	2.07	0.18	0.13
Hexagonal	1.09	2.23	0.00	0.17
Octagonal	1.07	2.29	0.00	0.19
Circle	1.00	2.46	0.00	0.20

Table 4.2 Coefficients for current sheet expression [31].

Both approximations were shown to exhibit agreement with field solver inductance values and within ~3% and within ~5% for actual measured results by [31].

A second important FOM for planar spiral inductors is the series resistance of the inductor. The series resistance calculation of an planar spiral inductor realized in a typical CMOS technologies must account for losses incurred by the capacitive coupling of the metal layer to the substrate in the form of *eddy current*, in addition to the typical

wire calculations accounting for the finite conductivity of the metal and its frequency dependent skin depth. As such the total series resistance can be approximated by the expression

$$R_S = \frac{l}{w \cdot \sigma \cdot \delta \left(1 - e^{-t/\delta}\right)} + \frac{\sigma_{sub}}{4e}\left(\mu \cdot n \cdot f\right)^2 d_{avg}^3 \rho^{0.7} z_{n,ins}^{-0.55} z_{n,sub}^{0.1}, \tag{4.3}$$

where the first term accounts for the finite metal conductivity and skin depth effects and the second term accounts for the induced eddy current losses [35]. The individual variables are defined as follows: w is the metal width, σ is the metal conductivity, l is the total length of the winding, t is the metal thickness, δ is the skin depth given by

$$\delta = \sqrt{\frac{2}{\omega \cdot \mu_0 \cdot \sigma}}, \tag{4.4}$$

σ_{sub} is the substrate conductivity, e is the real number constant equal to 2.7182..., and $z_{n,ins}$ and $z_{n,sub}$ are the total thickness of the insulation between the metal layer and the conductive substrate and the substrate skin depth (both normalized to d_{avg}), respectively [35].

Once the series inductance and resistance are computed a first-order approximation of the inductor's Q-factor can be made by using the quality factor definition to relate the energy stored per cycle to the energy lost per cycle. This relationship can be expressed simply as

$$Q_L = \frac{\omega L_S}{R_S}, \tag{4.5}$$

where L_S is the series inductance predicted by (4.1) or (4.2) and R_S is the series resistance approximated by (4.3).

The final FOM significant to the implementation of a suitable RF-choke is the inductor's frequency of self-resonance (SRF). This frequency is defined to be the point at which the inductor's Q value is equal to zero. At frequencies beyond this point the inductor takes on an impedance that is capacitive in nature eventually negating its usefulness as an RF-choke. Consequently, the inductor must be designed such that its SRF is sufficiently high as to not inhibit the broadband capabilities of the DA itself. This requirement in and of itself is not a trivial matter and is further complicated by the increased capacitive losses due to the low-resistivity substrate. However, due to the low Q-factors (< 2) of the planar spiral inductors realizable in the process used, the SRF did not need to be placed at the upper end of the DA's expected bandwidth.

In considering the implementation of a planar spiral inductor to serve as a suitable RF-choke in regards to the design of a broadband DA the three FOM visited above are weighed in order to achieve an inductor that simultaneously achieves a sufficiently high SRF, an inductance value large enough to mitigate the propagation of phase-incoherent RF signals through the bias network, and a minimal DC series resistance.

Planar Spiral Inductor Implementation

The limitations of the Cadence suite [36] used in this project restricts the geometry of any structure to one with 45° turns, thus limiting the polygon choice to

hexagonal or square. In order to facilitate rapid design iterations a square topology was chosen. In addition, a maximum outer diameter of 450µm was decided upon in order to ensure that the final die cost did not exceed ~5000USD[4]. With this restriction in mind the computer algebra system distributed by Mathsoft entitled Mathcad was used to simultaneously implement equations (4.1), (4.2), (4.3) and (4.5) in order to determine the dimensions of a square spiral inductor that achieved the greatest inductance value possible while maintaining an SRF near 5GHz. These constraints led to the determination of an inductor with the following dimensions: d_{out} = 447.7µm, d_{in} = 213.3µm, w = 24.5µm, s = 2.0µm, and n = 4.25 (see Appendix E for Mathcad derived plots used to graphically weigh the dimensional constraints against the desired inductance values). Momentum was then used to model the inductor and obtain the following important inductor FOM via the S-parameters: an inductance value of ~10nH, a DC series resistance of ~9.8Ω, and a SRF of ~4.5Ghz.

4 MOSIS MEP Research Account price for the 0.5µm AMIS C5 process listed at $650*(die size in mm^2), http://www.mosis.org/orders/prices/mep/.

CHAPTER 5
CALIBRATION AND CHARACTERIZATION

Introduction

As previously mentioned this work was carried out with the goal of realizing a DA sub-circuit that could be readily utilized within a larger RF system design. To that end, the parts fabricated were designed to enable a probed response to be easily acquired and used to characterize the operation of the DA device, the sub-circuits, and all associated passive elements. All measurements were conducted in the on-wafer high-frequency test facility housed in the Microwave and mm-Wave Electronics Laboratory at Montana State University – Bozeman. This facility is home to a Cascade Microtech Microchamber Probe Station and a N5250A mm-wave vector network analyzer (VNA) from Agilent Technologies. Available for on-wafer probing at the facility are four DC positioners (and associated probes) from Cascade Microtech and three model 40A CPS RF Picoprobes from GGB Industries Incorporated. The footprint of the available RF probes is an important factor that must be considered during the layout of all components to be probed. A diagram of the tip configuration of the laboratory's probes is shown in Figure 5.1. The probes are of a ground-signal (GS) and signal-ground (SG) configuration with a pitch (tip separation) of 50μm.

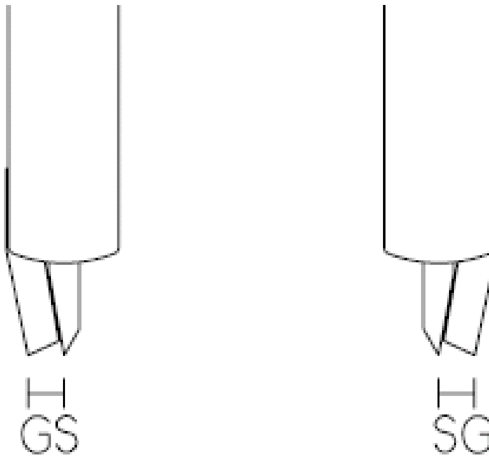

Figure 5.1 GGB model 40A CPS RF probe tip diagram.

Calibration

The first task to be completed during a measurement is that of calibration. Calibration is the procedure of removing sources of measurement error, at least to the extent possible. Calibration is separated into two types, response calibration and vector calibration [37]. Response calibration is limited to the correction of scalar errors, while vector calibration corrects for both magnitude and phase errors. When performing any type of device measurement there will be sources of error present that will affect the measurement data obtained. This measurement error can be grouped into three general types of error: drift, random, and systematic [37]. Drift error is caused by system variations over time that occurs *after* a calibration has been completed. This type of error is both time and temperature dependent and depends heavily on the robustness of the test system present. Minimizing drift error is accomplished by maintaining both a constant test environment and regular system validation procedures as prescribed by the device manufacturer. A simple but important task in this regard is to incorporate a warm-up

period for active test equipment into the calibration procedures in order to allow the equipment to reach thermal equilibrium. Random errors are by definition those that are completely unpredictable by nature and cannot be removed through calibration. The operator typically has no control of this type of error, as it chiefly depends upon the noise present within the test instruments themselves. Finally, systematic errors are those due to imperfections in the test instruments and test setups that are repeatable and time-invariant. Consequently, the contribution of systematic errors are readily characterized and used to create equivalent error boxes. During measurements of the device-under-test (DUT) these error boxes can then be used to mathematically remove the systematic error contributions.

The systematic error boxes are determined by measuring known calibration standards. A specific calibration kit (cal-kit) consisting of the set of known standards is used for this purpose. These standards typically involve some combination of reflects (opens and shorts), terminations, and thrus. Perfect opens and shorts reflect 100% of the incoming waves, ideal terminations absorb 100% of the incident waves, and error-less thrus fully transmit the signal with no attenuation or phase change. The disparities of the standards within the cal-kit to that of perfect standards are characterized and stored as calibration coefficients within the cal-kit definition file. The calibration coefficient definition file stored within the VNA is then used in conjunction with the standard measurements to form the 6-term (directivity, source match, load match, reflection tracking, transmission tracking, and crosstalk) reflection and transmission error boxes [37]. Thus, a full 2-port calibration requires a 12-term error correction model.

The type of calibration standards to be used defines the mathematical derivation

actually performed in order to arrive at these error boxes. Different derivation methods and the associated impedance standards make up the various calibration techniques existent in device characterization and measurement today. During the course of the measurements carried out in this work the two most common (SOLT and TRL) calibration techniques were effected.

Short-Open-Load-Thru (SOLT)

In a SOLT calibration there are four known reference standards, a short, an open, a load, and a thru. The accuracy of these standards directly correlates to the accuracy of a SOLT calibration, the more precise the standards, the more accurately the systematic errors can be defined [38]. This direct dependency upon the accuracy of the standards proves the SOLT method's greatest liability. It is often difficult to build easily defined calibration standards in the variety of TLs used today, with the problem becoming increasingly difficult to maintain at higher frequencies. For example, in CPS measurements the opens will radiate energy and the shorts will have an measurable inductance associated with them.

During this work a SOLT calibration was performed from 10MHz to 5GHz using a GGB calibration substrate (CS-8). This calibration placed the reference plane at the probe tips and does not de-embed any of the on-chip parasitics. To assess the quality of the calibration both a thru standard and a short standard were measured after calibration. Figure 5.2 shows a representative set of S-parameters of a 400μm thru line from the CS-8 calibration substrate after calibration. Return loss of better than 60dB is seen throughout virtually the entire frequency range (10MHz – 5GHz), suggesting an excellent calibration.

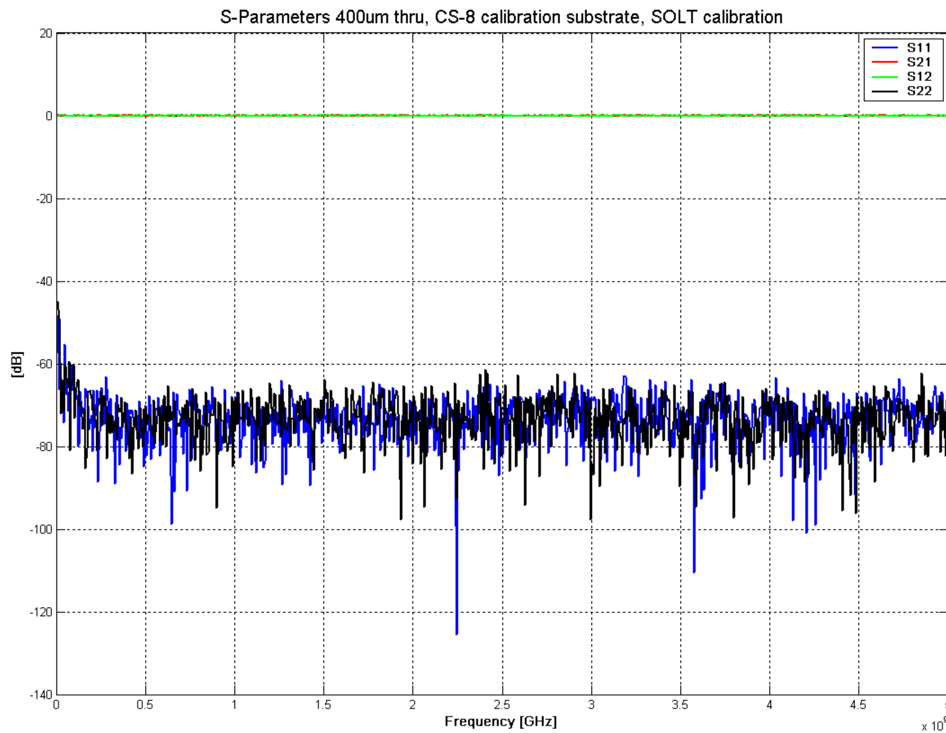

Figure 5.2 Measured 2-port S-parameters of a CS-8 thru line after SOLT calibration.

Similarly, Figure 5.3 shows the reflection from a short circuit on the CS-8 calibration substrate after the SOLT calibration upon a Smith chart. The frequency range shown in Figure 5.3 is 10MHz to 1GHz. From this figure it is again clear that the error correction model arrived at from SOLT calibration is in excellent agreement in terms of both magnitude and phase.

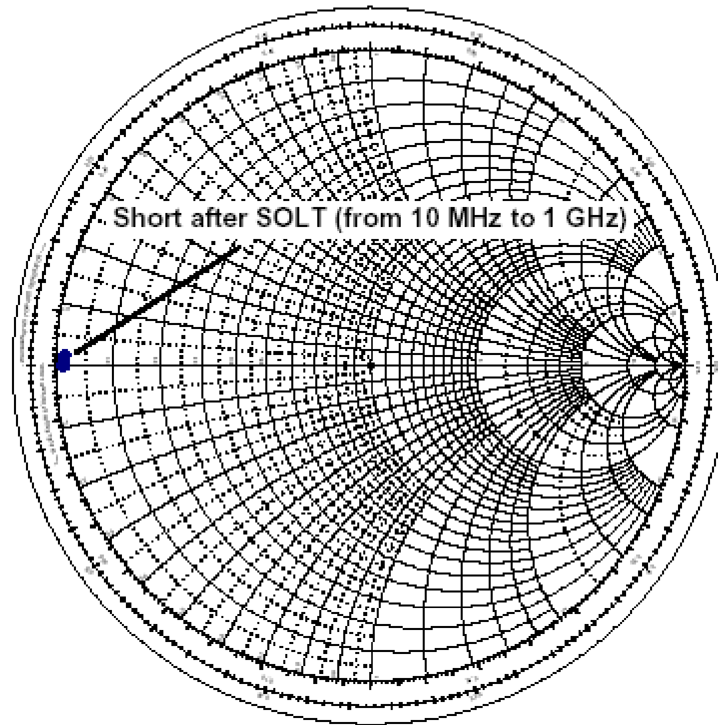

Figure 5.3 Measured reflection from a CS-8 short circuit after SOLT calibration.

Thru-Reflect-Line (TRL)

In order to circumvent the shortcomings of the SOLT calibration techniques, several methods have been developed requiring reduced numbers of well-defined standards. The TRL calibration method is perhaps the most popular alternative. This technique relies on the use of multiple transmission lines in place of the discrete impedance standards [39]. It requires only three simple standards, a short section of TL to connect ports 1 and 2 (the thru), identical high-reflection opens or shorts (the reflects) for both ports, and a second longer section of TL to connect ports 1 and 2 (the line). As such an immediate advantage of the TRL method lines in the relative ease of designing the required cal-kit. Also, only the first standard, the thru, need be precisely-defined for an accurate derivation of the 12-term error correction model using the TRL calibration

technique [38]. Consequently, the characteristic impedance of the thru line must be designed for that of the device to be measured in order to avoid measurement error.

In addition the optimal electrical length of the thru line is said to be 90° at the center frequency of bandwidth over which the device is desired to be characterized [38]. The length of the line is optimally defined to 90° greater than that of the thru at the center frequency, with a typical useful frequency range of 20° to 160° [38]. The bandwidth of a TRL calibration is thus limited by the line standard used. Larger bandwidth require the use of additional line standards. The required line length likewise restricts the usefulness of the TRL calibration technique to the higher RF frequencies as the length becomes prohibitively large at lower frequencies.

On-chip calibration standards were designed and fabricated on the DA die to facilitate a TRL calibration to the probe tips. The standards designed included 50Ω thru CPS of length 500μm, open and short reflects terminating 250μm CPS, and a 4686μm CPS line (see Figure 5.4). This TRL calibration places the reference plane at the center of the thru line, thus making it an ideal method in which to de-embed TL effects right up to the DUT.

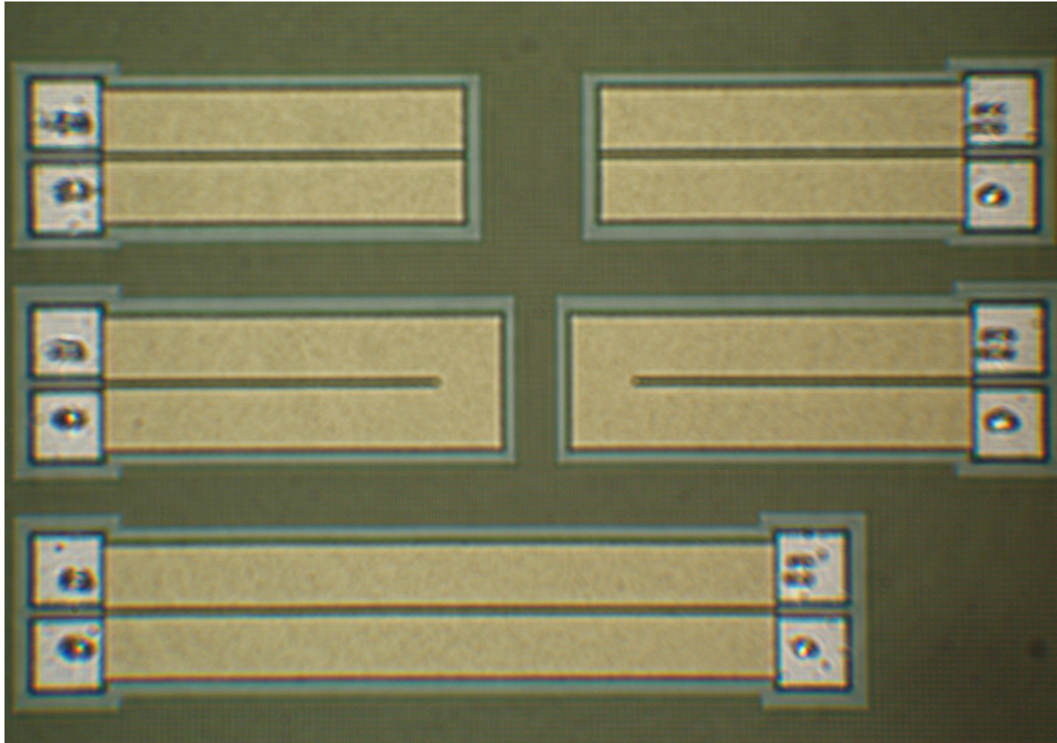

Figure 5.4 Micrograph of the fabricated CPS TRL calibration standards; TOP-open reflects, MIDDLE-short reflects, BOTTOM-thru line.

The guided wavelength of the 50Ω thru line is given by,

$$\lambda_g = \frac{c}{f\sqrt{\varepsilon_{eff}}} = \frac{3\times 10^8[m/s]}{f\sqrt{5.57}}, \quad (5.1)$$

where the effective dielectric constant (ε_{eff}) of 5.57 was estimated from IE3D simulation of the transmission line. The optimal line length was previously mentioned to be equal to 90º (λ/4) greater than the length of the thru line at the center frequency. Given the fabricated line lengths of 500μm and 4686μm the center frequency of this TRL cal-kit is calculated to be

$$f_{\lambda_g/4} = \frac{1}{4}\frac{c}{(l_{line} - l_{thru})\sqrt{\varepsilon_{eff}}} = \frac{1}{4}\frac{3\times 10^8[m/s]}{(4686\mu\text{m} - 500\mu\text{m})\sqrt{5.57}} = 7.6\text{GHz}. \tag{5.2}$$

Using the rule of thumb from [38] the range of acceptable calibration performance around this frequency is calculated as follows

$$f_{\lambda_g/18} = \frac{1}{18}\frac{c}{(l_{line} - l_{thru})\sqrt{\varepsilon_{eff}}} = \frac{1}{18}\frac{3\times 10^8[m/s]}{(4686\mu\text{m} - 500\mu\text{m})\sqrt{5.57}} = 1.7\text{GHz}, \tag{5.3}$$

$$f_{4\lambda_g/9} = \frac{4}{9}\frac{c}{(l_{line} - l_{thru})\sqrt{\varepsilon_{eff}}} = \frac{4}{9}\frac{3\times 10^8[m/s]}{(4686\mu\text{m} - 500\mu\text{m})\sqrt{5.57}} = 13.5\text{GHz}, \tag{5.4}$$

where the acceptable TRL calibration bandwidth is calculated as

$$\text{BW} = f_{4\lambda_g/9} - f_{\lambda_g/18} = 13.5\text{GHz} - 1.7\text{GHz} = 11.8\text{ GHz}.$$

However using the program FINDLEN offered by the NIST[5], it was found the maximum standard deviation for this frequency range is equal to ~2.91. In personal communication with Dr. Dylan Williams of NIST it was recommended that this range be reduced until a max standard deviation of ~1.0 was achieved. With the available line standards and a complex ε_{eff} equal to 4.785659 – j2.822164 at 7.6GHz it was found that a minimum max standard deviation of 1.10 resulted from a frequency range of 6.75GHz – 8.25GHz. This is significantly tighter than former acceptable bandwidth.

A TRL calibration was performed over this bandwidth using the iterative calibration algorithm [40] implemented in the software package StatistiCAL™ (see

5 National Institute of Standards and Technology, Electronics and Electrical Engineering Laboratory, Radio-Frequency Electronics Group (http://www.boulder.nist.gov/div818/81801/dylan/software.html).

previous footnote for website) offered by NIST. The StatistiCAL package allows one to readily acquire ASCII text data from a VNA in the format:

frequency Re(S_{11}) Im(S_{11}) Re(S_{21}) Im(S_{21}) Re(S_{12}) Im(S_{12}) Re(S_{22}) Im((S_{22}),

where S_{ij} are measured S-parameters and the value of the frequency must be in gigahertz. Using this raw data StatistiCAL generates a solution (the error boxes) to the VNA calibration problem using an algorithm based upon orthogonal distance regression as implemented in ODRPACK [41] given starting point estimates for the effective dielectric constant and the magnitude, phase, and time delay of S_{ij} at the first frequency point within the measurement range. Figures 5.5 and 5.6 show 2-port S-parameters of the on-chip thru line and a Smith chart of the reflection from both a short and an open after an on-chip TRL calibration using StatistiCAL. Note that these figures indicate that a reasonable error correction model was also derived during the TRL calibration procedure.

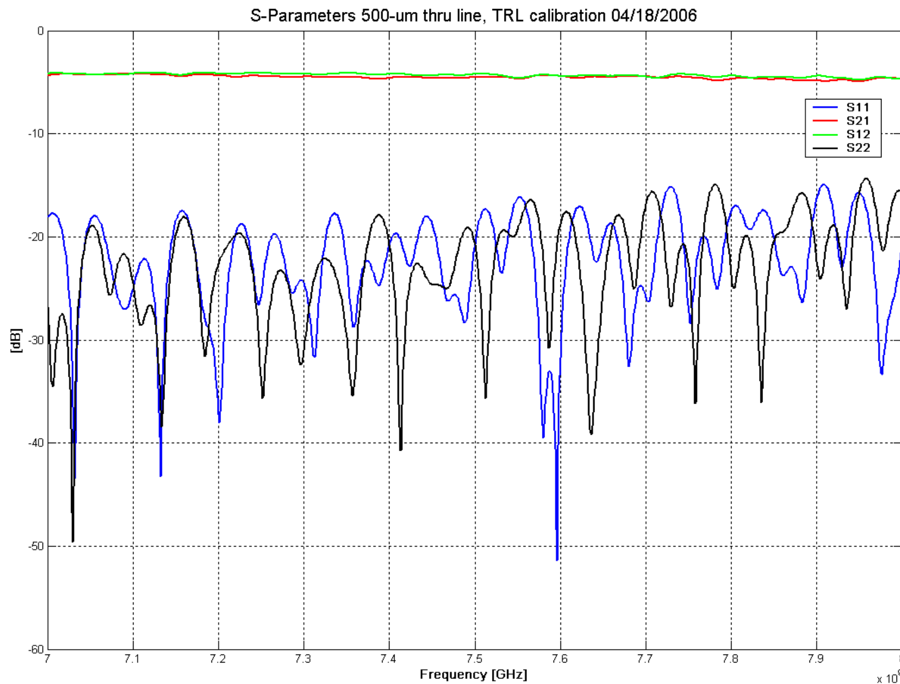

Figure 5.5 Two-port S-parameters of an on-chip thru line after TRL calibration.

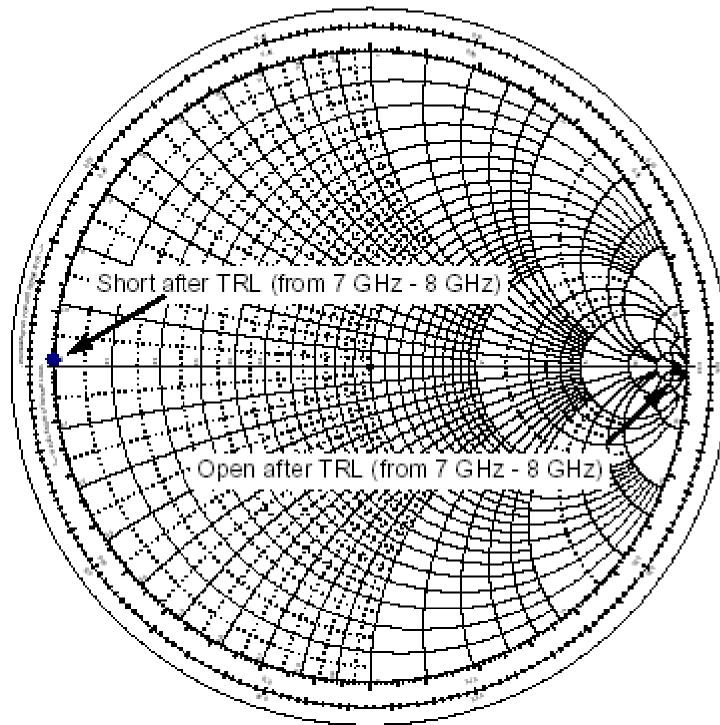

Figure 5.6 Input impedances of on-chip short and open reflects after TRL calibration.

Measurements

Delay Line Validation

In order to ensure that the phase velocities of the fabricated gate and drain lines corresponded to that of the electromagnetic simulated models, isolated sections of each were fabricated and probed after an SOLT calibration (see Figure 5.7). The simulated phase delay difference between the drain delay line and the gate line was predicted to vary from nearly 0º at 10MHz to approximately 1.7º at 5GHz (see simulation schematic and results shown in Figures 5.8 and 5.9, respectively).

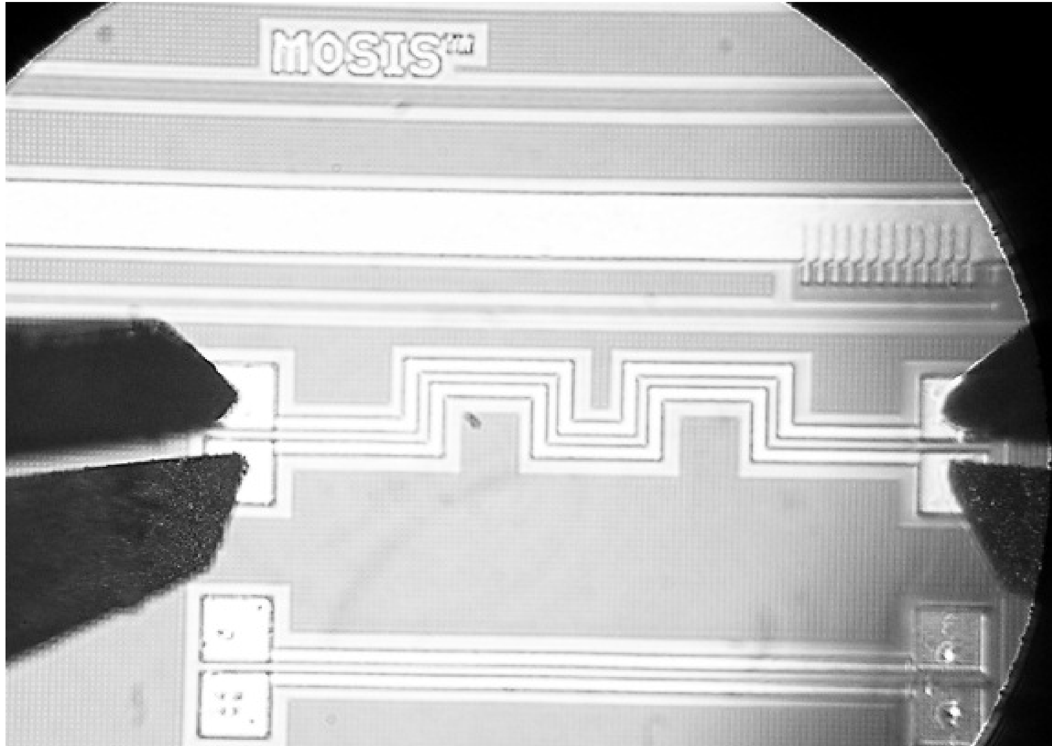

Figure 5.7 Micrograph of an isolated drain delay line being probed after SOLT calibration.

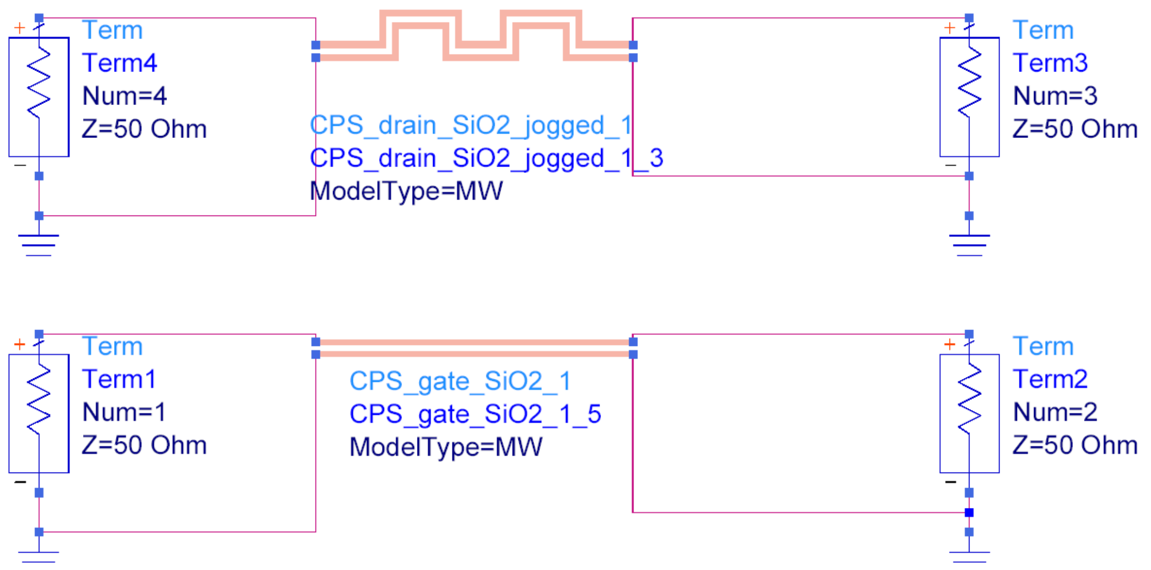

Figure 5.8 ADS delay line phase difference simulation schematic.

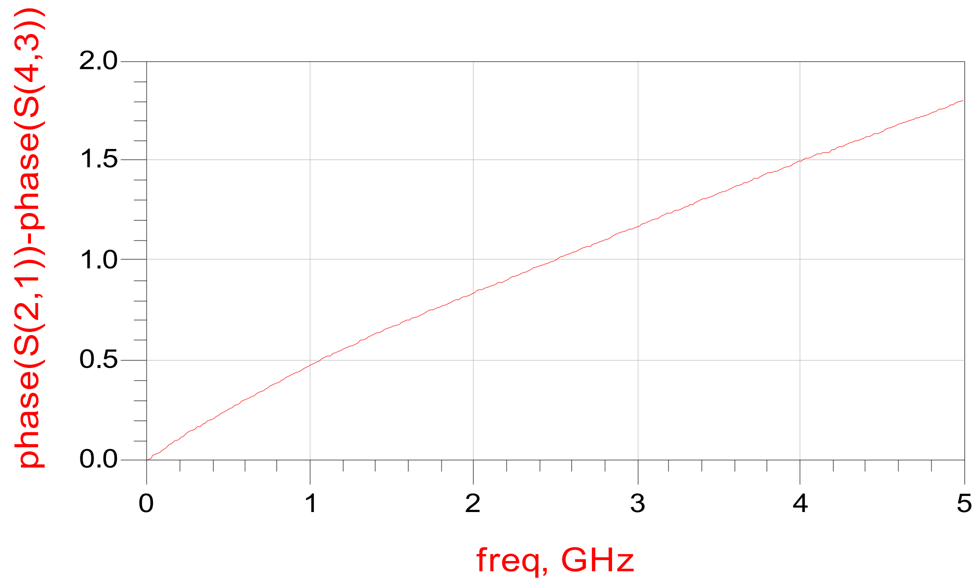

Figure 5.9 Delay line phase difference, ADS simulation.

The probed response suggested that the actual phase delay difference vary relatively linearly from approximately 0º at 10MHz to full degree greater than simulated, or approximately 2.7º, at 5GHz, as is shown in Figure 5.10. While the impact of this deviation is difficult to assess in terms of the loaded transmission lines it is concluded that this error is a comparatively small contributor to the total DA performance variance (in terms of simulated versus measured) seen.

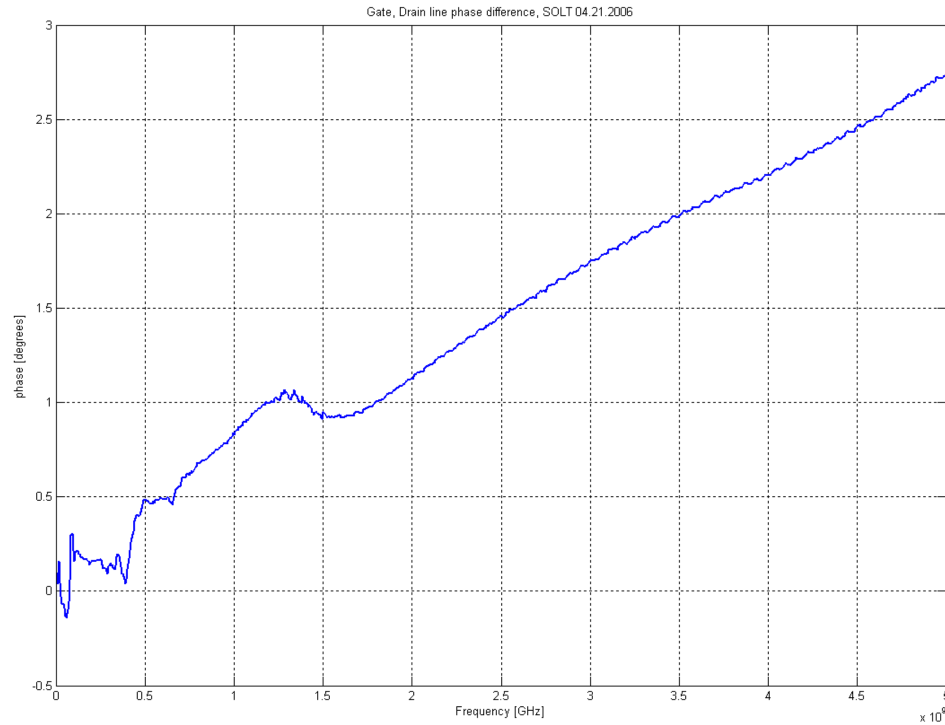

Figure 5.10 Delay line phase difference, measured data, SOLT calibration 04.21.2006.

<u>Square Planar Spiral Inductors</u>

Shown in Figure 5.11 is a micrograph of a single spiral inductor representative of those used as RF-chokes in the DA bias circuitry. Whereas the measured results obtained from the on-chip calibration standards, delay lines, and transistors (see subsequent section) were much as expected, the measured performance of the on-chip spiral inductors proved to be significantly different than expected. This is readily in seen the comparison of the simulated versus measured results of the 4.25 turn square spiral inductor shown in Figure 5.12. Below 1GHz the measured data exhibits extremely erratic behavior, very much inconsistent with the model predictions. As an initial investigation into the potential causes for the failure of the inductors to perform as

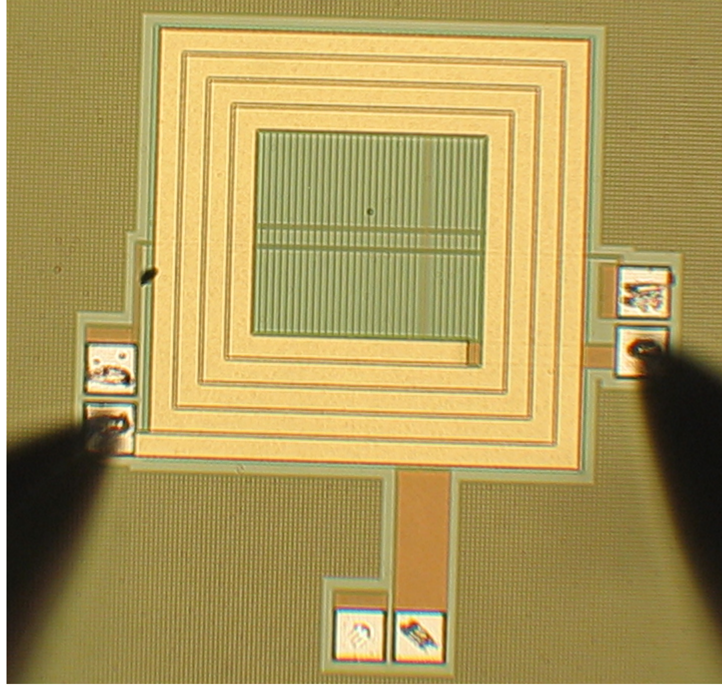

Figure 5.11 Micrograph of a 4.25 turn spiral inductor undergoing a DC connectivity test.

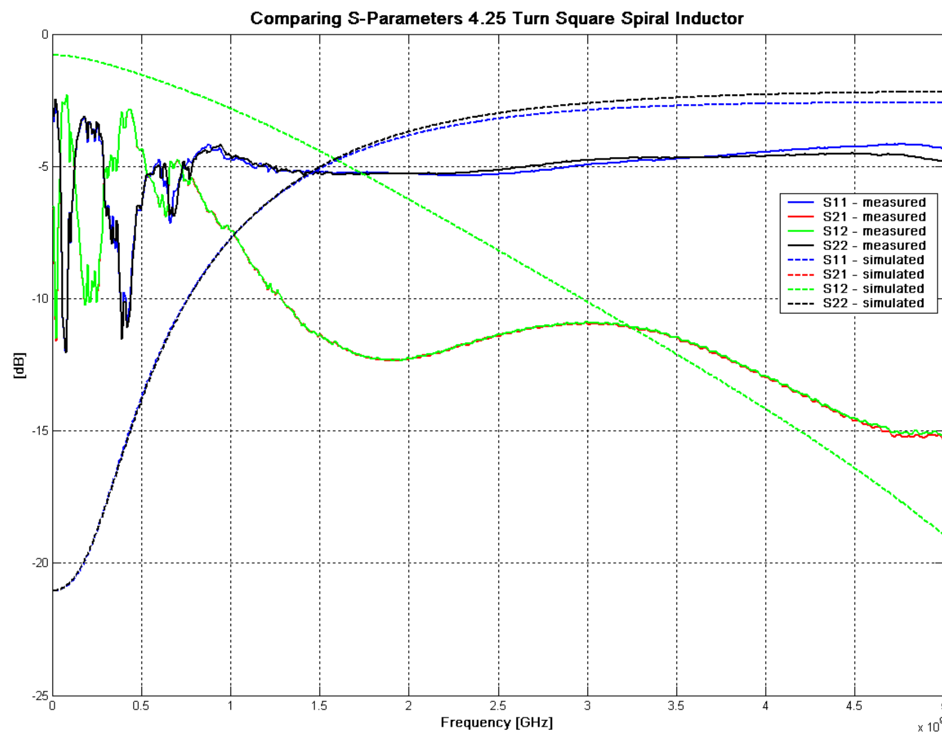

Figure 5.12 Comparing the simulated S-parameters of the 4.25 turn spiral inductor to those of the measured on-chip inductor (SOLID – measured, DASHED – simulated).

expected, DC connectivity was successfully verified (probing method shown in Figure 5.11).

A point of error in the initial 2-dimensional (2D) method-of-moment modeling of the 4.25 turn square spiral inductors was the lack of inclusion of the 17,000Å oxide/nitride passivation layer shown in Figure 3.2. Further simulation of the spiral inductor with the passivation layer modeled entirely as silicon nitride (Si_3N_4) indicated that the inclusion of the layer will in fact lower the self-resonant frequency of the inductor, but fails to explain the measured behavior below 1GHz. A comparison between the input matching and through S-parameters is shown in Figure 5.13.

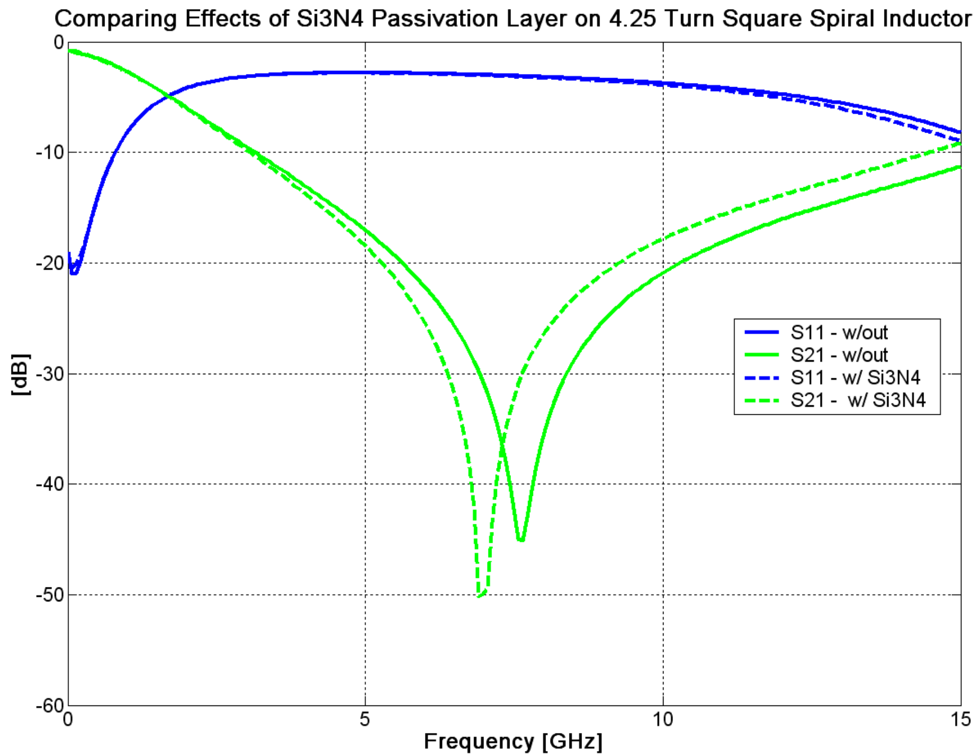

Figure 5.13 Comparing effects of including Si_3N_4 passivation layer on the simulated S-parameters of the 4.25 turn spiral inductor using IE3D (SOLID – with, DASHED – without).

The entire layer was chosen to be modeled as Si_3N_4 due to fact that the dielectric

constant of nitride is much higher (~7.5) than that of oxide (~4.0) and will therefore have the greater impact upon the performance of the inductor. Thus, the modeling was an attempt to represent a “worst-case” oxide/nitride layering.

The impact of the poor measured performance of the inductors will be discussed further when the measured results of the DA itself are examined.

Isolated Transistors

In order to characterize the transistors used within the DA individual devices equivalent to those used within the amplifier design were fabricated in the center of 500µm CPS structures as shown in Figure 5.14

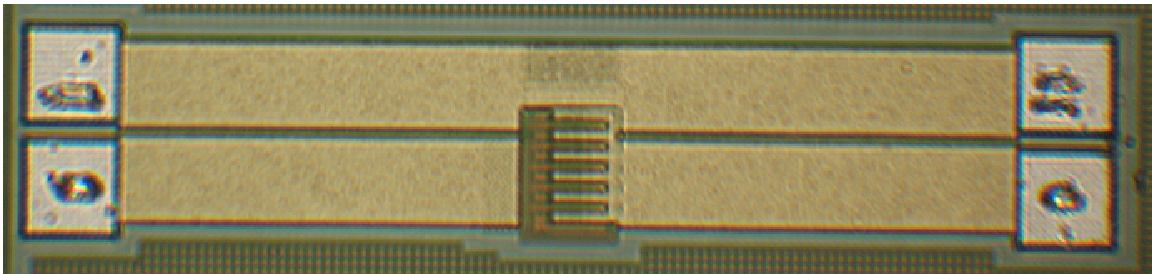

Figure 5.14 Micrograph of a 200µm by 0.6µm (WxL) transistor within a 500µm CPS structure.

The DC characteristics of the isolated transistors were measured using a B1500 semiconductor parameter analyzer manufactured by Agilent Technologies and the aforementioned probe station setup. Simulated and measured drain current (I_D) versus drain-to-source voltage (V_{DS}) curves for a single transistor are shown in Figure 5.15. The simulation results were obtained using the typical process corner at room temperature. As seen in the figure there exists good agreement between the DC results of the measured

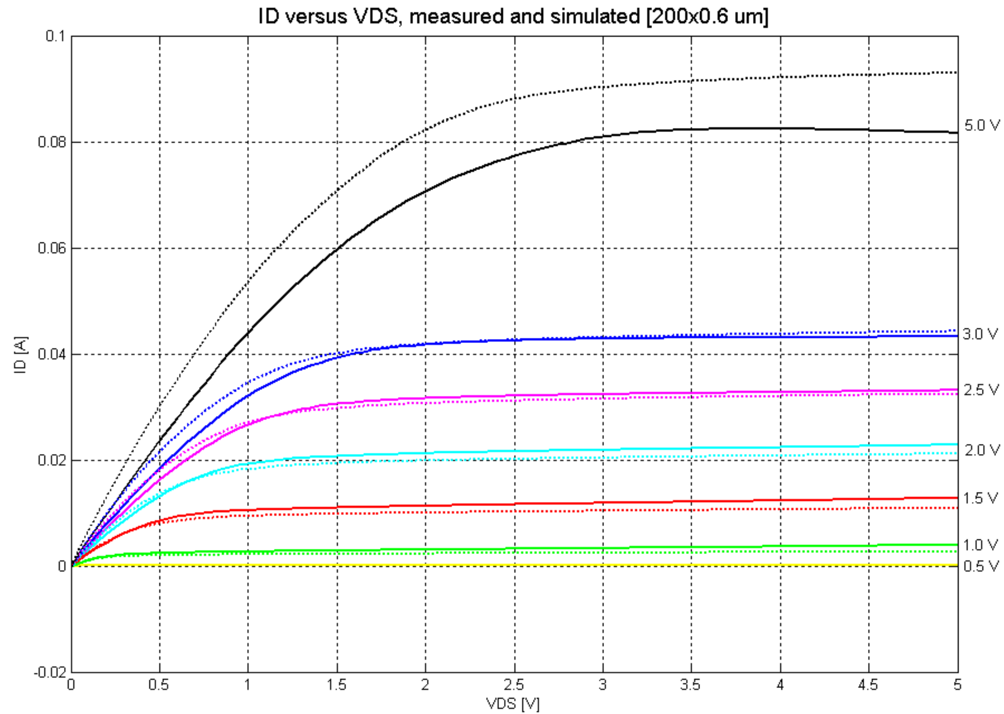

Figure 5.15 Measured (solid lines) and simulated (dashed lines) I_D versus V_{DS} curves for a single 200µm by 0.6µm (WxL) transistor.

and of the simulated transistors for gate-to-source (V_{GS}) voltages equal to 3V or less. For V_{GS} = 5V it's seen there exists a marked difference between measured and simulated results however. The transistors used within the DA were biased at V_{GS} = 3V or less. It should be noted that these simulation results were obtained using the model parameters used within the DA design process provided by AMIS. Simulation results obtained from the post-fabrication model parameters provided by MOSIS differed markedly from both the measured and the previously simulated results. This difference is readily apparent in the following figure.

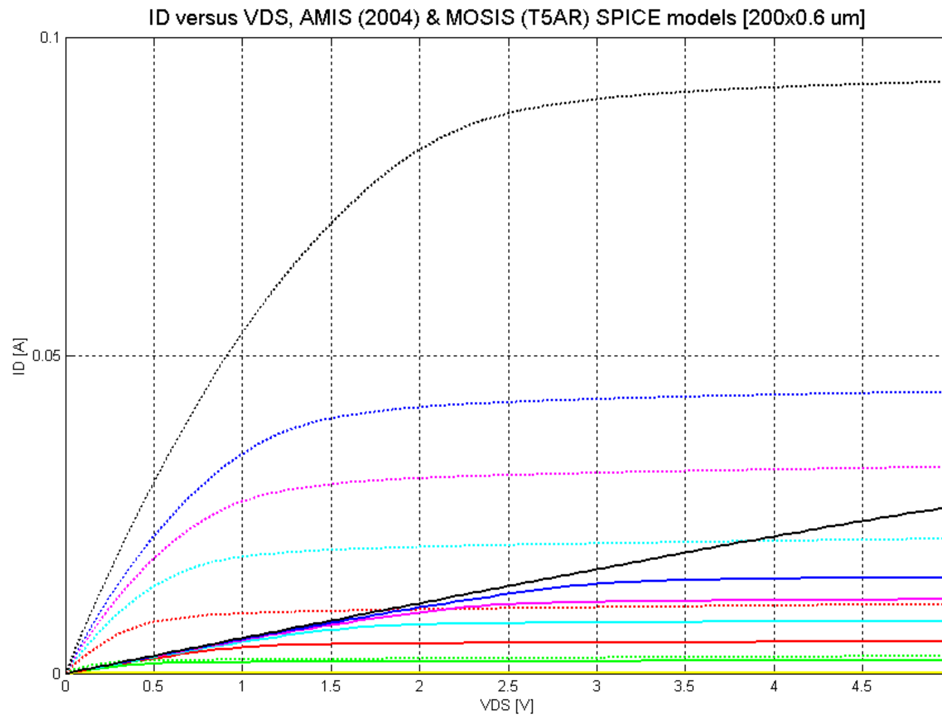

Figure 5.16 Simulated I_D versus V_{DS} curves for a single 200μm by 0.6μm (WxL) transistor using BSIM3v3 model parameters provided by AMIS (dashed) and MOSIS (solid).

In addition to the DC measurements, results were obtained for the RF performance of the individual transistors as well. Measured results can be seen compared to those obtained through simulation of a representative device in Figures 5.17 and 5.18.

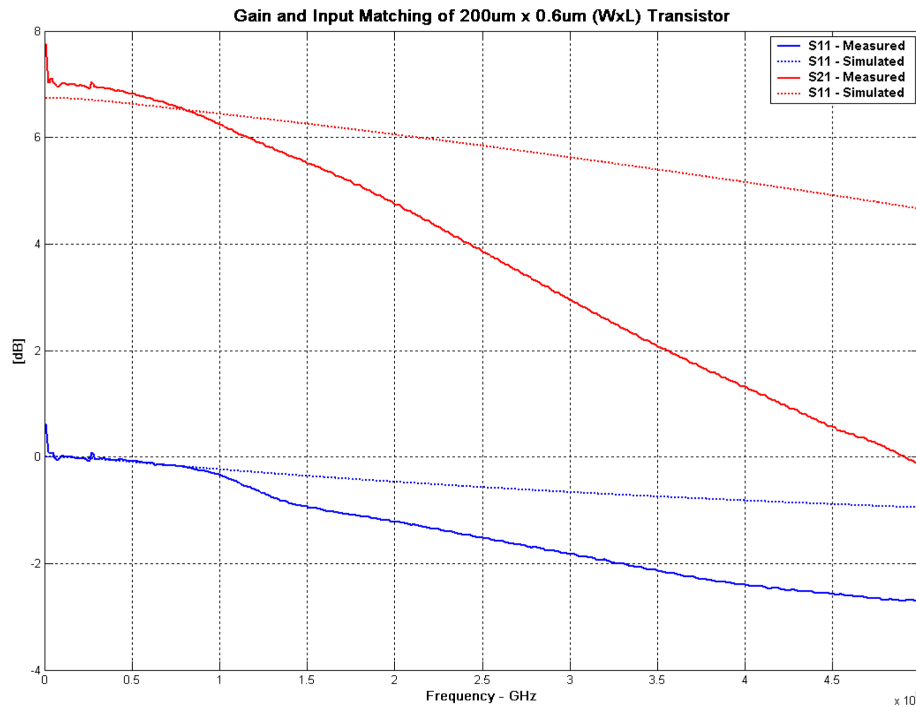

Figure 5.17 Measured (solid lines) and simulated (dashed lines) gain and input matching of a 200µm by 0.6µm (WxL) transistor.

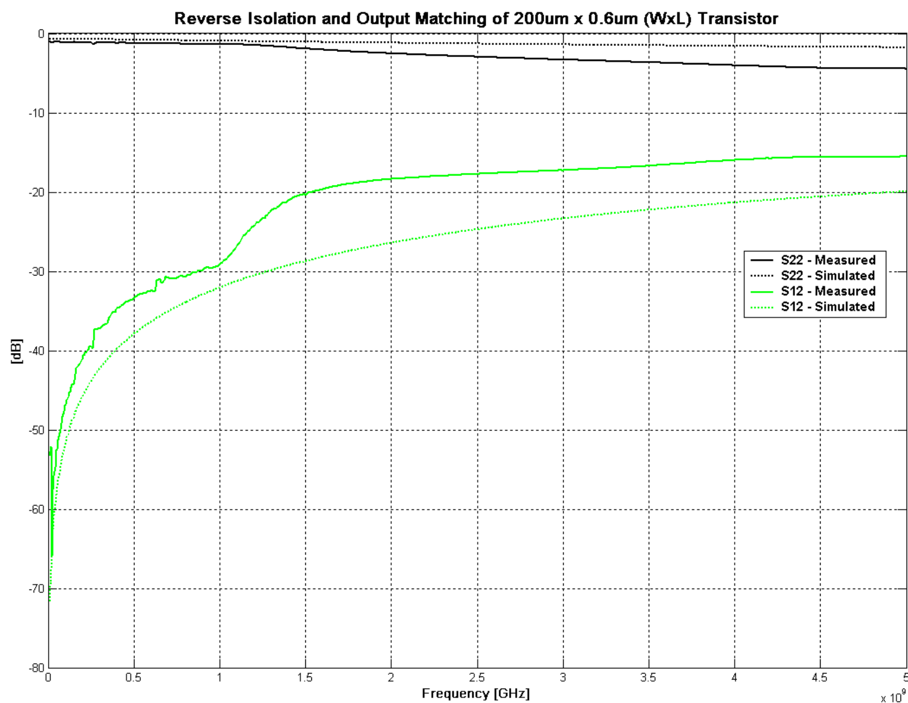

Figure 5.18 Measured (solid lines) and simulated (dashed lines) reverse isolation and output matching of a 200µm by 0.6µm (WxL) transistor.

Both sets of results shown include the effects of the input and output 50Ω CPS (250μm in length) as a SOLT calibration was performed. Recall that an SOLT calibration places the reference plane at the tips of the probes without de-embedding any of the TLs. While a TRL calibration would have allowed de-embedding of the input and output CPS, it was found that the gain of the transistors disappear at frequencies below the minimum for which the fabricated TRL standards would allow accurate calibration.

Looking at Figure 5.17, there appears to be good agreement between the measured and simulated results to approximately 1GHz. After 1GHz however, simulation predicts that the transistor should provide more than 5dB of gain past 5GHz, whereas measurements indicate that the transistor loses all gain by 5GHz in a 50Ω system. The measured input matching appears better than simulated beyond 1GHz. The fact that the transistor loses gain prematurely is a contributing, although not believed to be the primary, reason the DA exhibits the poor frequency discussed below.

Figure 5.18 shows the remaining two sets of S-parameters of the transistor, namely the reverse isolation and the output matching. This figure indicates that there is relatively good agreement between the measured and simulated results, particularly so for the reverse isolation.

In order to further discern the differences observed between the measured and simulated RF performance of the individual transistors it was next decided that inclusion of a finite gate resistance should be investigated. The layout of the individual transistors used within the DA circuit were drawn as multi-fingered devices comprised of ten fingers of width and length 200μm and 0.6μm, respectively; see Figure 5.19. The gate was contacted on both sides, giving the effect of the equivalent of twenty devices each with

width 20μm/2, connected in parallel. Thus, the gate resistance is four times smaller than what it would be if only one side of the side was connected.

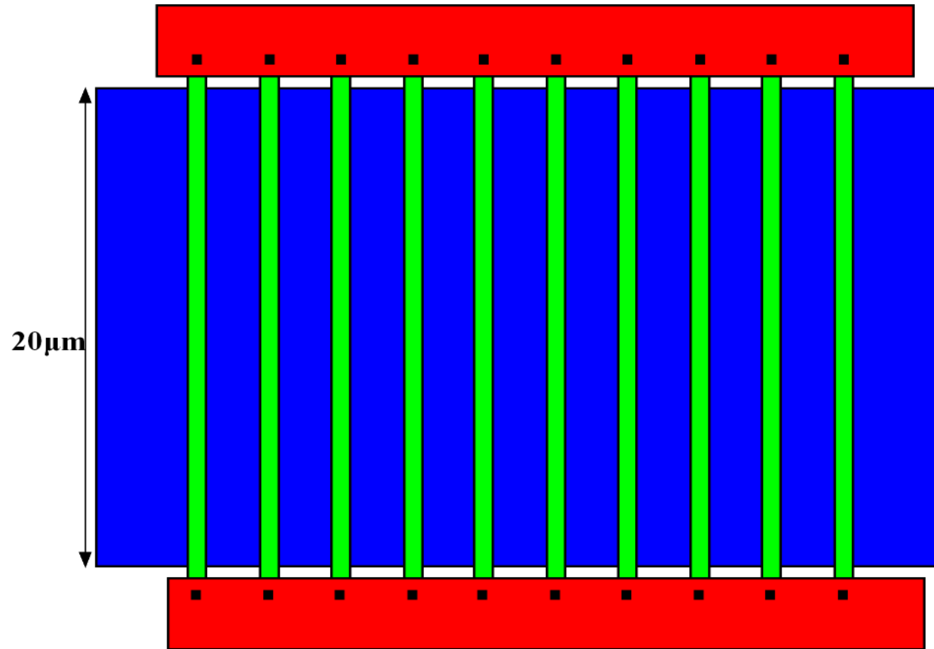

Figure 5.19 Layout representation of multi-fingered transistor of size 200/0.6μm (W/L).

From inspection of Figure 5.19 it is clear that that the gate resistance will form a distributed *RC* circuit with the gate-channel capacitance. To simulate the effects of the distributed network one may decompose the device into multiple sub-devices, obtaining a lumped approximation that becomes increasingly accurate as the number of sub-devices is increased. This however can be avoided by approximating the distributed effect of the gate resistance with a single transistor with an effective gate resistance of

$$R_{ge} = \frac{1}{12}\frac{W}{L}R_{\square}, \tag{5.5}$$

as explained by [42]. The preceding expression is the approximation for the effective

resistance of a gate connected upon both sides. To arrive at the expression for the gate connected on one end simply multiply the resistance by a factor of four. Consequently, an effective gate resistance for the transistors used within the DA circuit was calculated to be equal to ~138.9Ω using a width of 20µm, a length of 0.6µm, and a resistance per square of 50Ω. Figures 5.20 and 5.21 reflect the comparison of the measured RF performance of an isolated device to that of the simulations including an effective gate resistance. Note that the effective gate resistance significantly reduces the simulated gain and gives the appearance of improved input matching performance through resistive losses at the gate, causing a much closer agreement to the measured results than previous simulation. Thus, it is seen that inclusion of an effective gate resistance is an important RF circuit design consideration neglected in the initial DA design.

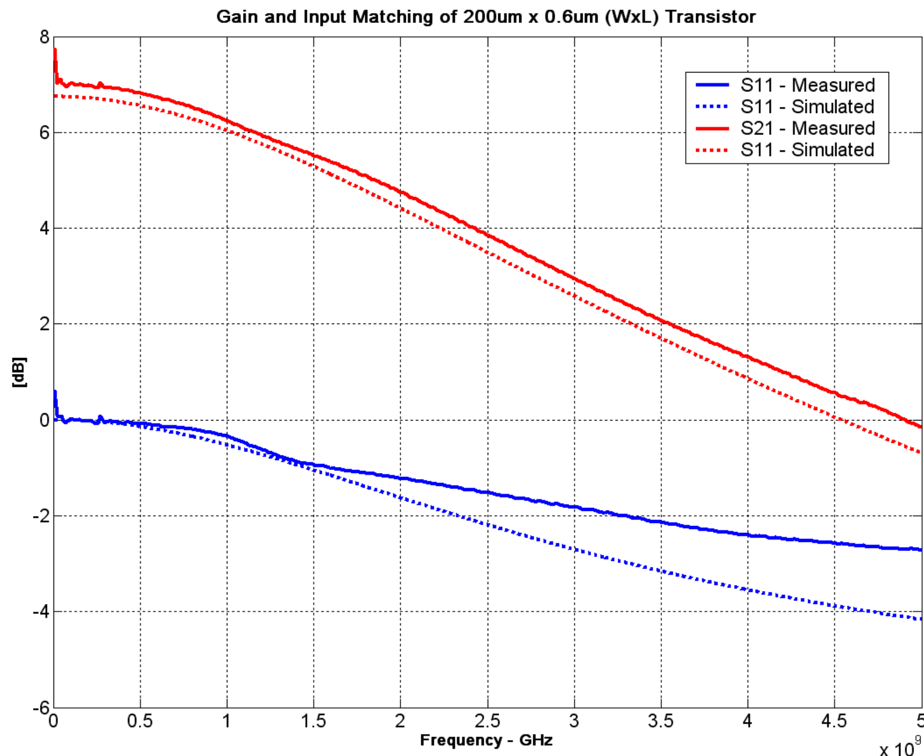

Figure 5.20 Measured (solid lines) and simulated (dashed lines) gain and input matching of a 200µm by 0.6µm (WxL) transistor including an effective gate resistance in simulation.

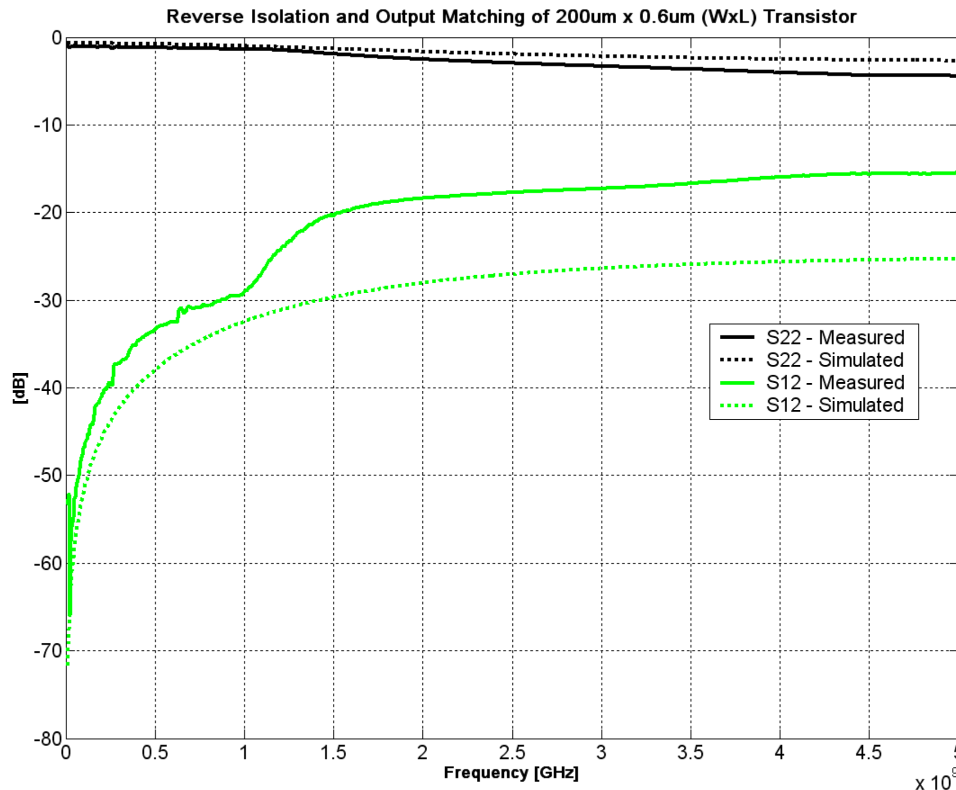

Figure 5.21 Measured (solid lines) and simulated (dashed lines) reverse isolation and output matching of a 200µm by 0.6µm (WxL) transistor including an effective gate resistance in simulation.

Distributed Amplifier

The final device to be characterized was the DA itself. The entire DA consists of six individual 200µm by 0.6µm (WxL) transistors connected by gate and drain CPS delay lines, two each square planar spiral inductors on the gate and drain line, and one 1200µm by 0.6µm (WxL) grounded-gate n-type MOSFET (GGNMOS) transistor providing electrostatic-discharge (ESD) protection at each DC bias input (2 total). The total fabricated DA can be seen in the micrograph shown in Figure 5.22.

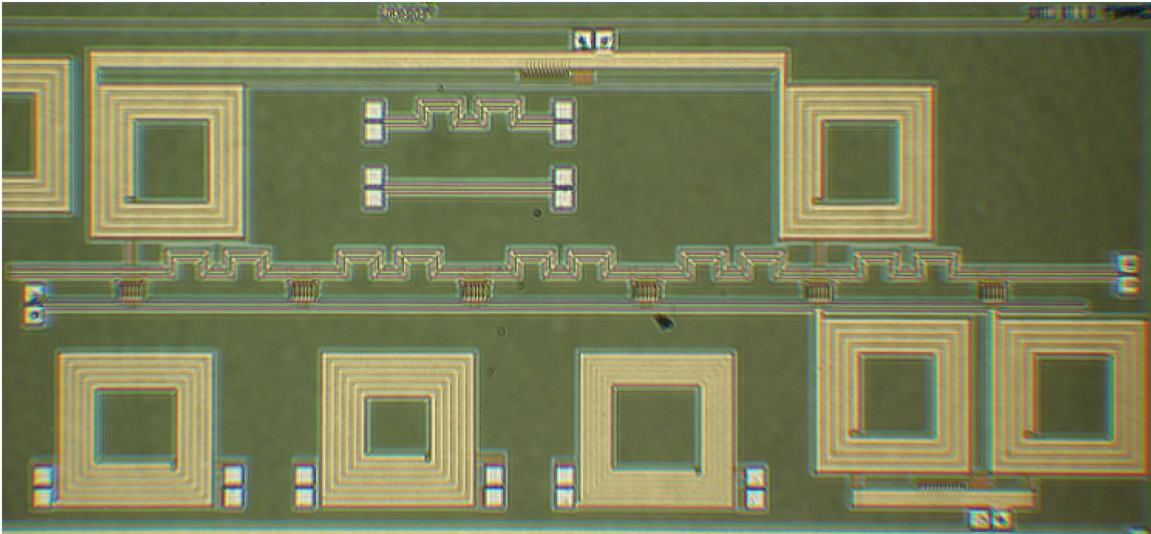

Figure 5.22 Micrograph of the fabricated distributed amplifier.

Though designed for an operating point of $V_{DS} = V_{GS} = 2.5V$, it was discovered experimentally that the DA exhibited the best performance with $V_{DS} = 3.5V$ and $V_{GS} = 1.9V$. The measured 2-port S-parameters of the DA after an SOLT calibration from 10MHz to 5GHz are shown in Figure 5.23. The DA was found to exhibit acceptable input and output matching with an input return loss (S_{11}) of better than 10dB to 10GHz and an output return loss (S_{22}) better than 8dB to 10GHz (better than 10dB for most of the range). Return isolation (S_{12}) is good, being better than 25dB to 10GHz. Finally, the 10dB of gain (S_{21}) at low frequency quickly vanishes beyond approximately 650MHz, whereas design simulation predicted that amplification would persist beyond 9GHz (see Figures 5.24 and 5.25) at these bias levels. So, while the low frequency gain exceeds prediction, the low cutoff frequency of the DA is obviously quite disappointing.

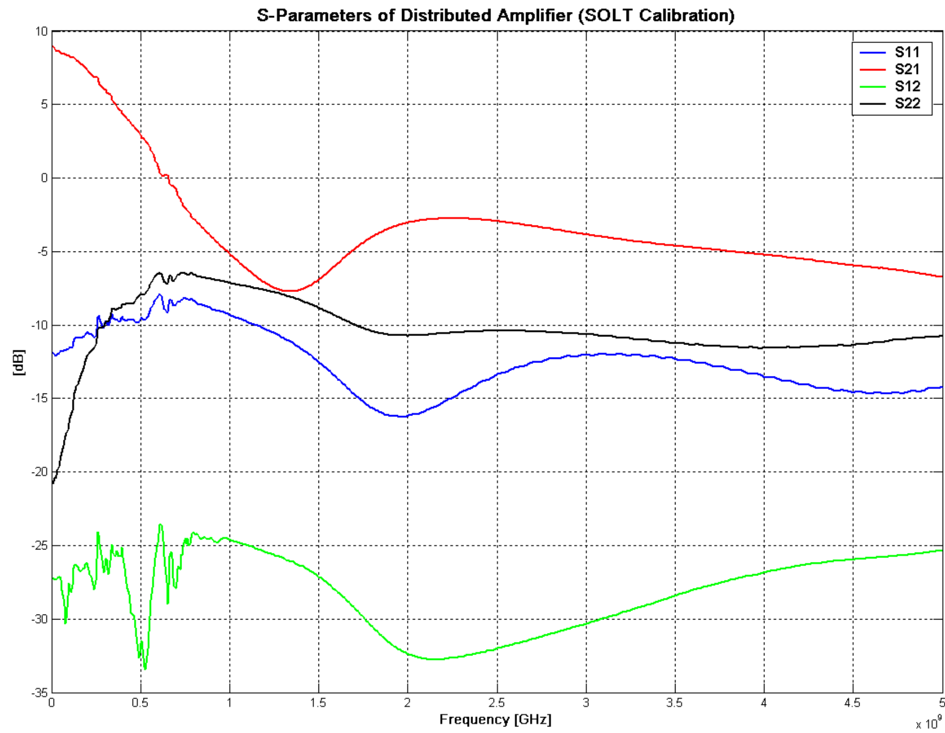

Figure 5.23 Measured 2-port S-parameters of the distributed amplifier after SOLT calibration.

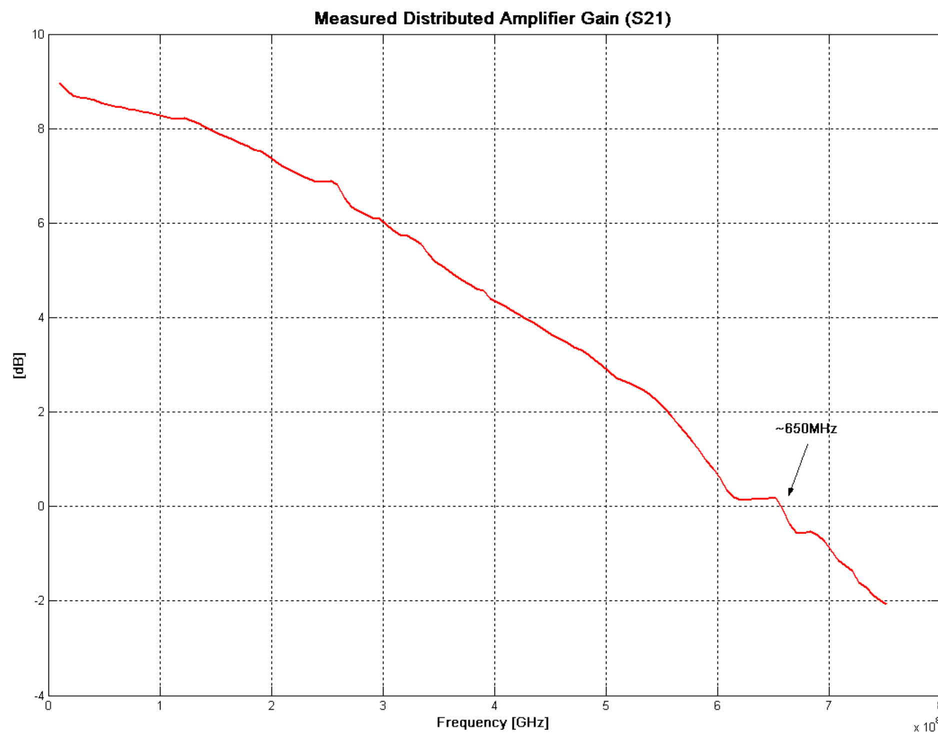

Figure 5.24 Measured gain (S_{21}) of DA with bias levels V_{DS} = 3.5V and V_{GS} = 1.9V.

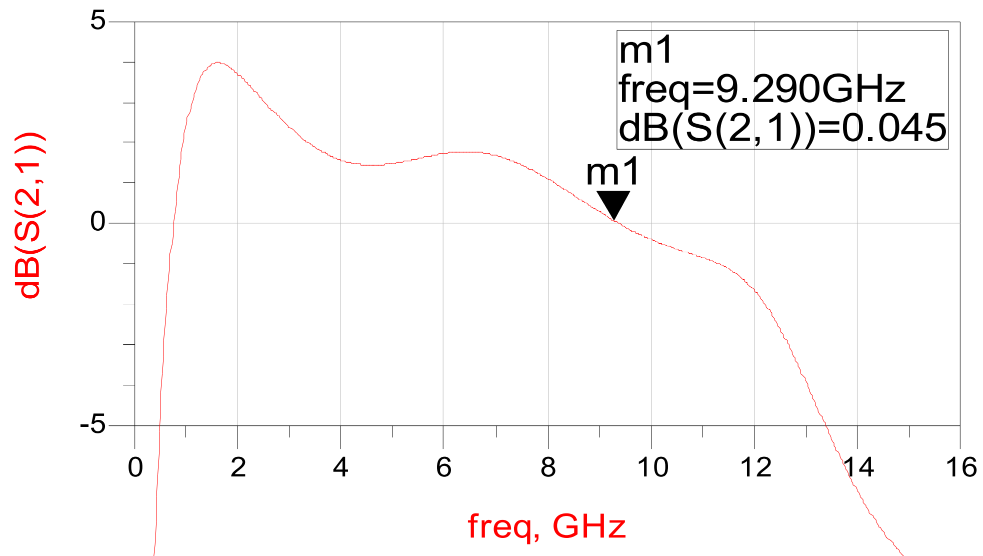

Figure 5.25 Simulated gain (S_{21}) of DA with bias levels V_{DS} = 3.5V and V_{GS} = 1.9V.

Based upon the fact that the DC and RF performance results of the isolated transistors and the phase velocity difference of the gate and drain line are reasonably close to that which was predicted (although the gain of the individual transistors exhibit a much lower cutoff frequency than initially simulated), whereas the measured behavior of the square spiral inductors differs greatly from that predicted, it is believed that the poor high-frequency gain performance of the DA may be traced in large measure to ill-performing RF-chokes.

As a first attempt to determine if in fact the on-chip inductors are the root cause of the poor performance seen the DA's measured results, the measured S-parameters of a single 4.25 turn spiral inductor were substituted for the 2D modeled inductors in the simulated DA circuit. Figure 5.26 displays the results of this simulation in terms of gain and input matching from 10MHz to 1GHz. It is readily apparent that the inductors reduce the predicted gain from beyond 7GHz (shown in Figure 5.25) to approximately 850MHz

when the measured S-parameters are utilized in the simulation. These results clearly suggest that the fabricated on-chip inductors are greatly limiting the DA's frequency response.

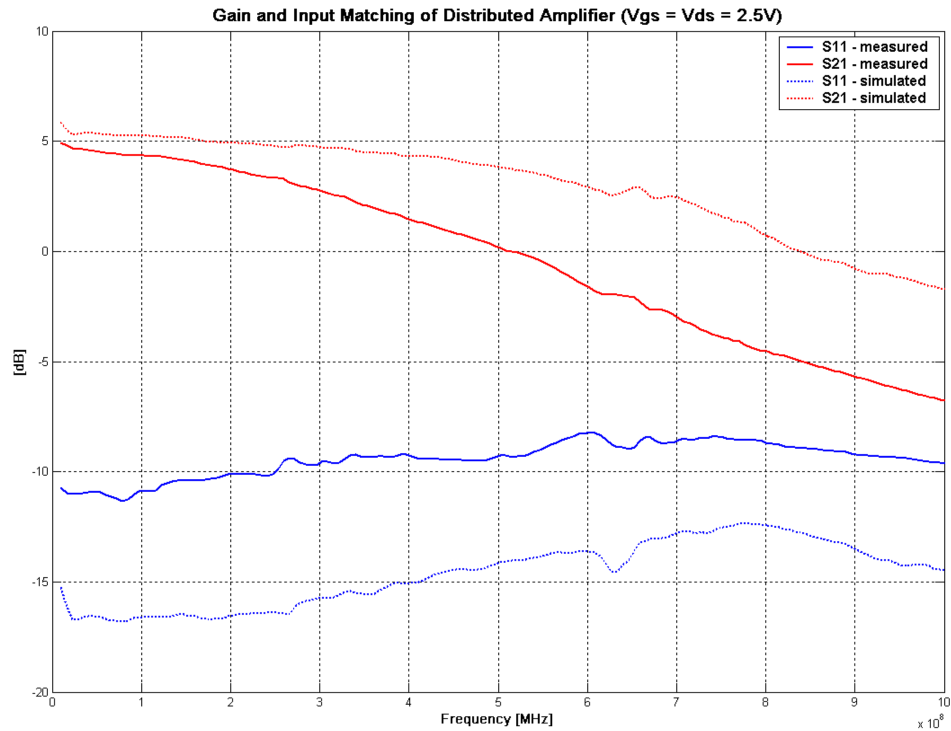

Figure 5.26 Measured (solid lines) and simulated (dashed lines) gain (S_{21}) and input matching (S_{11}) of the DA. Simulation results include *measured* data from the on-chip inductors.

CHAPTER 6
CONCLUSIONS AND RECOMMENDATIONS FOR FURTHER RESEARCH

Summary

A distributed, or traveling-wave, amplifier has been designed, fabricated, and tested using a commercial CMOS process technology. The technology used was the AMIS C5 process available through the MOSIS service. This process has a 0.6μm minimum feature size and contains three aluminum metal layers. Funding for the die fabrication was provided through a MOSIS Educational Program grant.

Both SOLT and TRL calibration techniques were utilized in the characterization of the RF performance of both passive and active devices. Measured calibration standards, both on and off chip validated the accuracy of the derived error correction models. The isolated transistors performed as predicted at DC and exhibited expected RF performance to about 1GHz, at which point the measured gain dropped more rapidly than expected in initial simulations. Further simulations of isolated transistors with an effective gate resistance show stronger agreement to measured results. The phase velocities of individual sections of the coplanar strip-lines implementing the gate and drain transmission lines were shown to agree closely with simulation. The on-chip spiral inductors were found be resonant far below the predicted 4.5GHz however. The distributed amplifier itself was shown to display gain above predicted, approximately 10dB, at low frequency and then quickly degrade to zero at about 650MHz, much below the roughly 9GHz bandwidth predicted through simulation. After importing the measured scattering parameters of the inductors into simulation, it was shown how the poor performance of the fabricated spiral inductors significantly degrades the frequency

response of the distributed amplifier to the point where the gain is predicted to drop to unity at approximately 850MHz.

Recommendations for Further Work

Planar Spiral Inductors

Fully understanding the performance of the on-chip spiral inductors would seem to be the most important task at this point in the research. This work may proceed by attempting to more accurately model the spiral inductors using a full-wave electromagnetic simulation software package such as that present in Ansoft's High Frequency Structure Simulator (HFSS). Initial 2D method-of-moments simulation appear to indicate that failing to include the passivation layer within the models during the spiral inductor design does not have a significant impact upon the inductor performance. The spurious S-parameter results obtained from on-chip inductor measurements below 1GHz appear to suggest that there exists still some unexplained effects that could be discovered through accurate 3D modeling.

Additionally, the effects of the passivation may be experimentally deduced through selective etching of the silicon nitride layer using the on-site tools available in the Montana Microfabrication Facility (MMF). The etching process must be selective to both aluminum metal and silicon dioxide making the most appropriate choice of process a dry etch one. The reactive ion etching (RIE) system present within the MMF may be used for just a procedure. Measured results after etching may then be compared to the initial design simulations and those with a silicon dioxide layer representative of that which the etching procedure did not remove. The thickness of the latter is easily

determined through using the facility's profilometer.

Planar Microwave Circuit Design Course

The forty fabricated die will also be incorporated into future offerings of the *Planar Microwave Circuit Design* course at Montana State University. The chips will allow future students to obtain hands-on laboratory experiences in on-wafer calibration and transistor characterization. A portion of the author's remaining duties will be to construct a simple, straightforward user-manual for such calibrations and measurements using the hardware (probe station, semiconductor device analyzer, VNA, etc.) and software (MultiCAL, StatistiCAL, etc.) present within Montana State's Microwave and mm-Wave Electronics Laboratory.

REFERENCES CITED

[1] IBM, "BiCMOS – Key Technology Specifications," http://www-03.ibm.com/chips/asics/foundry/technologies/bicmosspecs.html

[2] W. Hafez and M. Feng, "Experimental demonstration of pseudomorphic heterojunction bipolar transistors with cutoff frequencies above 600 GHz," *Applied Physics Letters*, vol. 86, no. 15, 152101, April 2005.

[3] W. S. Percival, "Thermionic Valve Circuits," British Patent Specification no. 460,562, filed 24 July 1936, granted January 1937.

[4] E. L. Ginzton, W. R. Hewlett, J. H. Jasberg, and J. D. Noe, "Distributed Amplification," *Proc. IRE*, pp. 956-69, August 1948.

[5] E. W. Strid and K. R. Gleason, "A DC-12 GHz Monolithic GaAsFET Distributed Amplifier," *IEEE Trans. Microwave Theory and Techniques*, vol. MTT-30, no. 7, pp. 969-975, July 1982.

[6] Y. Ayasli, R. L. Mozzi, J. L. Vorhaus, L. D. Reynolds, and R. A. Pucel, "A Monolithic GaAs 1-13-GHz Traveling-Wave Amplifier," *IEEE Trans. Microwave Theory and Techniques*, vol. MTT-30, no. 7, pp. 976-981, July 1982.

[7] K. B. Niclas, W. T. Wilser, T. R. Kritzer, and R. R. Pereira, "On Theory and Performance of Solid-State Microwave Distributed Amplifiers," *IEEE Trans. Microwave Theory and Techniques*, vol. MTT-31, no. 6, pp. 447-456, June 1983.

[8] R. Majidi-Ahy, C. K. Nishimoto, M. Riaziat, M. Glenn, S. Silverman, S.-L. Weng, Y.-C. Pao, G. A. Zdasiuk, S. G. Bandy, and Z. C. H. Tan, "5-100 GHz InP Coplanar Waveguide MMIC Distributed Amplifier," *IEEE Trans. Microwave Theory and Techniques*, vol. MTT-38, no. 12, December 1990.

[9] S. Kimura, Y. Imai, Y. Umeda, and T. Enoki, "Loss-compensated Distributed Baseband Amplifier for Optical Transmission Systems," *IEEE Trans. Microwave Theory and Techniques*, vol. MTT-44, no. 10, pp. 1688-1693, October 1996.

[10] D. Linten, S. Thijs, W. Jeamsaksiri, J. Ramos, A. Mercha, M. I. Natarajan, P. Wambacq, A. J. Scholten, and S. Decoutere, "An Integrated 5 GHz Low-Noise Amplifier with 5.5 kV HBM ESD protection in 90 nm RF CMOS," *2005 Symp. on VLSI Circuits Digest of Technical Papers*, pp. 86-89, July 16-18 2005.

[11] T. H. Lee, *Planar Microwave Engineering: A Practical Guide to Theory, Measurement, and Circuits*, Cambridge University Press, 2004.

[12] Y. Ayasli, R. L. Mozzi, J. L. Vorhaus, L. D. Reynolds, and R. A. Pucel, "A Monolithic GaAs 1-13-GHz Traveling-Wave Amplifier," *IEEE Trans. Microwave Theory and Techniques*, vol. MTT-30, pp. 976-981, July 1982.

[13] D. M. Pozar, *Microwave Engineering.* 2nd ed., New York: John Wiley & Sons, Inc., 1998.

[14] A. S. Sedra and K. C. Smith, *Microelectronic Circuits*, 4th ed., New York: Oxford University Press, Inc., 1998.

[15] Agilent Technologies Inc., "Advanced Design System (ADS) 2004A". Palo Alto, CA, Available: http://eesof.tm.agilent.com/products/ads_main.html

[16] P. H. Woerlee, M. J. Knitel, R. van Langevelde, D. B. M. Klaassen, L. F. Tiemeijer, A. J. Scholten, and A. T. A. Zegers-van Duijnhoven, "RF-CMOS Performance Trends," *IEEE Trans. On Electron Devices*, vol. 48, no. 8, pp. 1776-1782, August 2001.

[17] D. Thelen, Personal Communication, AMI Semiconductor, Inc., Bozeman, MT, June, 2006.

[18] J. P. Becker, "S-Parameter Design of Amplifiers," *EE433 – Planar Microwave Circuit Design*, Fall 2006 Lectures.

[19] C. H. Doan, S. Emami, A. M. Niknejad, and R. W. Brodersen, "Design of CMOS for 60GHz Applications," *Solid-State Circuits Conference*, vol. 1, pp. 440-538, February 2004.

[20] R. A. Pucel, "Design Considerations for Monolithic Microwave Circuits," *IEEE Trans. on Microwave Theory and Techniques*, vol. MTT-29, no. 6, pp. 513-534, June 1981.

[21] S. Akhtarzad, T. R. Rowbotham, and P. B. Johns, "The Design of Coupled Microstrip Lines," *IEEE Trans. on Microwave Theory and Techniques*, vol. MTT-23, no. 6, pp. 486-492, June 1975.

[22] R. Garg and I. J. Bahl, "Characteristics of Coupled Microstriplines," *IEEE Trans. on Microwave Theory and Techniques*, vol. MTT-27, no. 7, pp. 700-705, July 1979.

[23] M. Kirschning and R. H. Jansen, "Accurate Wide-Range Design Equations for the Frequency-Dependent Characteristic of Parallel Coupled Microstrip Lines," *IEEE Trans. on Microwave Theory and Techniques*, vol. MTT-32, no. 1, pp. 83-90, January 1984.

[24] T. Q. Deng, M. S. Leong, P. S. Kooi, and T. S. Yeo, "Synthesis formulas for coplanar lines in hybrid and monolithic MICs," *Electronics Letters*, vol. 32, no. 24, pp. 2253-2254, November 1996.

[25] C. Yildiz, "New and Very Simple Synthesis Formulas for Coplanar Strip Line," *Microwave and Optical Technology Letters*, vol. 44, no. 2, pp. 199-202, January 2005.

[26] Zeland Software Inc., "IE3D Version 8.2", Fremont, CA, Available: http://www.zeland.com

[27] B. Kleveland, C. H. Diaz, D. Vook, L. Madden, T. H. Lee, and S. S. Wong, "Monolithic CMOS Distributed Amplifier and Oscillator," in *IEEE Dig. Tech. Papers*, 1999, pp. 70-71.

[28] P. J. Sullivan, B. A. Xavier, and W. H. Ku, "An Integrated CMOS Distributed Amplifier Utilizing Packaging Inductance," *IEEE Trans. on Microwave Theory and Techniques*, vol. 45, no. 10, October 1997, pp. 1969-1976.

[29] B. M. Ballweber, R. Gupta, and D. J. Allstot, "A Fully Integrated 0.5-5.5-GHz CMOS Distributed Amplifer," *IEEE Trans. on Solid-State Circuits*, vol. 35, no. 2, pp. 231-238, February 2000.

[30] L. N. Alves and R. L. Aguiar, "Frequency Behavior of Classical Current Mirrors," *ICECS 2002 - 9th IEEE Conference on Electronics, Circuits and Systems*, Dubrovnik, Croatia, Sep. 2002.

[31] S. S. Mohan, M. Hershenson, S. P. Boyd, and T. H. Lee, "Simple Accurate Expressions for Planar Spiral Inductors", *IEEE Journal of Solid-State Circuits*, vol. 43, no. 10, pp. 1419-1424, October 1999.

[32] A. Zolfaghari, A. Chan, and B. Razavi, "Stacked Inductors and Transformers in CMOS Technology," *IEEE Journal of Solid-State Circuits*, vol. 36, no. 4, pp.620-628, April 2001.

[33] T. Dickson, M.-A. LaCroix, S. Boret, D. Gloria, R. Beerkens, and S. P. Voinigescu, "Si-based Inductors and Transformers for 30-100 GHz Applications," *Microwave Symposium Digest, 2004 IEEE MTT-S International*, vol. 1, pp. 205-208, June, 2004.

[34] Ansoft Corporation, "High Frequency Structure Simulator (HFSS) Ver. 9.2.1", Tech. Rep., Pittsburgh, PA, 2005. Available: http://www.ansoft.com/products/hf/hfss/

[35] T. H. Lee, *The Design of CMOS Radio-Frequency Integrated Circuits*, 2nd ed., Cambridge University Press, 2004.

[36] Cadence Design Systems, "Virtuoso Layout Editor," San Jose, CA, Available: http://www.cadence.com/

[37] *Agilent Network Analyzer Basics*, Agilent Technologies, Inc., August 31, 2004.

[38] S. A. Wartenberg, *RF Measurements of Die and Packages*, Artech House, Inc.,

2002.

[39] G. F. Engen and C. A. Hoer, "'Thru-Reflect-Line': An Improved Technique for Calibrating the Dual Six-Port Automatic Network Analyzer," vol. MTT-27, no. 12, pp. 987-993, December 1979.

[40] D. F. Williams, J. C. M. Wang, and U. Arz, "An Optimal Vector-Network Analyzer Calibration Algorithm," *IEEE Trans. on Microwave Theory and Techniques*, vol. MTT-51, no. 12, pp. 2391-2401, December 2003.

[41] P. T. Boggs, R. H. Byrd, J. E. Rogers, and R. B. Schnabel, "User's Reference Guide for ODRPACK Version 2.01 Software for Wieghted Orthogonal Distance Regression," NIST, Boulder, CO, Internal Rep. NISTIR 91-4834, June 1992.

[42] Y. Tsividis, *Operation and Modeling of The MOS Transistor*, 2nd Ed., Oxford, New York, Oxford University Press, 1999.

APPENDICES

APPENDIX A

NON-QUASISTATIC EFFECTS

Non-quasistatic Effects & CMOS SPICE Models

The majority of MOSFET models implemented in SPICE are based upon quasistatic (QS) approximations. QS operation assumes that the terminal voltages vary slowly enough for the channel charge of the MOS transistor to achieve equilibrium instantaneously [1]. Thus, these charges can be determined using equivalent DC voltages applied to the terminals. At high-frequencies however, these approximations begin to breakdown, leading to unpredictable transistor behavior. Attempts to quantify criteria for the onset of non-quasistatic (NQS) effects based upon transient behavioral simulations have been proposed by [2] and [3]. These simulation results suggest that the total inversion charge, given by

$$Q_{inv}(t) = \int_0^L Q'_{inv}(t)dx = Q_{inv,DC} + \hat{Q}_{inv'} \sin(\omega t + \phi) \tag{A.1}$$

when stimulated by a sinusoidal input voltage, deviates from that predicted by the QS model in both amplitude and phase at sufficiently high frequency. Results presented by [2] demonstrate that the amplitude remains nearly constant until a certain frequency limit, while the phase shift varies linearly with phase. Using these results, the non-quasistatic onset frequency limit f_{NQS} can be defined separately in terms of acceptable inversion layer amplitude and phase deviation from that of the QS model. The former was found to be minimal until nearly the unity-gain frequency f_T of the devices simulated in both [2] and [3]. Phase deviation was indicated to range from ~3º at 20% of f_T to ~12º at f_T.

Typical analog circuits may be designed with a respectable phase margin in order

to ensure stable operation, mitigating the requirement of using NQS device modeling. This phase deviation can create much more significant performance degradation in a DA design however. Recall that phase velocity equalization is a principle requirement in the DA. Phase differences of greater than 5º were experimentally shown by the author to result in significant signal reflections. Using the device parameters indicated in this thesis, these results indicate that the QS BSIM3v3 model used should only be taken to accurately simulate the response of the DA up to approximately 5GHz.

[1] Y. Tsividis, *Operation and Modeling of the MOS Transistor*, 2nd Ed., Oxford University Press, U.S.A., 2003.

[2] E. Gondro, O. Kowarik, G. Knoblinger, and P. Klein, "When do we need Non-Quasistatic CMOS RF-Models?," *Proc. IEEE Custom Integrated Circuits Conf.*, San Diego, CA, May 2001, pp. 377-380.

[3] A. F.-L. Ng, P. K. Ko, and M. Chan, "Determining the Onset Frequency of Nonquasistatic Effects of the MOSFET in AC Simulation," *IEEE Electron Device Letters*, vol. 23, no. 1, January 2002, pp. 37-39.

APPENDIX B

AMIS C5 BSIM3V3 SPICE MODEL PARAMETERS (CONFIDENTIAL)

APPENDIX C

MOSIS T5AR RUN
WAFER ELECTRICAL TEST DATA AND SPICE MODEL PARAMETERS

MOSIS WAFER ACCEPTANCE TESTS

RUN: T5AR VENDOR: AMIS
TECHNOLOGY: SCN05 FEATURE SIZE: 0.5 microns
Run type: SKD

INTRODUCTION: This report contains the lot average results obtained by MOSIS from measurements of MOSIS test structures on each wafer of this fabrication lot. SPICE parameters obtained from similar measurements on a selected wafer are also attached.

COMMENTS: American Microsystems, Inc. C5

TRANSISTOR PARAMETERS	W/L	N-CHANNEL	P-CHANNEL	UNITS
MINIMUM	3.0/0.6			
Vth		0.74	-0.94	volts
SHORT	20.0/0.6			
Idss		459	-242	uA/um
Vth		0.64	-0.91	volts
Vpt		10.0	-10.0	volts
WIDE	20.0/0.6			
Ids0		< 2.5	< 2.5	pA/um
LARGE	50/50			
Vth		0.65	-0.96	volts
Vjbkd		11.0	-11.7	volts
Ijlk		<50.0	<50.0	pA
Gamma		0.49	0.57	V^0.5
K' (Uo*Cox/2)		54.6	-18.8	uA/V^2
Low-field Mobility		445.90	153.53	cm^2/V*s

COMMENTS: Poly bias varies with design technology. To account for mask bias use the appropriate value for the parameter XL in your SPICE model card.

Design Technology	XL (um)	XW (um)
SCMOS_SUBM (lambda=0.30)	0.10	0.00
SCMOS (lambda=0.35)	0.00	0.20

FOX TRANSISTORS	GATE	N+ACTIVE	P+ACTIVE	UNITS
Vth	Poly	>15.0	<-15.0	volts

PROCESS PARAMETERS	N+	P+	POLY	PLY2_HR	POLY2	M1	M2	UNITS
Sheet Resistance	82.0	102.6	23.3	1101	41.9	0.09	0.09	ohms/sq
Contact Resistance	60.9	146.9	17.1		27.7		0.83	ohms
Gate Oxide Thickness	141							angstrom

PROCESS PARAMETERS	M3	N\PLY	N_W	UNITS
Sheet Resistance	0.05	847	841	ohms/sq
Contact Resistance	0.79			ohms

COMMENTS: N\POLY is N-well under polysilicon.

CAPACITANCE PARAMETERS	N+	P+	POLY	POLY2	M1	M2	M3	N_W	UNITS
Area (substrate)	432	728	85		32	16	10	40	aF/um^2
Area (N+active)			2447		36	16	11		aF/um^2
Area (P+active)			2340						aF/um^2
Area (poly)				911	56	16	9		aF/um^2
Area (poly2)					49				aF/um^2
Area (metal1)						31	13		aF/um^2
Area (metal2)							33		aF/um^2
Fringe (substrate)	351	289			74	58	38		aF/um
Fringe (poly)					57	38	28		aF/um
Fringe (metal1)						54	33		aF/um
Fringe (metal2)							51		aF/um
Overlap (N+active)			214						aF/um
Overlap (P+active)			231						aF/um

CIRCUIT PARAMETERS			UNITS
Inverters	K		
Vinv	1.0	1.97	volts
Vinv	1.5	2.23	volts
Vol (100 uA)	2.0	0.12	volts
Voh (100 uA)	2.0	4.86	volts
Vinv	2.0	2.41	volts
Gain	2.0	-18.60	

```
 Ring Oscillator Freq.
  DIV256 (31-stg,5.0V)                100.83  MHz
  D256_WIDE (31-stg,5.0V)             152.64  MHz
 Ring Oscillator Power
  DIV256 (31-stg,5.0V)                  0.50  uW/MHz/gate
  D256_WIDE (31-stg,5.0V)               1.01  uW/MHz/gate
```

COMMENTS: SUBMICRON

T5AR SPICE BSIM3 VERSION 3.1 PARAMETERS

SPICE 3f5 Level 8, Star-HSPICE Level 49, UTMOST Level 8

```
* DATE: Dec 19/05
* LOT: T5AR                  WAF: 9102
* Temperature_parameters=Default
.MODEL CMOSN NMOS (                                LEVEL   = 49
+VERSION = 3.1            TNOM    = 27             TOX     = 1.41E-8
+XJ      = 1.5E-7         NCH     = 1.7E17         VTH0    = 0.586875
+K1      = 0.8563109      K2      = -0.0870606     K3      = 21.2216405
+K3B     = -8.2868264     W0      = 1E-8           NLX     = 1E-9
+DVT0W   = 0              DVT1W   = 0              DVT2W   = 0
+DVT0    = 2.6056345      DVT1    = 0.4382785      DVT2    = -0.1735756
+U0      = 456.0277023    UA      = 2.415709E-12   UB      = 1.416873E-
18
+UC      = 4.598182E-12   VSAT    = 1.92885E5      A0      = 0.5967346
+AGS     = 0.1129858      B0      = 2.667003E-6    B1      = 5E-6
+KETA    = -9.709638E-4   A1      = 1.170959E-5    A2      = 0.3031839
+RDSW    = 1.264411E3     PRWG    = 0.0767006      PRWB    = 0.0181561
+WR      = 1              WINT    = 1.950485E-7    LINT    = 7.18413E-8
+XL      = 1E-7           XW      = 0              DWG     =
-4.687723E-9
+DWB     = 5.083626E-8    VOFF    = 0              NFACTOR = 0.3386768
+CIT     = 0              CDSC    = 2.4E-4         CDSCD   = 0
+CDSCB   = 0              ETA0    = 2.048127E-3    ETAB    =
-1.791953E-4
+DSUB    = 0.0684107      PCLM    = 2.546561       PDIBLC1 = 1
+PDIBLC2 = 2.474758E-3    PDIBLCB = -0.0168243     DROUT   = 0.9735435
+PSCBE1  = 6.377329E8     PSCBE2  = 2.095166E-4    PVAG    = 9.989289E-3
+DELTA   = 0.01           RSH     = 82             MOBMOD  = 1
+PRT     = 0              UTE     = -1.5           KT1     = -0.11
+KT1L    = 0              KT2     = 0.022          UA1     = 4.31E-9
+UB1     = -7.61E-18      UC1     = -5.6E-11       AT      = 3.3E4
+WL      = 0              WLN     = 1              WW      = 0
+WWN     = 1              WWL     = 0              LL      = 0
+LLN     = 1              LW      = 0              LWN     = 1
+LWL     = 0              CAPMOD  = 2              XPART   = 0.5
+CGDO    = 2.14E-10       CGSO    = 2.14E-10       CGBO    = 1E-9
+CJ      = 4.309065E-4    PB      = 0.97442      MJ      = 0.4323804
+CJSW    = 3.255079E-10   PBSW    = 0.8            MJSW    = 0.2023408
+CJSWG   = 1.64E-10       PBSWG   = 0.8            MJSWG   = 0.2023408
+CF      = 0              PVTH0   = 0.1279055      PRDSW   =
-183.5626587
+PK2     = -0.0273762     WKETA   = -0.018498      LKETA   = 3.588525E-
```

```
3      )
*
.MODEL CMOSP PMOS (                               LEVEL   = 49
+VERSION = 3.1            TNOM    = 27            TOX     = 1.41E-8
+XJ      = 1.5E-7         NCH     = 1.7E17        VTH0    = -0.9239325
+K1      = 0.5474696      K2      = 7.884255E-3   K3      = 5.7895228
+K3B     = -1.0529775     W0      = 2.392135E-7   NLX     = 9.013808E-8
+DVT0W   = 0              DVT1W   = 0             DVT2W   = 0
+DVT0    = 2.4409049      DVT1    = 0.479078      DVT2    = -0.0812137
+U0      = 202.7748917    UA      = 2.492512E-9   UB      = 1E-21
+UC      = -7.05979E-11   VSAT    = 1.518724E5    A0      = 0.7338304
+AGS     = 0.095815       B0      = 1.07472E-6    B1      = 4.99995E-6
+KETA    = -8.151786E-4   A1      = 7.117004E-4   A2      = 0.3261133
+RDSW    = 3E3            PRWG    = -0.0422194    PRWB    = -0.0192246
+WR      = 1              WINT    = 2.300175E-7   LINT    = 9.660331E-8
+XL      = 1E-7           XW      = 0             DWG     =
-8.177807E-9
+DWB     = 1.723601E-8    VOFF    = -0.0604473    NFACTOR = 0.735806
+CIT     = 0              CDSC    = 2.4E-4        CDSCD   = 0
+CDSCB   = 0              ETA0    = 0.4947532     ETAB    = -0.0743284
+DSUB    = 1              PCLM    = 2.3713952     PDIBLC1 = 0.0317803
+PDIBLC2 = 3.060557E-3    PDIBLCB = -0.0531146    DROUT   = 0.1834052
+PSCBE1  = 5.297294E9     PSCBE2  = 5E-10         PVAG    = 0.0132388
+DELTA   = 0.01           RSH     = 102.6         MOBMOD  = 1
+PRT     = 0              UTE     = -1.5          KT1     = -0.11
+KT1L    = 0              KT2     = 0.022         UA1     = 4.31E-9
+UB1     = -7.61E-18      UC1     = -5.6E-11      AT      = 3.3E4
+WL      = 0              WLN     = 1             WW      = 0
+WWN     = 1              WWL     = 0             LL      = 0
+LLN     = 1              LW      = 0             LWN     = 1
+LWL     = 0              CAPMOD  = 2             XPART   = 0.5
+CGDO    = 2.31E-10       CGSO    = 2.31E-10      CGBO    = 1E-9
+CJ      = 7.256029E-4    PB      = 0.9506215     MJ      = 0.4987322
+CJSW    = 2.85532E-10    PBSW    = 0.99          MJSW    = 0.2661054
+CJSWG   = 6.4E-11        PBSWG   = 0.99          MJSWG   = 0.2661054
+CF      = 0              PVTH0   = 5.98016E-3    PRDSW   = 14.8598424
+PK2     = 3.73981E-3     WKETA   = 5.300715E-3   LKETA   =
-5.899284E-3    )
*
```

APPENDIX D

IE3D EXTRACTED RLGC PARAMETERS FOR 500mm, 50Ω CPS

The frequency dependent equivalent circuit parameters:

Warning: The error function for 11 GHz and higher frequency is quite high (0.253373>0.25).
The single RLC-equivalent circuit may not be a suitable one for it. Please check
its accuracy before use the data.

Freq (GHz)	Error Factor	Q-Factor	Series R (Ohms)	Series L (nH)	Shunt R (Ohms)	Shunt C (pF)
0.25	0.0095961	0.54493	0.84954	0.29484	90003	0.12661
0.5	0.018877	1.0209	0.88947	0.28928	23031	0.12482
0.75	0.027704	1.4212	0.93968	0.28381	10685	0.12175
1	**0.03601**	**1.7565**	**0.99382**	**0.27849**	**6371.6**	**0.11788**
1.25	0.043789	2.0437	1.0476	0.27357	4373.3	0.11352
1.5	0.051075	2.2973	1.0985	0.26917	3285.9	0.10895
1.75	0.05792	2.5277	1.146	0.26532	2628.7	0.10437
2	0.064386	2.741	1.1899	0.26198	2201.2	0.099957
2.25	0.070534	2.9409	1.2306	0.25906	1907.3	0.095792
2.5	0.07642	3.1297	1.2686	0.25649	1696.5	0.091935
2.75	0.082094	3.3088	1.3041	0.25421	1540	0.088409
3	0.087599	3.4795	1.3376	0.25215	1420.6	0.085214
3.25	0.092972	3.6427	1.369	0.25028	1327.2	0.082336
3.5	0.098243	3.7995	1.3986	0.24857	1252.8	0.079753
3.75	0.10344	3.9507	1.4263	0.24699	1192.4	0.07744
4	0.10857	4.0971	1.4523	0.24552	1142.7	0.075371
4.25	0.11367	4.2394	1.4765	0.24414	1101.1	0.073518
4.5	0.11873	4.3781	1.4991	0.24284	1066.1	0.07186
4.75	0.12378	4.5137	1.5199	0.24162	1036.1	0.070372
5	0.12881	4.6468	1.5392	0.24047	1010.3	0.069036
5.25	0.13384	4.7776	1.5569	0.23938	987.85	0.067835
5.5	0.13888	4.9064	1.573	0.23833	968.17	0.066752
5.75	0.14391	5.0335	1.5876	0.23734	950.8	0.065774
6	0.14896	5.1591	1.6008	0.23639	935.36	0.06489
6.25	0.15401	5.2833	1.6127	0.23547	921.55	0.064089
6.5	0.15908	5.4062	1.6232	0.2346	909.12	0.063362
6.75	0.16416	5.5281	1.6324	0.23375	897.88	0.0627
7	0.16926	5.6489	1.6403	0.23293	887.66	0.062098
7.25	0.17437	5.7687	1.647	0.23214	878.33	0.061549
7.5	0.1795	5.8877	1.6526	0.23137	869.76	0.061047
7.75	0.18465	6.0058	1.6571	0.23063	861.86	0.060589
8	0.18982	6.1231	1.6604	0.2299	854.54	0.060169
8.25	0.195	6.2396	1.6628	0.22919	847.74	0.059785
8.5	0.20021	6.3554	1.6641	0.22849	841.39	0.059432
8.75	0.20543	6.4705	1.6644	0.22781	835.44	0.059109
9	0.21067	6.5849	1.6638	0.22714	829.85	0.058812
9.25	0.21594	6.6985	1.6622	0.22649	824.57	0.05854
9.5	0.22122	6.8115	1.6597	0.22584	819.57	0.058289
9.75	0.22653	6.9238	1.6564	0.2252	814.81	0.05806
10	0.23185	7.0355	1.6522	0.22457	810.27	0.057849
10.25	0.2372	7.1464	1.6472	0.22395	805.93	0.057656
10.5	0.24257	7.2567	1.6414	0.22333	801.76	0.057479
10.75	0.24796	7.3664	1.6348	0.22272	797.74	0.057316
11	0.25337	7.4753	1.6275	0.22212	793.85	0.057168
11.25	0.25881	7.5835	1.6194	0.22151	790.08	0.057033
11.5	0.26427	7.6911	1.6105	0.22092	786.42	0.056909
11.75	0.26975	7.798	1.601	0.22032	782.84	0.056797
12	0.27525	7.9041	1.5908	0.21973	779.34	0.056696
12.25	0.28078	8.0095	1.5799	0.21913	775.91	0.056604
12.5	0.28633	8.1142	1.5683	0.21854	772.53	0.056522
12.75	0.2919	8.2181	1.5561	0.21796	769.19	0.056449
13	0.2975	8.3212	1.5432	0.21737	765.9	0.056383
13.25	0.30312	8.4235	1.5297	0.21678	762.63	0.056326
13.5	0.30877	8.525	1.5156	0.21619	759.38	0.056276
13.75	0.31445	8.6257	1.5009	0.2156	756.14	0.056233
14	0.32015	8.7255	1.4857	0.21501	752.91	0.056196
14.25	0.32587	8.8244	1.4698	0.21442	749.69	0.056166
14.5	0.33163	8.9224	1.4534	0.21383	746.45	0.056142
14.75	0.33741	9.0194	1.4364	0.21324	743.21	0.056124
15	0.34321	9.1155	1.4189	0.21264	739.95	0.056111

APPENDIX E

ANALYTICAL PLANAR SPIRAL INDUCTOR DESIGN

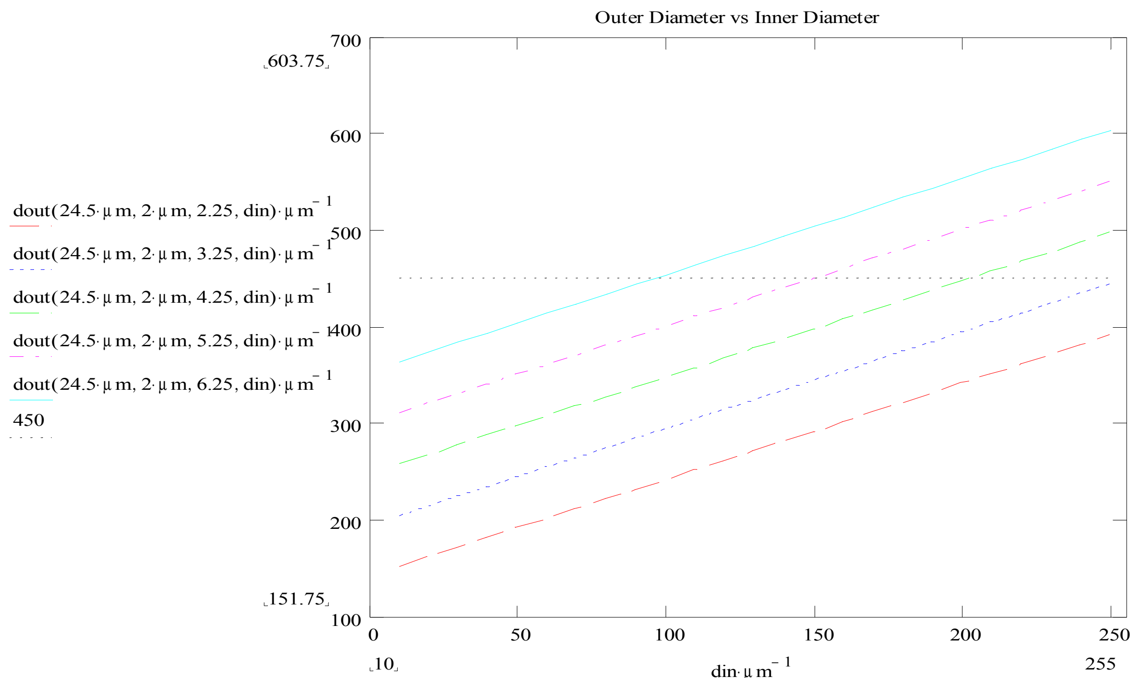

Figure E.1 Plotting the relationship between inner and outer diameters of a square planar spiral inductor (the dashed black line represents to 450µm d_{out} restriction, w =).

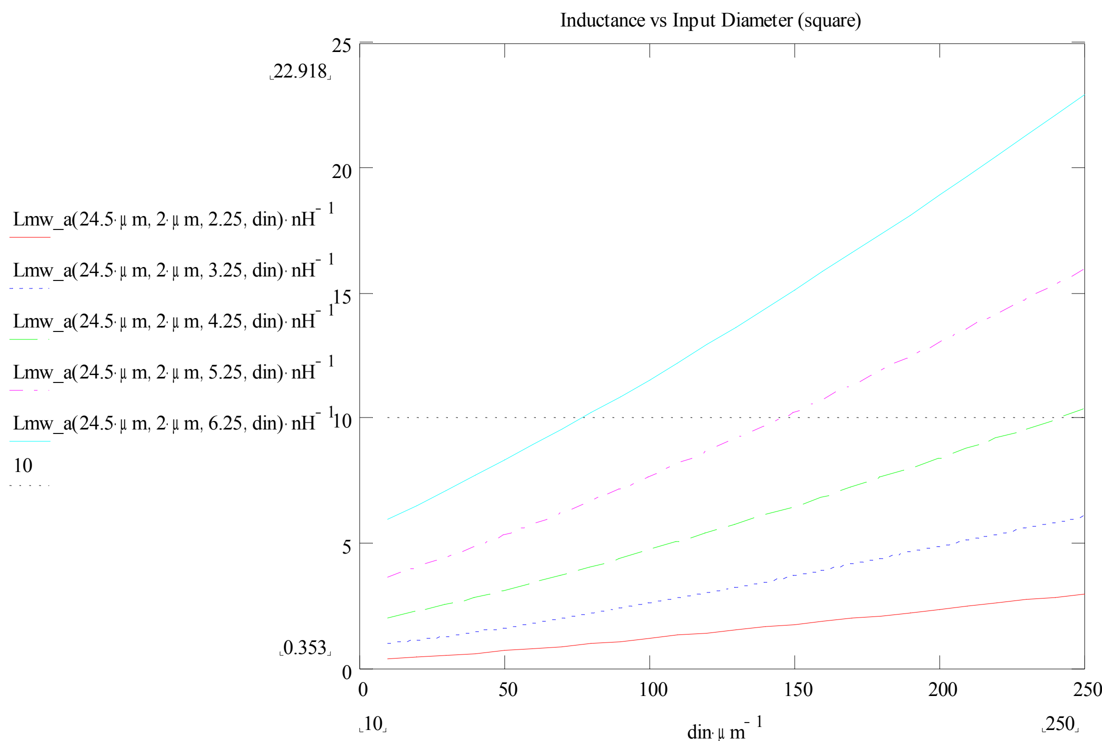

Figure E.2 Determining the turn and inner diameter requirements of a 10nH inductor (w = 24.5µm and s = 2.0µm).

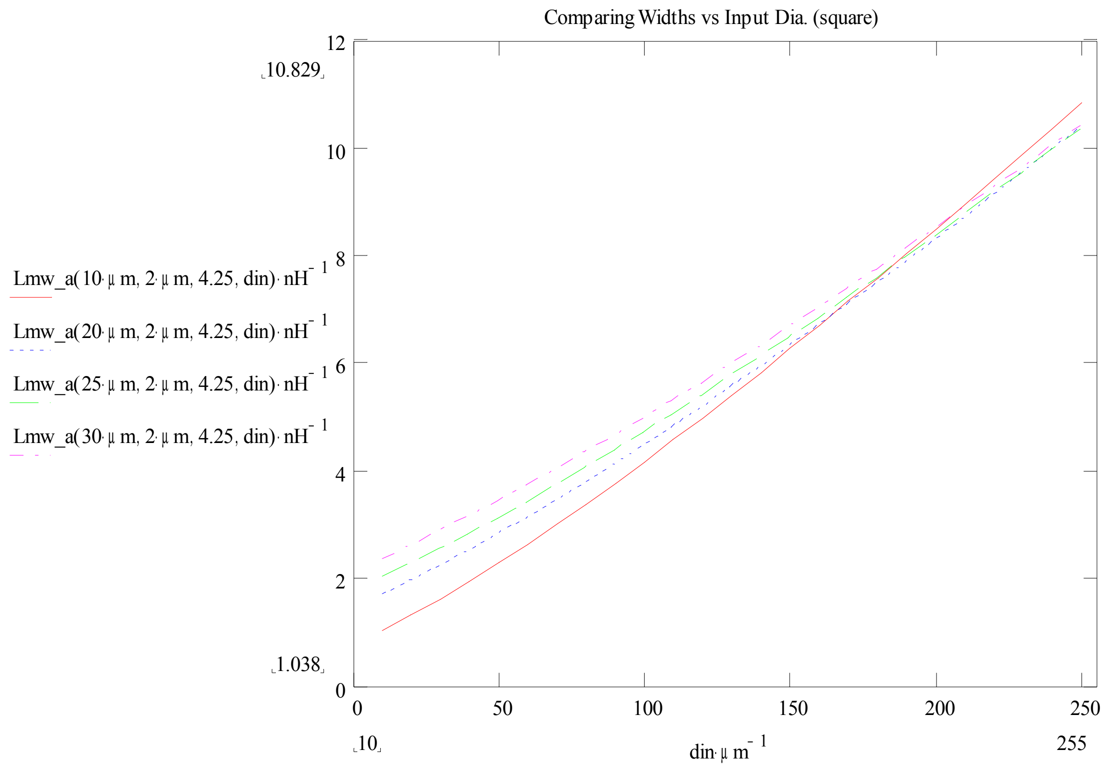

Figure E.2 Plotting the effects of winding width on square planar spiral inductance (n = 4.25, s = 2.0µm).

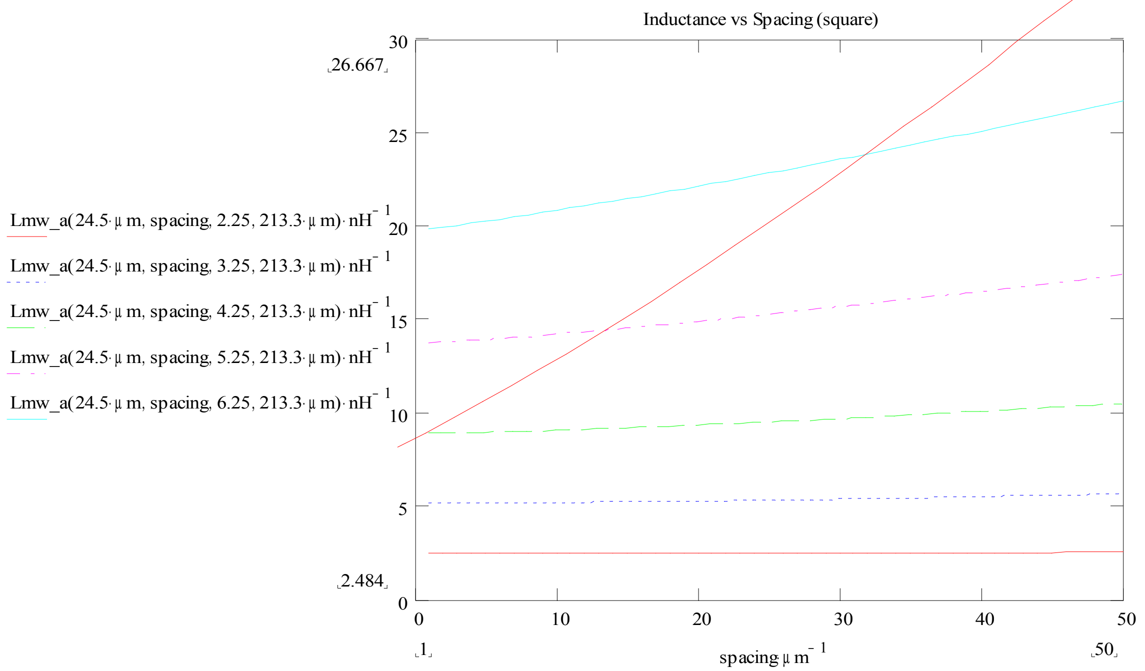

Figure E.3 Plotting the effects on winding spacing on inductance of square spiral inductor.

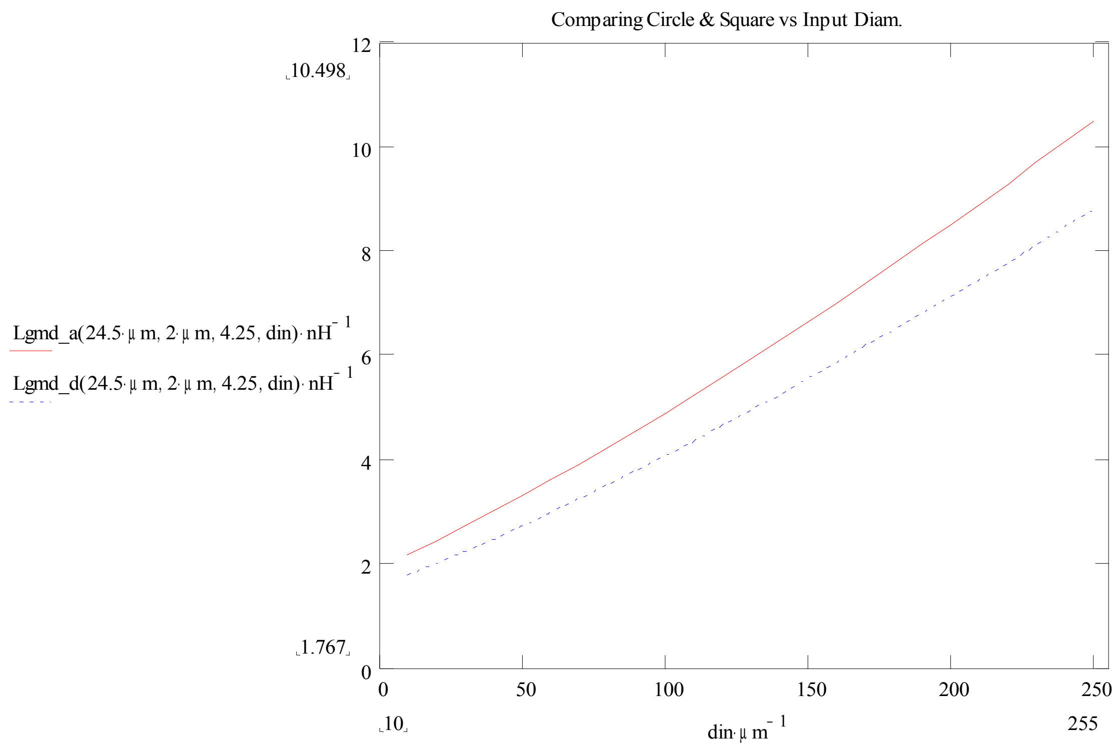

Figure E.4 Comparing inductance of circle and square spiral inductor geometries with equal dimensions.